

Atomic simulation of pull-out Halloysite nanotube from polyurethane  
by the molecular dynamic method

by

Mohammadreza Heidari Pebdani

A thesis submitted to the Faculty of Graduate and Postdoctoral  
Affairs in partial fulfillment of the requirements  
for the degree of

Master of Applied Science

in

Mechanical Engineering

Carleton University

Ottawa, Ontario

@2021

## ABSTRACT

The main restriction to employ different types of materials in ballistic applications is the disability to absorb energy exposure in high impact velocity, especially in civilian and defence applications. Nanomaterials and Nano-composites have been studied in various applications. One innovative approach is to employ a polymer in combination with a strong nanomaterial. In this study, we will consider a composite where the polymer matrix is a polyurethane (PU) and the nanoscale material is a Halloysite nanotube (HNT).

Mechanical properties are one crucial aspect of designing new material which significantly depends on nanofiller incorporation. Therefore, first, we analyze the lattice parameters of Halloysite (HNT) applying the Quantum Mechanics (QM), specifically Density Functional Theory (DFT). Then the molecular dynamics simulation was carried out to determine the Elastic modulus of Halloysite nanotube with zigzag and armchair arrangements. The elastic modulus of both arrangements is decreased with an increase in radius. Second, we used density functional theory to compute interaction energy between HNT-PU. Then the Machine Learning (ML) method with the particle swarm optimization (PSO) algorithm has been applied to fitting force field parameters of Molecular Mechanics (MM) using data from DFT calculations. The excellent agreement between the interaction energy from DFT and the optimized force field model was achieved. The optimum Lennard-Jones parameters were obtained by the interaction energy matching between DFT and MM results with less than 5 kcal/mol discrepancy. In this research, we present an

efficient and accurate method to compute the interaction potential between PU and HNT by the rigorous application of machine learning techniques.

In addition, molecular dynamics simulation has been applied to the study of pull-out of Halloysite nanotubes from a polyurethane matrix. We studied the interaction interface influence between HNT and PU matrix on the interfacial energy.

In the final part of this study molecular dynamics (MD) simulation has been applied to study the permanent strain of polyurethane (PU) reinforced with Halloysite through loading and unloading cyclic tests. The influences of the stretching cycle rate, different temperatures, the volume of HNT and the density rate of the hard and soft domain of PU were studied on the permanent set.

## ACKNOWLEDGEMENTS

I would like to express my appreciation to my advisor Professor Ronald Miller, for his support, patient and mentorship during my MSc mission at Carleton University. His endless guidance was not only the focus on the development of this thesis but also for my academic growth. My appreciation also goes to Prof. Andrei Artemev and Prof. Tao Jin for serving in my committee, and for their time, and insightful suggestions along with this dissertation. Special gratitude to our group members for the support and building a friendly environment, I will never forget that great times. We have passed through, and hopefully, in the future, our paths cross again. I would like to thank Dr. Nuwan Arachchigeand and Dr. Manura Liyanage for sharing their knowledge and contributing to this dissertation. I am deeply thankful to Rafaela Aguiar for her assistance at several steps of my MSc. mission. Your help and encouragement have been valuable to me. Last but not least, this dissertation is dedicated to my parents, my wife, my brothers and my sister; my nieces and my nephews for their endless care, support, patient and love that has kept me so motivated in achieving my goals.

## Table List

Table 2. 1: DFT type codes and features .....	27
<b>Table 2. 2:</b> force fields potentials of molecular mechanic .....	30
<b>Table 2. 3:</b> Stiffness and typical elastic modulus of four major bonds found in common solids material .....	31
<b>Table 3. 1:</b> Computed and experimental lattice parameters of PBC optimization; parentheses are shown percentage deviations. Data are reported in Å and degrees.....	44
<b>Table 3. 2:</b> Elastic constants of halloysite calculated by the MM and DFT approach, (Subscripts 1, 2 and 3 referred to X, Y and Z of Cartesian coordinates system. ....	54
<b>Table 3. 3:</b> Mechanical; properties of the single Halloysite sheet with assuming the material is isotropic and using Vigot and Reuss notation through the molecular mechanic and DFT simulation.....	54
<b>Table 3. 4:</b> List of bond and cutoff distance based on the minimum value in the RDF result.....	60
<b>Table 4. 5:</b> Elastic constants of amorphous polyurethane calculated by the molecular mechanic approach.....	72
<b>Table 4. 6:</b> Elastic constants of amorphous polyurethane calculated by molecular dynamics ....	73
<b>Table 5. 1:</b> improved pair coefficients for classical simulations.....	105
<b>Table 7. 1:</b> Ogden constitutive parameters for loading and unloading curves of PU/HNT composite	133

## Figure List

<b>Figure 1. 1:</b> Schematic of PU/HNT showing soft segment (SS) and hard segment (HS) domains .....	13
<b>Figure 1. 2:</b> Schematic of Polyurethane [2] .....	14
<b>Figure 1. 3:</b> Structure of segmented polyurethane (a), the two-phase structure of the bulk polymer (b) [4] .....	15
<b>Figure 1. 4:</b> MD simulation of Uniaxial compression stress-strain behavior of polyurethane in quasi-static strain rate regimes (a) PU with 54% HS, (b) PU with 44% HS[7].....	16
<b>Figure 1. 5:</b> Schematic of various deformation processes [8].....	17
<b>Figure 2. 1:</b> schematic force fields potentials of molecular .....	29
<b>Figure 3. 1:</b> Schematic of Halloysite structure [53] .....	41
<b>Figure 3. 2:</b> the hydrogen bonds between interlayers HNT .....	41
<b>Figure 3. 3:</b> lattice parameters of single repeat unit Halloysite (Hal-sing) [59]. .....	43
<b>Figure 3. 4:</b> Energy verse lattice b parameters of single repeat unit Halloysite (Hal-sing) .....	44
<b>Figure 3. 5:</b> Schematic of Nanosheet and Nano scroll form an HNT [59] .....	46
<b>Figure 3. 6:</b> Transmission electron microscopy image of Halloysite nanotubes [11]. copyright permission to reuse this image was obtained from the publisher. ....	46
<b>Figure 3. 7:</b> Schematic diagram showing zigzag and armchair of Halloysite .....	48
<b>Figure 3. 8:</b> supercell including 24480 atoms ( $156.4 \times 212.6 \text{ \AA}^2$ ).....	49
<b>Figure 3. 9:</b> molecular dynamics simulations of twin rolling of the layer of Halloysite, (a) 0 ps, (b) 2 ps, (c) 3 ps and (d) 5 ps. ....	49
<b>Figure 3. 10:</b> AFM images of Halloysite nanotubes [11]. copyright permission to reuse this image was obtained from the publisher. ....	50
<b>Figure 3. 11:</b> The rectangular supercell model has 93 nm 132 nm elongated in a and c directions exhibited in the structure of twisted formations with a diameter of 15 nm. (a) 0 ns, (b) 2 ns, (c) 3 ns and (d) 5 ns. ....	51
<b>Figure 3. 12:</b> single Halloysite nanotube [11]. copyright permission to reuse this image was obtained from the publisher. ....	52

<b>Figure 3. 13:</b> Schematic of loading direction (a) OA axis (b) OB axis (c) OC axis (d) The simulation cell of HNT is arranged into four layers, silicon (yellow) aluminum (pink). Oxygen and hydrogen atoms are displayed.....	56
<b>Figure 3. 14:</b> Density of models during the relaxation process .....	57
<b>Figure 3. 15:</b> Stress-strain curves for three strain rates ( $10^8$ , $10^9$ and $10^{10}$ s <sup>-1</sup> ) along the OA axis .....	58
<b>Figure 3. 16:</b> Stress-strain curves for three perpendicular loading directions (along with OA, OB and OC axis) .....	59
<b>Figure 3. 17:</b> radial distribution function (RDF) bond types in the Halloysite and the first minimum.....	60
<b>Figure 3. 18:</b> Fracture process for Halloysite nanosheet (model 1) in OA direction.....	61
<b>Figure 3. 19:</b> Fracture process for Halloysite nanosheet (model 1) in OC direction .....	61
<b>Figure 3. 20:</b> Fracture process for Halloysite nanosheet (model 1) in OB direction.....	62
<b>Figure 3. 21:</b> The structure of HNT (a) armchair HNT, (b) zigzag HNT .....	63
<b>Figure 3. 22:</b> Stress-strain curves of the armchair (ac) and zigzag (ZZ) HNT .....	64
<b>Figure 3. 23:</b> Effect of temperature on Young's modulus of HNT armchair and zigzag under uniaxial tensile .....	65
<b>Figure 3. 24:</b> variation Young's modulus respect evaluated radius for armchair and zigzag configurations of HNTs. The Elastic modulus of the flat sheet of HNTs is represented within dashed lines(different calculation) [55], [56].....	66
<b>Figure 4. 1:</b> Schematic of the basic reaction scheme of urethane formation [85].....	70
<b>Figure 4. 2:</b> Snapshot of an amorphous model of polyurethane with lattice parameters with dimensions a =b= c=46.3 Å, repeat units (n=20), No of chain = 15, No of atoms=8020 .....	71
<b>Figure 4. 3:</b> Stress-strain PMMA with various Halloysite percentages [70].....	76
<b>Figure 4. 4:</b> Stress-strain of polymers epoxy resin with various Halloysite [70] .....	76
<b>Figure 5. 1:</b> <i>interact between HNT with simple PU chain in a periodic periodic cell with 15.6 Å *25 Å *27.2 Å</i> .....	83
<b>Figure 5. 2:</b> Total energy convergence of HNT structure with (a)increasing cutoff energy, (b) with increasing k-points.....	84
<b>Figure 5. 3:</b> PU axes position respect to the flat surface of HNT, a) 0-degree, b) 30-degree, c) 60 degree and d) 90 degrees.....	85

<b>Figure 5. 4:</b> scans of the total energy for the different angles of PU respect to the flat surface of HNT .....	86
<b>Figure 5. 5:</b> sliding of the position of the center point of PU monomer respect to the center point of the flat surface of HNT .....	87
<b>Figure 5. 6:</b> scans of the total energy for the different lateral movements of PU respect to the flat surface of HNT .....	87
<b>Figure 5. 7:</b> trajectory, which is formed of the smaller vacuum gap (a, c nearest two-body) to the largest distance rearrangement (b, d far way PU monomer) periodic cell with 15.6 Å *25 Å *27.2 Å.....	88
<b>Figure 5. 8:</b> select atoms for constrained at x, y, and z-direction and matching lattice structure for both the HNT and a chain of PU .....	89
<b>Figure 5. 9:</b> total Energy vs non-band length between HNT with simple PU chain .....	90
<b>Figure 5. 10:</b> the optimized polyurethane chain PU (C <sub>17</sub> N <sub>3</sub> O <sub>3</sub> H <sub>18</sub> ) with dimension 15.6 Å *25 Å *27.2 Å.....	91
<b>Figure 5. 11:</b> the optimized HNT with dimension 15.6 *25*27.2 cubic Angstrom.....	92
<b>Figure 5. 12:</b> total energy evolution during the equilibration of the individual PU and the HNT.....	92
<b>Figure 5. 13:</b> scans of the interaction energy for the sliding of the position of the center point of PU monomer respect to the center point of the flat surface of HNT for opening movement.....	93
<b>Figure 5. 14 :</b> conjugate gradient minimization isolated the polyurethane chain and Halloysite flat surface.....	95
<b>Figure 5. 15:</b> The PSO algorithm.....	103
<b>Figure 5. 16:</b> the position vector and the velocity vector being updated at a t iteration as being composed by two components regarding a bi-dimensional problem [117].....	103
<b>Figure 5. 17:</b> Interaction energy vs Position of PU chain, a) before and b) after the fitting process.....	104
<b>Figure 5. 18:</b> density of the system vs time during equilibrium process .....	106
<b>Figure 5. 19:</b> The Molecular dynamics models of PU/HNT composite under the stretching test .....	107
<b>Figure 5. 20:</b> Stress-Strain diagram for MD and Experimental PU/HNTs samples .....	108
<b>Figure 6. 1:</b> density of the system vs time during equilibrium process .....	112
<b>Figure 6. 2:</b> snapshots pull-out of the HNT from the polymer matrix .....	113

<b>Figure 6. 3:</b> pull-out of the HNT from the PU matrix. (a) Fully embedded, (b) at 60 Å displacement of the HNT, (c) fully extracted HNT from PU and (d) cross-cut of fully extracted HNT .....	114
<b>Figure 6. 4:</b> Interaction potential energy for HNT/PU during the pull-out test .....	115
<b>Figure 7. 1:</b> Schematic of the Mullins effect.....	118
<b>Figure 7. 2:</b> Density of models after annealing cycle and relaxation process for PU (m=15) with 1% wt HNT, .....	121
<b>Figure 7. 3:</b> Stress-strain curves the PU/HNT composite .....	122
<b>Figure 7. 4:</b> Stress-strain response of HNT/PU composite versus different strain amplitude from 1 to 1.5 to 2.5. ....	123
<b>Figure 7. 5:</b> loading-unloading applied strain cycles, (a) PU/HNT, (b) strain=1, (c) strain=1.5, (d) strain=2.5, (e) Halloysite nanotube, .....	124
<b>Figure 7. 6:</b> Recovery of residual strain at different temperatures .....	125
<b>Figure 7. 7:</b> Uniaxial stress-strain behavior of HNT/PU in the Hard and soft segment ratio....	126
<b>Figure 7. 8:</b> Expansion of atomic stress for different macroscopic strains.....	127
<b>Figure 7. 9:</b> The distribution of the angle of atoms for two states .....	129
<b>Figure 7. 10:</b> The variation of the entanglement parameter during a stretch–release process....	129
<b>Figure 7. 11:</b> The stress-strain response for different HNT densities in the composite. ....	130
<b>Figure 7. 12:</b> (a) indicates f loading, and to (b) shows loading and unloading MD and Ogden constitutive models of the simulation. ....	134

## TABLE OF CONTENTS

ABSTRACT.....	1
Table List .....	4
Figure List.....	5
TABLE OF CONTENTS.....	9
Introduction.....	12
<b>1.1 Background and Motivation .....</b>	<b>12</b>
<b>1.2 Literature Review of PU .....</b>	<b>14</b>
<b>1.3 Objective .....</b>	<b>18</b>
<b>1.4 Dissertation Layout.....</b>	<b>19</b>
Computational chemistry .....	22
<b>2.1 Density Functional Theory (DFT) .....</b>	<b>22</b>
<b>2.2 Pseudopotentials.....</b>	<b>27</b>
<b>2.3 Molecular Dynamics and Molecular Mechanics .....</b>	<b>28</b>
2.3.1 Molecular Mechanics (MM);.....	28
2.3.2 Molecular Dynamics; .....	31
<b>2.4 Mechanical Properties .....</b>	<b>32</b>
2.4.1 Static Method.....	32
2.4.2 Dynamic Method .....	34
2.4.3 Ensemble Detail.....	35
2.4.4 Elastic Moduli of Polycrystalline Materials .....	36
<b>2.5 Theory in an Amorphous Cell.....</b>	<b>37</b>
<b>2.6 Software Packages.....</b>	<b>38</b>

Halloysite Nanotubes .....	40
<b>3.1 Literature Review.....</b>	<b>40</b>
<b>3.2 The Lattice Parameter of Unit Cell of HNT .....</b>	<b>42</b>
<b>3.3 Computational Method of Rolling Mechanism and Discussion.....</b>	<b>45</b>
<b>3.4 Mechanical Properties of the HNT (Atomic Simulation) .....</b>	<b>52</b>
3.4.1 Static Approach .....	52
3.4.2 Dynamic Approach.....	55
<b>3.5 Conclusion.....</b>	<b>67</b>
Polyurethane .....	68
<b>4.1 Mechanical Properties of the PU .....</b>	<b>69</b>
<b>4.2 Nanocomposite.....</b>	<b>73</b>
Modified Force Field .....	78
<b>5.1 Motivation .....</b>	<b>78</b>
<b>5.2 Methodology of Fitting Process.....</b>	<b>80</b>
5.2.1 Preparation of Supercell .....	81
5.2.2 DFT Calculation .....	82
5.2.3 Rotational Movement .....	85
5.2.4 Sliding Movement .....	86
5.2.5 Opening Movement .....	88
5.2.6 Interaction Energy .....	90
<b>5.3 Molecular Mechanics .....</b>	<b>93</b>
<b>5.4 Particle Swarm Optimization (PSO) .....</b>	<b>98</b>
<b>5.5 Model Validation .....</b>	<b>105</b>
<b>5.6 Concluding Remarks .....</b>	<b>108</b>
Pull-out Simulation .....	110

<b>6.1</b>	<b>Introduction .....</b>	<b>110</b>
<b>6.2</b>	<b>Modeling Simulation .....</b>	<b>111</b>
<b>6.3</b>	<b>Result of Pulling-out Simulation .....</b>	<b>114</b>
<b>6.4</b>	<b>Conclusions .....</b>	<b>115</b>
	Study of Irreversible Strain and Permanent Set of PU Reinforced with HNT .....	117
<b>7.1</b>	<b>Introduction .....</b>	<b>117</b>
<b>7.2</b>	<b>Molecular Dynamic Model .....</b>	<b>120</b>
<b>7.3</b>	<b>Results and Discussion .....</b>	<b>121</b>
	7.3.1 Cyclic Loading .....	122
	7.3.2 Temperature Evaluates .....	125
	7.3.3 Chain Entanglement Evolution.....	128
<b>7.4</b>	<b>Ogden Pseudo-Elasticity Model .....</b>	<b>131</b>
<b>7.5</b>	<b>Conclusion.....</b>	<b>134</b>
	General Conclusions .....	137
	References.....	140

## Introduction

### 1.1 Background and Motivation

Nowadays security concerns from ballistic impact have increased worldwide due to threats of civilian attacks or explosives. Hence, it is necessary to consider improved explosive protective devices. A ballistic impact is generally a phenomenon that begins when a projectile is propelled toward a target and ends within. A ballistic impact is a high-velocity impact where the projectile speed is in the range of 0.05 to 2 km/s [1].

During ballistic impact, structures in various applications are exposed to extreme conditions especially at high stress and strain rate. For impact velocities associated with defense ballistics application, high strain rates are in the range of  $10^5/s$  to  $10^6/s$  [1]. Nanocomposite materials can improve ballistic protection and enhance thermal-mechanical stability. Moreover, these materials are more lightweight, flexible, transparent, and capable of absorbing energy.

One innovative approach employs polymer combined with a reinforcing nanoscale material to improve their functionality in extreme conditions (high stress or high strain rate during ballistic impact). In this study, we will consider a composite where the polymer matrix is a polyurethane (PU) and the nanoscale material is Halloysite nanotube (HNT) as displayed in Figure 1. 1. We are expecting an improvement in the structure of the PU

augmented with HNT, at the end, we are able to predict the PU/HNT nanocomposite behaviour and indirectly achieve a better understanding of structure at the atomic level.

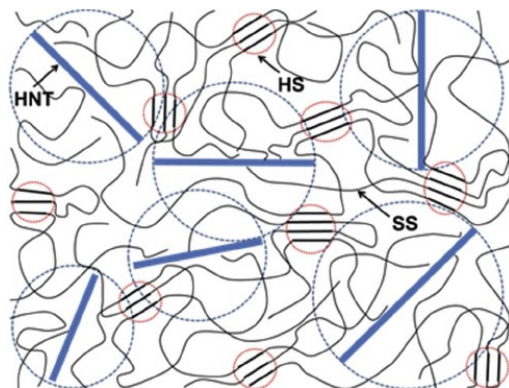


*Figure 1. 1: Schematic of PU/HNT showing soft segment (SS) and hard segment (HS) domains*

The Halloysite is small enough to be dispersed throughout the polymeric matrix. The chemical interaction between the matrix (PU) and the nanoscale material (HNT) makes it a valuable candidate to reinforce components for the matrix. In this case, the mechanical enhancement is achieved by increasing the chemical interaction between the polyurethane and the Halloysite, which restricts the motion of polymer chains and strengthens the composite. Hence, nanocomposites behave differently when compared with unreinforced composites.

Polyurethane (PU) is a copolymer formed by combining a di-isocyanate ( $\text{OCN-R-NCO}$ ) and a polyol ( $\text{OH-R'-OH}$ ), where R is aromatic or aliphatic and R' is a linear hydrocarbon chain (shown in Figure 1. 2) [2]. Also, PU is considered as soft segments (SS) which are from the polyol and hard segments (HS) create of the di-isocyanate. The HS act as rigid fillers that reinforce the amorphous regions and lead to an increase in Young

modulus and the tensile strength. In contrast SS is a chain extender and influences cross-links between chains. The chemical composition of HS and SS is provided in chapter 4 [2]. PU has a variety of applications in a range of products such as foams, coatings, adhesives, fibers, rubbers, or thermoplastic elastomers[3]. Furthermore, polyurethane has good corrosion resistance and fire resistance which is of significant concern in both civilian and defense applications [2].

Recently, new applications of polyurethane have been developed for protection against blast and ballistic loading. Understanding polyurethane's response in a range of strain rates is essential to employ it in extreme loading conditions.

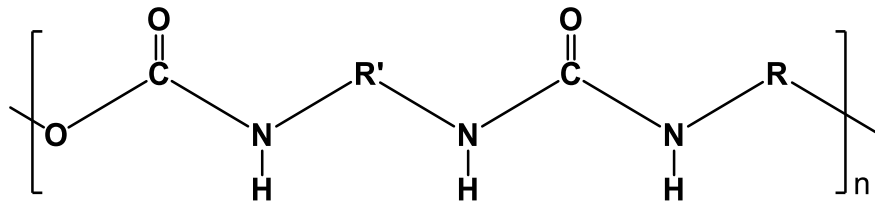


*Figure 1. 2: Schematic of Polyurethane [2]*

## 1.2 Literature Review of PU

Figure 1. 3 shown that PU is considered a copolymer with different parts: soft segments (SS) from the polyol and hard segments (HS) from the di-isocyanate of crystalline and amorphous regions. Due to their polarity and chemical nature, the soft and hard segments are incompatible and form separate phases in nanoscale domains. The extent to which phase separation occurs is dependent on the size of the hard and soft segments,

the chemical composition of di-isocyanate and polyol and the hydrogen bond between urethane linkages [3].

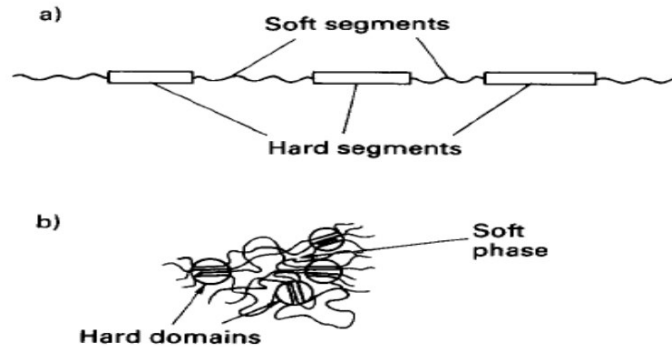


*Figure 1. 3: Structure of segmented polyurethane (a), the two-phase structure of the bulk polymer (b) [4]*

The nature of polyurethane leads to the formation of a complex nanoscale morphology due to repeating units of hard and soft segments. The alternating soft and hard segments assemble create excellent mechanical properties [5]. Consequently, PU can be employed not only for its lightweight nature but also for its dynamic properties that provide opportunities for use under high pressures conditions during shock or impact loading application [6].

In molecular dynamics, Yi et al. considered the mechanical behavior of polyurethane (PU) under high and low strain rate conditions with different hard segment ratios, where the main focus of their work was understanding the change in the glass transition temperature ( $T_g$ ) with the strain rate. Their copolymer was composed of “hard” and “soft” segments that had a different glass transition temperature ( $T_g$ ), and melting temperature ( $T_m$ ). Figure 1. 4 illustrated the mechanical behavior versus the strain rate for different hard segment ratios of the sample PU [7].

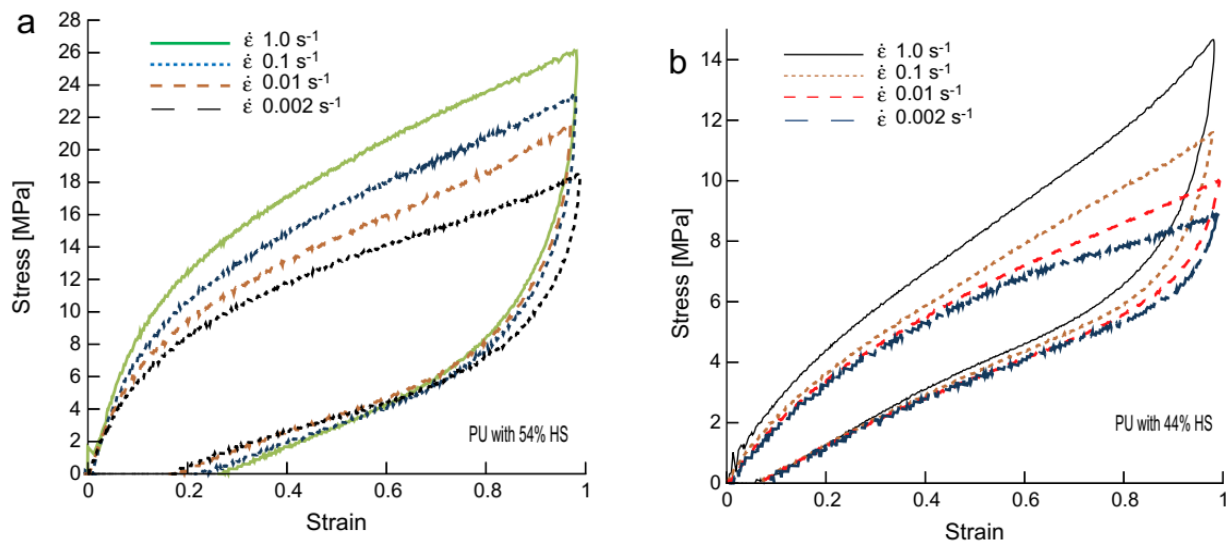


**Figure 1. 4:** MD simulation of Uniaxial compression stress-strain behavior of polyurethane in quasi-static strain rate regimes (a) PU with 54% HS, (b) PU with 44% HS[7]

Lee and his colleagues described the molecular behavior of polyurethane in high strain conditions by developing a simple model layered nanocomposite system, where the layers simulated the behavior of the hard and soft domains. According to the authors, during ballistic impact the initial structure is highly compressed, causing the domains to form fragments and segments to mix. As the temperature rises, the granular<sup>1</sup> phase gets more homogenous through further segmental mixing, as described in Figure 1. 5 [8].

<sup>1</sup> A particle of solid is discrete, macroscopic particles decrease energy when particles interact (the most common example is friction when the seeds collide)

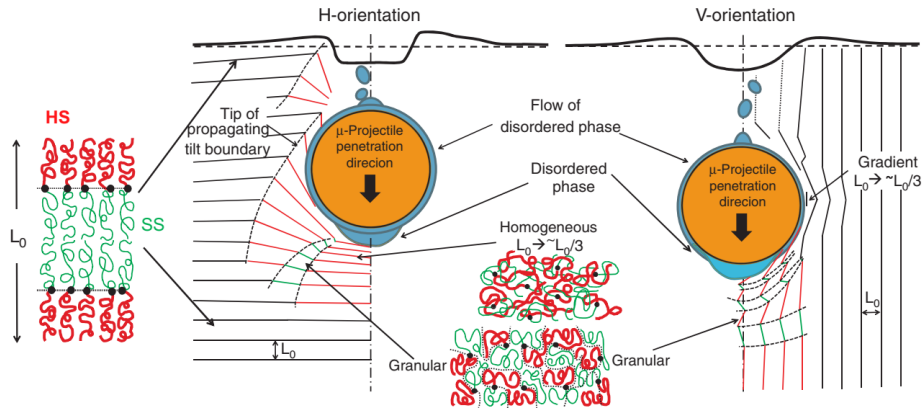


**Figure 1. 5:** Schematic of various deformation processes [8]

However, polyurethane has some limitations in its applications, due to poor thermal capability, poor durability against most solvents and low strength during high strain rate conditions. Therefore, it can be reinforced with a rigid and strong nanomaterial.

Polyurethane/Halloysite is composed of more than 95% (by weight) content of polyurethane polymer and less than 5% hard mineral ingredient in the form of Halloysite structural. Natural and synthetic polymers reinforced with Halloysite nanotubes (HNTs) play an important role in designing new nanocomposites. Carbon nanotubes are the most commonly studied nanomaterial; however, toxicity and high costs make it less attractive in industrial applications. However, HNT is extensively available around the world at low cost, and so has received more attention from researchers. HNT has become an interesting reinforcement particle material for developing the functionality of the polymer [9]. Halloysite is a clay tube with a length of 600–1000 nm and an internal radius of 12-30 nm, an external radius of 30-100 nm [10], [11].

The main goal of this study is to provide fundamental insights into the properties of polyurethane/ Halloysite nanocomposite for potential application in ballistic applications

(high strain rate performance) in both civilian and defence applications. Understanding the structure, properties and dynamic response of these materials at the atomistic scale, provides great help to design new material beyond ballistic application. These opportunities, if exploited, can possibly produce many protective materials for future application.

### **1.3 Objective**

To implement HNTs in different applications, it is necessary to consider materials exposed to different loading conditions. HNTs have extraordinary properties, in specific, stiffness and strength, which make them attractive as the reinforcing element in a composite material. To achieve the full benefit of these properties, it is necessary to understand the combination with a matrix material. The purpose of this research is to use computational techniques to study the properties of the HNT/PU nanocomposite.

The incorporation of HNTs can possibly improve the ability of polyurethane to absorb energy during high strain rate conditions, due to HNTs ability to chemically interact with the polyurethane and fine dispersion around the polymeric structure. Specifically, this work examines the interaction interface response of the HNT/PU nanocomposite. The study of this interaction can possibly indirectly provide a better understanding of the energy absorption mechanism at the atomic level of the polyurethane under high strain conditions.

For this purpose, we will apply computational techniques to investigate the structural properties of the polymer nanocomposite at the atomistic level. We will use ab-

initio calculation, in particular, density functional theory to compute interaction energy between HNT-PU. Then the Machine Learning (ML) method of particle swarm optimization (PSO) technique was used to obtain force field parameters for MD from data of DFT calculations.

Overall, the expansion of a general set of interatomic potentials is a considerable subject for the molecular simulation of the various molecular system [12], [13]. The PCFF-IFF force field provides a general set of interatomic potentials that allow to evaluate of the complex response of natural materials. In this research, a new method has been developed to generate new interatomic parameters for HNT-PU by applying the particle swarm optimization method to fit MM calculation to the desirable DFT data to obtain the best values of Lennard-Jones parameters for PCFF-IFF potential.

With increasing computational power, applying computational analyses is getting much more attention from researchers in different fields. Nevertheless, computational analyses, especially molecular simulations, cannot replace conventional laboratory experiments. Thus, to ensure reliability and accuracy, the results obtained from our simulations will be compared with previous theoretical and experimental studies.

#### **1.4 Dissertation Layout**

Chapter 2 introduces an overview of the fundamentals of computational theory for material simulations. Computational simulations have been developed to bridge the gap between classical theory and experiments. This section highlights the computational methods applied in this research, such as molecular mechanics, molecular dynamics and

density functional theory. By combining the appropriate computational models with relevant computational software, it is possible to understand material behavior without conducting any real experiments.

Chapters 3 and 4, constitute a literature review of components used for polymer nanocomposite, particularly in chapter 3, concentrated on Halloysite nanotube as a reinforcing nanoparticle in polymer matrices. In chapter 3, first, we examined the equilibrium lattice parameter for HNT by DFT. Then, we illustrated the transformation of slab Halloysite to scroll shape with the proper selection of the potential. Also, the molecular simulation was conducted to determine the mechanical properties of Halloysite under different conditions. The results displayed that the Elastic modulus of an armchair Nano scroll was higher than zigzag with similar dimensions, and that Young's modulus of both arrangements decrease with an increased radius. Following that, in chapter 4, a literature review of polyurethane was conducted. These chapters contribute a conceptual framework for the development of HNT/PU nanocomposite.

Chapter 5 describes the application of density functional theory and Molecular mechanics in obtaining interaction energy between HNT and PU. First, we employed density functional theory to compute interaction energy between HNT and PU. After obtaining interaction energy between HNT/PU, we developed a technique for developing the classical PCFF-IFF force field for HNT-PU by applying the particle swarm optimization algorithm to fit MM calculation to the desirable DFT-computed atomic.

Finally, in chapter 6, we studied the effects of the interatomic strength between the HNT and PU composites. For this purpose, we studied the HNT pull-out from the polyurethane matrix by the MD simulation. Once the HNT is extracted out of the PU, the potential energy increases and finally reaches to the summit. When the HNT is farther away from the PU, the interaction energy of HNT with the matrix becomes weaker, due to the decreasing interaction between the HNT and PU due to decreasing interface area. The result of this study is a great help for understanding HNT/PU which can be used for designing new generation nanocomposites.

## Computational chemistry

Recently, computers have become powerful tools for researchers to study chemical systems at the level of the electronic structure, thus it allows researchers to bridge between classical theory and experiment results. Quantum Chemistry (QC) is a computational simulation method to determine the energy of the system and forces acting upon the atoms in the system. QC may be classified into different theories, such as ab-initio methods and semi-empirical, where each theory identifies according to different methods to reduce computational effort.

The following chapter reviews the fundamental computational models for material simulations, especially, density functional theory (DFT), molecular mechanics (MM) and molecular dynamics (MD). These methods will be applied to study atomistic simulation. By combining the right computational models with the appropriate computational software, it will be possible to understand material behavior without performing physical experiments [14]–[16].

### 2.1 Density Functional Theory (DFT)

The DFT theorem says that all properties of a system are determined uniquely from the electron density, regardless of the details of the electron wave functions form. This popular approach is a variational method that depends on the electron density. The Schrödinger equation introduces the wave function of a particle:

$$\left\{ \frac{-\hbar^2}{8\pi^2 m} \nabla^2 + V \right\} \psi(\hat{r}, t) = \frac{i\hbar}{2\pi} \frac{\partial \psi(\hat{r}, t)}{\partial t} \quad (2.1)$$

In this equation,  $\psi$  is the wave function (dependent on position and time),  $m$  is the mass of the particle,  $V$  is a potential field in which the particle is moving and  $\hbar$  is Plank's constant ( $4.1357 \times 10^{-15}$  eV s). The Schrödinger equation can be simplified by using the mathematical separation variable technique, as a function of time and position as the following equation;

$$\begin{aligned} \psi(\hat{r}, t) &= \psi(\hat{r})\tau(t) \\ H\psi(\hat{r}) &= \varepsilon\psi(\hat{r}) \end{aligned} \quad (2.2)$$

The Hamiltonian consists of the following terms:

$$H = \underbrace{-\frac{\hbar^2}{2} \sum_I \frac{\nabla_I^2}{M_I} - \frac{\hbar^2}{2} \sum_i \frac{\nabla_i^2}{m_i}}_T + \underbrace{\frac{1}{2} \sum_{I \neq J} \frac{e^2}{4\pi\epsilon_0 |r_i - r_j|} \frac{1}{2} \sum_{I \neq J} \frac{Z_I Z_J e^2}{4\pi\epsilon_0 |R_I - R_J|} - \sum_{i,I} \frac{Z_I e^2}{4\pi\epsilon_0 |r_i - R_I|}}_V \quad (2.3)$$

where  $M$  is the mass of the particle,  $\nabla_i^2$  is the Laplacian operator,  $r$  is designated to the position vector of the electron within the atoms,  $R_i$  and  $R_j$  refers to position vectors of nuclei within the atoms,  $e$  refers to electron charges,  $Z_i$  and  $Z_j$  refers to atomic numbers,  $\hbar$  refers to Plank's constant ( $4.1357 \times 10^{-15}$  eVs) and  $\epsilon_0$  is the vacuum permittivity  $8.8542 \times 10^{-12}$  F.m<sup>-1</sup> (farads per meter). For the above equation, the Hamiltonian consists of the energy term associated to the motion of the nuclei and repulsion between the nuclei (described as Coulomb's law); the energy term associated to the motion of the electrons,

the electron-electron repulsion (described as Coulomb's law) and the term potential energy of nuclei-electron attraction respectively.

According to Molecular orbital theory, the wave function is comprised of molecular orbitals to cover all conditions on the wave function. Moreover, these sub functions must be a normalized and orthogonal set of molecular orbitals.

$$\iiint \phi_i^* \phi_i dx dy dz = 1 \quad (2.4)$$

$$\iiint \phi_i^* \phi_j dx dy dz = 0 \quad i \neq j \quad (2.5)$$

Each molecular orbital holds only one electron, however most calculations are closed shell calculations using doubly-occupied orbitals holding two electrons of opposite spin. Electron spin can have up (+1/2) and down (-1/2). Thus, there is a two spin functions as follow:

$$\begin{aligned} \alpha(\uparrow) &= 1 & \alpha(\downarrow) &= 0 \\ \beta(\uparrow) &= 0 & \beta(\downarrow) &= 1 \end{aligned} \quad (2.6)$$

The function  $\alpha$  is 1 for spin up and function  $\beta$  is 1 for spin down, thus the notation  $\alpha(i)$  and  $\beta(i)$  will describe values of for electron  $i$ .

The closed-shell wave function is defining the  $n/2$  molecular orbitals for a system with  $n$  electrons, for recall, a pair of an electron in each orbital has opposite spin:

$$\Psi(\hat{r}) = f\left(\phi_{\frac{n}{2}}(\hat{r}_n)\alpha(n), \phi_{\frac{n}{2}}(\hat{r}_n)\beta(n)\right) \quad (2.7)$$

The molecular orbital is a combination of one-electron functions called basis functions ( $\phi$ ). Each basis function is usually centred on an atomic nucleus and atomic orbital. There are several appropriate definitions for basis function;

$$\phi_i = \sum_{\mu=1}^n c_{\mu i} \chi_{\mu} \quad (2.8)$$

$$\iiint \phi_i^* \phi_i dx dy dz = 1 \quad (2.9)$$

$$\iiint \phi_i^* \phi_j dx dy dz = 0 \quad i \neq j \quad (2.10)$$

Where  $i$  refer to electron orbital-spin,  $C_{\mu i}$  is molecular orbital expansion coefficient and  $\chi_{\mu}$  is refers to an arbitrary basis function, hence  $\phi$  refers to an arbitrary molecular orbital basis function. The problem is how to solve equations (2. 2) and (2. 8) for the expansion coefficient  $C_{\mu i}$ . Finding the solution for the Schrödinger equation problem would be challenging for the multi-electron due to interacting between electrons nuclei.

Density functional theory (DFT) was derived from quantum mechanics by Walter Kohn who won the Nobel Prize in chemistry in 1998 [17], [18]. The DFT states that all properties of a system are determined uniquely from the electron density, regardless of the details of the electron wave functions from which the density is derived. Over the years, the original formulation of the DFT has extended to cover several applications [17], [18].

The Hohenberg-Kohn theorem determines the ground state energy and exact density. One of the popular approaches under this theorem is a variation method for a single

electron problem instead of for the whole electron wave function[18]. The Hohenberg-Kohn theorem employs an approximated base on an integral involving only the spin densities [19]. Becke formulated based on modify basis set with the Local Exchange function term [20]. Perdew and Wang determined Gradient-Corrected functions modify term [21].

The different DFT methods are classified by a different definition of the improvement term functions, for example, the BLYP (Paris Lee-Yang and Par [22]) function is defined according to a combination of gradient-corrected exchange function with the gradient-corrected correlation function.

There is a wide variety of DFT codes, where the choice of code depends on the system. Generally, there are two main types of DFT methods: those based on a set of plane waves as the basis set, referred to as plane-wave methods (PW); and atomic orbitals, referred to as localized-orbital methods (LCAO). Table 2.1 identifies DFT methods. Complete information can be found in [17], [23].

DFT is one of the most accurate approaches to study various chemical structures at the electron scale. However, it neglects thermal contributions when using the ground state energy, therefore, the DFT results are derived at absolute zero temperature.

Table 2. 1: DFT type codes and features

Plane-wave DFT [24]		Localized-orbital DFT [25]	
Advantage	Reliable for reciprocal space (FFT) and fully periodic system,	Advantage	Uses strictly-localized or fast-decaying orbitals
	Perfect for crystals, extremely small unit cells and utilized different k-point sampling,		More freedom in the choice of boundary conditions,
	Plane waves do not move with atoms, meaning there are no Pulay forces affect (makes MD and geometry optimization easier)		Usually no or comparatively little cost for vacuum
	PW basis set depends on KE cutoff, and thus on grid spacing. This makes varying the simulation cell size or shapes.	Disadvantage	Free of the pseudopotential approximation,
	Pseudopotential approximation almost always necessary, because the all-electron wave function oscillates rapidly close to the nucleus.		Basis-set superposition error needs to be taken into account
	No basis-set superposition error (BSSE)		Basis functions move with atoms, leading to Pulay forces. This makes MD and geometry optimization more difficult
Disadvantage	Plane waves as a basis set mean that one usually "pays for vacuum" (more padding means more computational effort and higher memory requirements)	Software	Gaussian
	Cost of using hybrid functional comparatively high		
Software	CASTEP, Quantum espresso, VASP, CPMD, ABINIT, ONETEP, D mol3		

## 2.2 Pseudopotentials

A pseudopotential is an approximation approach for describing electron-ion atomic systems through a small number of Fourier elements. A solid has several valence electrons and ion cores. The ion cores include nuclei and tightly restrained core electrons. In the pseudopotential procedure, ion cores are assumed to be fixed. This means that the properties of solids or molecules are determined on the hypothesis that the ion cores are

not associated with chemical bonding and do not exchange on structural modifications. In the pseudopotential method, the core electrons and Coulomb interact substitutes by a pseudopotential function that behaves on a set of pseudo wave functions. In this research, the projector augmented wave (PAW) pseudopotential [26] was applied for all DFT calculations [27].

## **2.3 Molecular Dynamics and Molecular Mechanics**

### **2.3.1 Molecular Mechanics (MM);**

Molecular Mechanics (MM) applies Newtonian mechanics to simulate the chemical structure. The Newtonian mechanic laws are used to calculate configurations of atoms based on empirical force fields. The force field parameters can be obtained by fitting to DFT or experimental data. In MM, the optimum geometry of a molecule depends on the potential energy of the structure. In this process, electronic structure is ignored (as it is expected to be represented by the force field) and only the positions of the atoms are considered.

Molecular Mechanics is basically a method that uses potentials that are functions of intramolecular bonds lengths, bond angles, and bond dihedral angles of the molecules. (See Figure 2. 1).

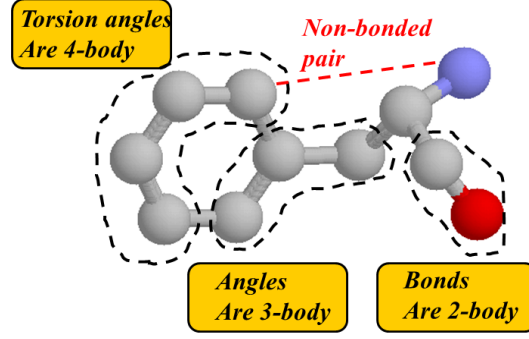


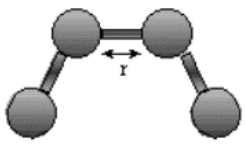
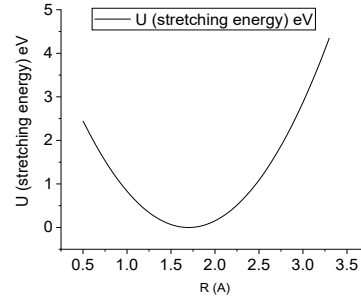
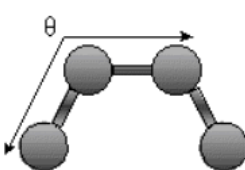
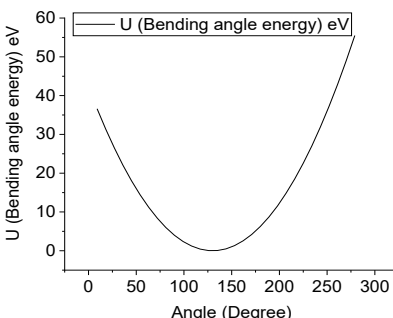
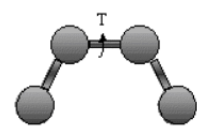
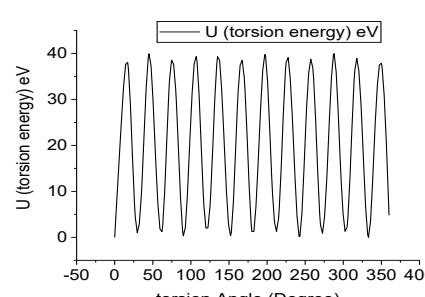
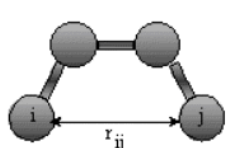
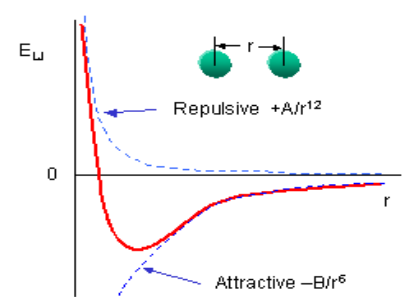
**Figure 2. 1:** schematic force fields potentials of molecular

The potential energy function depends on the positions of nuclei which is derived from positions of the atoms within a molecule. Some common potential energy functions used are CHARMM, AMBER, PCFF, Dreiding, UFF, and COMPASS [28]–[33]. In general, the choice of a particular force field depends on the properties of the system. The potential energy  $U$  of a system of atoms is;

$$U = \sum_{\text{all bonds}} \frac{1}{2} K_b (b - b_0)^2 + \sum_{\text{all angles}} \frac{1}{2} K_\theta (\theta - \theta_0)^2 + \sum_{\text{all torsions}} K_\varphi [1 - \cos(n\varphi)] + \sum_z K_\chi \chi^2 + \sum_{i,j \text{ nonbonded}} \epsilon_{ij} \left[ 2 \left( \frac{R_{ij}}{r_{ij}} \right)^9 - 3 \left( \frac{R_{ij}}{r_{ij}} \right)^6 \right] + \sum_{i,j \text{ nonbonded}} \frac{q_i q_j}{4\pi\epsilon_0 \epsilon r_{ij}} \quad (2. 11)$$

The first four terms in equation 2.11 introduce the stretch bonds energy ( $b$ ), bend angles energy ( $\theta$ ), torsion angles energy ( $\varphi$ ) and distort energy respect to a reference plane ( $\chi$ ). The final terms represent the non-bonded interactions as a sum of van der Waals and electrostatic interactions. All terms depend on the distance ( $r_{ij}$ ) between atoms. Each force field defines a specific coefficient for all type atoms in the equation(2. 11). The following Table 2. 2 gives an idea of each of these terms as described in equation 2.11.

Table 2. 2: force fields potentials of molecular mechanic

stretching energy	$U = \sum_{\text{all bonds}} \frac{1}{2} K_b (r - r_0)^2$		
Bending angle energy	$U = \sum_{\text{all angles}} \frac{1}{2} K_\theta (\theta - \theta_0)^2$		
torsion energy	$U = \sum_{\text{all torsions}} K_\phi [1 - \cos(n\phi)]$		
Non-Bonded Energy	$U = \sum_{i,j \text{ nonbonded}} \epsilon_{ij} \left[ 2 \left( \frac{R_{ij}}{r_{ij}} \right)^9 - 3 \left( \frac{R_{ij}}{r_{ij}} \right)^6 \right]$		
	$U = \sum_{i,j \text{ nonbonded}} \frac{q_i q_j}{4\pi\epsilon_0 \epsilon r_{ij}}$		

The following Table 2. 3 gives an idea of the various types of bonds found in different solids;

*Table 2. 3: Stiffness and typical elastic modulus of four major bonds found in common solids material*

<b>Bond</b>	<b>Example</b>	<b>Bond Energy (kJ/mol)</b>	<b>Bond Energy (eV/Atom)</b>
<b>Covalent</b>	C-C(diamond)	713	7.4
<b>Metallic</b>	Al	324	3.4
<b>Ionic</b>	MgO	1000	5.2
<b>Van der Waals</b>	Cl <sub>2</sub>	31	0.32

### 2.3.2 Molecular Dynamics;

Molecular dynamics (MD) is an algorithm for solving Newton's equations of motion for a collection of atoms with discrete time steps. It can be used for polymers and composites containing a large number of atoms (millions to billions) as a computational process of simulating molecular motion. Consequently, potential-based methods that are computationally cheaper than DFT are applied for chemical systems. A large simulation cell is required to effectively represent the long-range order in such systems [34].

Calculations of the equations of motion also depend on thermodynamic properties. There are numerous packages that are used for MD such as; GROMACS, LAMMPS [35] and Material Studio package [24], [36]. In this project, we used the LAMMPS package.

The typical time scale for atomic motions in MD is in a picosecond ( $10^{-12}$ ) or less, and we should use femtosecond ( $10^{-15}$ ) time steps to avoid any numerical errors, Therefore, it takes many more than a million iterations to follow the motion for just a microsecond [35].

MM and MD are similar but somewhat different. The main function of MD is the modelling of molecular movements; However, it could be used for optimization. MM ignores the fluctuations which happen due to thermal movement. Generally, both employed the same classical force fields [37].

## **2.4 Mechanical Properties**

Studying size effects on the mechanical properties of nanostructures is extremely important to classify their functionalities and potential application. However, mechanical analyses of nanoscale objects are considerably restricted due to the difficulties encountered in the set-up of conventional tensile or bending tests. During the last three decades, several techniques based on the use of atomic force have been extended to analyze the mechanical behavior of nanoparticles [38], [39]. Various functions are available for the calculation of elastic moduli which we can categorize as static and dynamic ways.

### **2.4.1 Static Method**

The static approach ignores the fluctuations which happened due to thermal movement. This technique is usually applied to a geometrically optimized structure. Analytical calculation on the response in an optimized structure by using the cell Hessian matrix, or by employing a small and finite strain. Young's moduli in the static approach are given by eq (2.12) [40];

$$E = \frac{1}{V_0} \left( \frac{\partial^2 U}{\partial \varepsilon^2} \right) \quad (2.12)$$

Where  $V_0$  is the equilibrium volume,  $\varepsilon$  is the strain, and  $U$  is the total energy. This methodology keeps the stress small zero in the non-deformed directions and allows the calculation of elastic constants from 1-D stress–strain curves. The resulting six stress components are calculated from a summation over all particles in the system from  $k = 1$  to  $N$

$$\sigma_{ij} = \frac{\sum_k^N M_k v_{ki} v_{kj}}{V} + \frac{\sum_k^N F_{ki} r_{kj}}{V} \quad (2.13)$$

where  $i, j = x, y, \text{ and } z$ ,  $M_k$  refers to the atom mass,  $v_{ki}$  identifies the atomic velocity,  $V$  refers to the volume of the structure,  $r_{ki}$  refers to the atom location, and  $f_{kj}$  is the atomic force. Applying Hooke's law and Voigt notation, the stiffness tensor  $C_{ijkl}$ , can be obtained as the following equation:

$$\sigma_{ij} = \sum_{k=1}^3 \sum_{l=1}^3 C_{ijkl} \varepsilon_{kl} \quad (2.14)$$

where  $\sigma_{ij}$  refers to the stress tensor,  $\varepsilon_{ij}$  refers to the strain tensor, and  $C_{ijkl}$  refers to the stiffness tensor. Because of symmetry, the stiffness tensor reduced to 21 components [39], [41];

A relevant method is found in the work of Theodorou and Suter (1986) [39], [42]. For their method, the relaxation contributions are computed numerically, instead of applying analytical derivatives. During geometry optimization, the structure is constrained to twelve deformations; three sets in uniaxial tension/compression and three sets including pure shear. Each of those deformations corresponds to producing one of the parts of the strain vector (Eq. (2.12)) to some small amount (for example  $\varepsilon = 0.001$ ) while retaining all

other parts fixed at zero. Subsequent to each deformation, the structure is allowed to relax internally while it has constant strain. Therefore, 21 components of the stiffness matrix can be determined from the static method using eq (2.15) [40];

$$\frac{\partial^2 U}{\partial \varepsilon_{ij} \partial \varepsilon_{kl}} = \frac{\partial \sigma_{ij}}{\partial \varepsilon_{kl}} \quad (2.15)$$

where U is the potential energy.  $E_i$  refers to elastic moduli that can be derived of the stiffness tensor  $S_{ijkl}$  and,  $S_{ij} = C_{ij}^{-1}$ , therefore,  $E_i = 1/S_{ii}$  [39], [42]. In the static mode, the temperature doesn't play any role. Consequently, entropic contributions to the elastic constants are neglected.

Besides Young's modulus, another component is the Poisson ratio, which estimates the variation in a material at perpendicular angles to the axial stress. Generally, it is determined as the ratio of lateral to longitudinal strain under a uniform axial stress. The formulation used to calculate the Poisson ratio is provided below:

$$\nu_{ij} = -\frac{S_{ij}}{S_{ii}} \quad (2.16)$$

Most materials naturally shrink orthogonal to an applied tension, this leads to positive values for Poisson's ratio, with a hypothetical maximum of 0.5. Normal values for several materials are in the range of 0.2-0.3, although negative values are also recognized.

## 2.4.2 Dynamic Method

The dynamic technique applies to a trajectory of arrangements taken from a molecular dynamic's simulation. The dynamic method applies a range of strains (or stresses) in a specific direction and calculates the consequent average stress (or strain) at, for example, constant temperature. Parrinello and et. al (1982) [43] proposed the simplest method when simulations have been conducted in the constant stress ensemble. The canonical ensemble provides fixed temperature, the microcanonical ensemble provides constant energy[44];

### **2.4.3 Ensemble Detail**

A statistical ensemble is a collection of some similarly provided by systems under similar thermodynamic or macroscopic conditions. Ensembles are identified by three separate thermodynamic variables that are constant in the system, as described below;

NVE is known as a microcanonical ensemble. It indicates that volume (V), Energy (E) and the number of particles (N) are constant in MD simulations. This ensemble is applied to control the conservation of total energy in a defined time step.

NVT is also called a canonical ensemble. In this method, the system is equilibrated at a specified value through applying thermostat algorithms, while the total energy (E) of the system can fluctuate.

NPT refers to the isobaric-isothermal ensemble. In this method, the volume of the system is allowed to fluctuate during the thermodynamic equilibrium process while the

pressure and temperature are fixed at specific values. The method is appropriate for chemical reactions simulation at constant pressure conditions.

We need to control the thermodynamic conditions in the simulation process such as the pressure and the temperature to examine the simulation results with the experimental observation. The temperature is controlled by the Langevin thermostat [45]. In this process, when the temperature drifts outside of the specific range, the atomic velocities are returned into the target range.

Pressure in an MD simulation is controlled by applying Parinello, Andersen, Nose and Berendsen methods [46]. In the Parinello method, the volume and shape of the cell are allowed to change till the internal stress of the system is equal to external stress, the Andersen and Nose method, only allows the volume to be changed and in the Berendsen approach, the coordinates of the particles are allowed to change while the shape and dimension of the cell are fixed [47].

#### **2.4.4 Elastic Moduli of Polycrystalline Materials**

As defined by the stiffness matrix of a crystal, it is possible to calculate the elastic moduli of a polycrystalline material. There are three distinct notations as described by Reuss, Voigt, and Hill [39]. The Voigt notation is defined according to an assumption that the strain field remains constant during an arbitrary average stress load. In contrast, the Reuss notation is determined according to an assumption that the stress field remains constant during an arbitrary average strain load. A typical simplistic approach uses the

average of the Voigt and Reuss definition to measure the effective moduli which call the Hill average. This method is relatively accurate when all components of elastic moduli are roughly the same values [39]. The following equations are definitions of the Reuss and Voigt expression, while, the Hill is defined as the average of the other two.

$$K_{Voigt} = \frac{1}{9}(C_{11} + C_{22} + C_{33} + 2C_{12} + 2C_{13} + 2C_{23}) \quad (2.17)$$

$$K_{Reuss} = \frac{1}{(S_{11} + S_{22} + S_{33} + 2S_{12} + 2S_{13} + 2S_{23})} \quad (2.18)$$

$$G_{Voigt} = \frac{1}{15}(C_{11} + C_{22} + C_{33} + 2C_{44} + 2C_{55} + 2C_{66} - C_{12} - C_{13} - C_{23}) \quad (2.19)$$

$$G_{Reuss} = \frac{15}{4(S_{11} + S_{22} + S_{33} - S_{12} - S_{13} - S_{23}) + 3(S_{44} + S_{55} + S_{66})} \quad (2.20)$$

Where K is the Bulk modulus and G is the shear modulus.

## 2.5 Theory in an Amorphous Cell

Modelling or simulation usually begins with the designation of an initial composition. For crystalline materials, this simply requires inserting the correct lattice parameters, which guarantee the short and long-range arrangements. On the other hand, for amorphous materials, the long-range arrangements would be ignored, thus, a specific construction algorithm is required to satisfy short-range correlation, without proposing long-range arrangements.

In particular for polymers, the formational distribution in the amorphous arrangement is different compared to a crystal structure. Furthermore, the relaxation of crystalline as a

liquid form is a very slow process. As a result, simply melting a polymer crystal will not occur in realistic initial structures.

To build realistic arrangements for polymers in the condensed phase the torsional degrees of freedom play a critical role. Many polymer designs neglect all degrees of freedom except the torsions around the backbone bonds. The famous Rotational Isomeric State (RIS) method [48], simplifies formation by assuming that torsions will only occur in the construction process. On the other hand, an amorphous cell used the same method by applying a force field. We will use this approach to create an initial amorphous structure.

## **2.6 Software Packages**

Recently, multi-purpose DFT and MM software packages have been established which can apply to different size systems. This allows researchers to focus on larger systems with the use of supercomputing [25]. VASP (Vienna ab-initio simulation package) [49] is a well-known commercial package for solid-state physics based on DFT. This program utilizes pseudopotentials and plane-wave basis sets. VASP package was used for DFT calculation. LAMMPS (Large-scale Atomic/Molecular Massively Parallel Simulator) [36] is free and open-source software, LAMMPS is a classical molecular dynamics program. It can be used for numerous modelling applications such as a crystalline or amorphous system, polymer structures, molecular mechanics MM, molecular dynamics. In this research, it was used for MM and MD simulations.

Molecular modelling and availability of higher computational methods provide a new low-price approach for understanding the principal interaction of new materials that is an advantage in materials science or interdisciplinary science. Therefore, in the next chapters, we are using the right computational methods to a better understanding of the energy absorption mechanism at the atomic level of the polyurethane reinforce by Halloysite nanotube.

## Halloysite Nanotubes

Computer simulation is an efficient mechanism to investigate molecular-level properties, and it has been successfully applied to many physical properties of clay mineral systems including the mechanical response [42], [50] and interlayer formation [51], [52]. We apply computer simulation to study the properties of Halloysite as a function of geometry and size simultaneously.

The chapter is organized as follows. After a review of the literature related to Halloysite nanotubes in section 1, Lattice parameters of Halloysite were calculated by the DFT method in section 2. Next, we will investigate the rolling mechanism of Halloysite nanotube with Molecular Mechanic in Section 3, then, atomic simulation with DFT, MM and MD methods will be performed to calculate the elastic properties of Halloysite. The results including the effects of temperature and rolling on young's modulus and Poisson's ratio are discussed in Section 4. Finally, we will calculate the cohesive energy for the interfaces between Halloysite layers by the DFT approach in Section 5.

### 3.1 Literature Review

Halloysite nanotube (HNT) has become an interesting natural nanoparticle for researchers due to inexpensive nanoparticles and availability in several regions. Also, it is a reliable and compatible particle that can enhance polymer functionality. Halloysite is

basically a mineral alumina-silicate ( $\text{Al}_2\text{Si}_2\text{O}_5(\text{OH})_4 \cdot 2\text{H}_2\text{O}$ ) composed of a two-layer structure, where the exterior structure is composed of siloxane, and the inner structure consisted of alumina. Halloysite forms tubes with a length of 600–1000 nm and an internal radius of 12-30 nm, an external radius of 30-100 nm as shown in Figure 3. 1 [12][53].

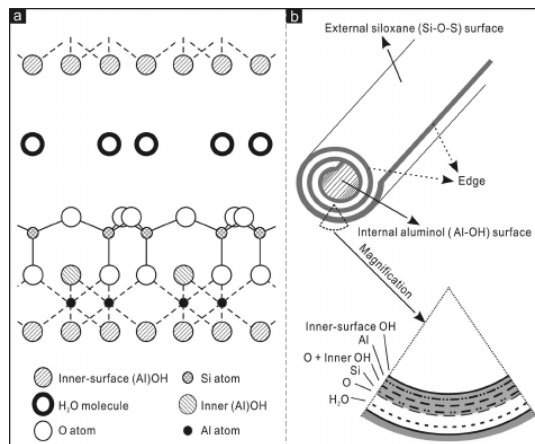


**Figure 3. 1:** Schematic of Halloysite structure [53]

The interlayer water molecules, held by weak hydrogen bonds, shown in Figure 3. 2;

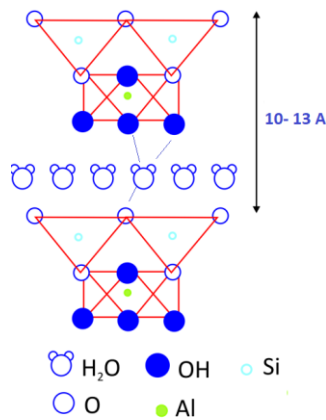


**Figure 3. 2:** the hydrogen bonds between interlayers HNT

The inner cylindrical hollow of Halloysite can store and release other molecules, for example, drugs, proteins, and anti-corrosion, antioxidants, and flame-retardant material,

for hours or months. Thus, Halloysite is a good candidate for purposes such as regenerative medicine, drug delivery, and self-healing polymeric composites. Additionally, Halloysite tubes with clogging at the ends can extend the release time of stored molecules, while opening the ends of Halloysite tubes works like a catalysis function by exposing the interior and exterior surfaces of the Halloysite tubes [54].

Most research on Halloysite has concentrated on measured mechanical properties under different loading [55]. Lu et al. (2010) experimentally measured the Elastic modulus. They found that the Elastic modulus of the HNT layer is  $130 \pm 24$  GPa [56]. Lvov et al. (2008) calculated Young's modulus of a multi-wall alumino-silicate nanotube. They obtained Young's modulus (230–340 GPa) [54]. Guimaraes et al. (2010) calculate the young modules of different arrangements of HNT nanotubes by applying DFT. They obtained that Elastic modulus in the range 230–300 GPa for zigzag arrangement and 300–340 GPa for armchair arrangement [10]. Moreover, the Elastic modulus of HNT declines with a growth radius. Also, other researchers found that HNTs are significantly flexible [57].

### **3.2 The Lattice Parameter of Unit Cell of HNT**

DFT has been used to find the equilibrium structure of the Halloysite unit cell. For this purpose, we are using DFT analyses of the local structure of single a repeating unit of Halloysite (Figure 3. 3) to find lattice parameters of the unit cell of HNT through the minimization of total energy. The structure was relaxed with a conjugate gradient algorithm

[58] until the energy components on any ions were smaller than 0.01 eV. The primitive cell of Halloysite was obtained from reference [59].

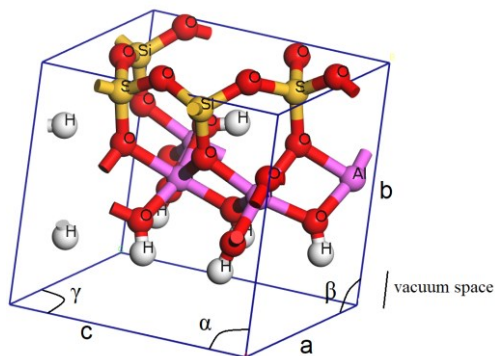


**Figure 3. 3:** lattice parameters of single repeat unit Halloysite (Hal-sing) [59].

DFT was carried out with VASP [49] with the PBE gradient-corrected functionals [21] methods. The calculation was performed at zero temperature. Reciprocal space was represented by Gamma k-points scheme with 5x5x5 grid meshes. There are 34 atoms in the unit cells (See Figure 3. 3). The structures are relaxed without symmetry constraints with a cut-off energy of 750 eV. The projector augmented wave (PAW) pseudopotential [26] was applied for describing the core electrons interactions. Figure 3. 4 shows the energy verse lattice parameter b of a single repeat unit Halloysite.

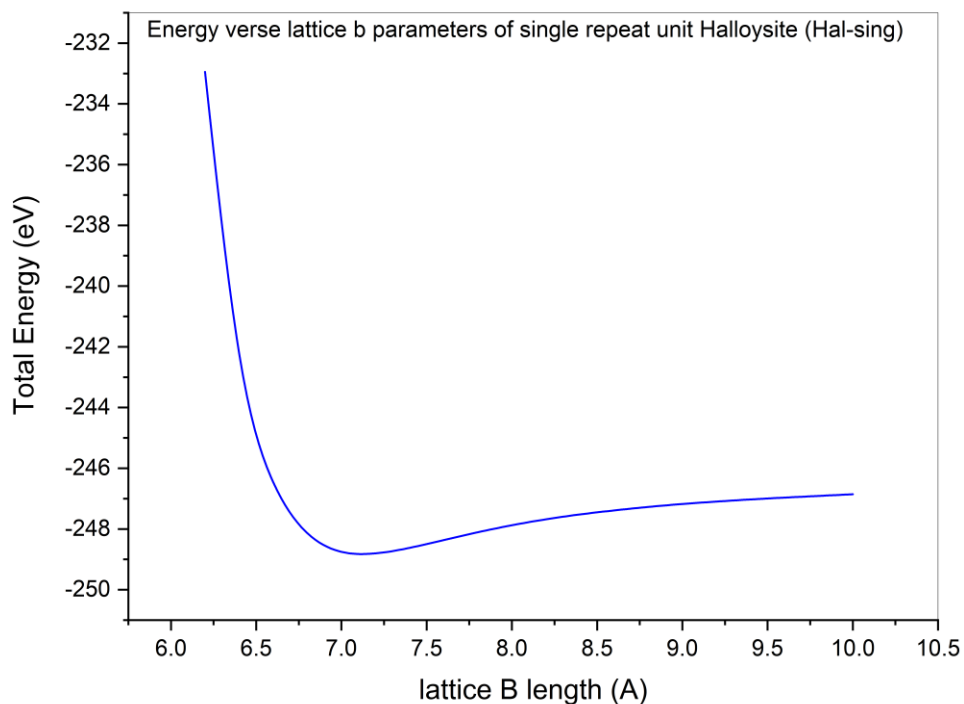


**Figure 3. 4:**Energy verse lattice b parameters of single repeat unit Halloysite (Hal-sing)

Table 3. 1 presented previous experimental and computational results of lattice parameters of the unit cell of Halloysite with the current geometry optimization

**Table 3. 1:**Computed and experimental lattice parameters of PBC optimization; parentheses are shown percentage deviations. Data are reported in Å and degrees

	MM [57] ClayFF	MM [57] PMMCS	DFT [57] B3LYP	DFT [60] B3LYP	DFT [61] B3LYP	Experimental [62]	DFT this work PBE
a (Å)	5.143(0.5)	5.134(0.7)	5.206(0.7)	5.184(0.3)	5.230 (1.2)	5.17	5.11314
b(Å)	7.299(1.4)	7.322(1.0)	7.323(1.0)	7.396(0.1)	7.480 (1.1)	7.40	7.30867
c(Å)	5.210(1.2)	5.164(0.3)	5.192(0.8)	5.190(0.8)	5.210 (1.2)	5.15-8.94	5.45623-8.857
$\alpha$ (Deg)	84.08(0.2)	82.82(1.7)	84.08(0.2)	83.50(-0.9)	84.10 (0.2)	84.23-91.69	84.5556
$\beta$ (Deg)	98.97(0.3)	99.52(0.8)	99.05(0.4)	99.80 (1.1)	98.80 (0.1)	98.70-104.61	99.9974
$\gamma$ (Deg)	60.40(0.8)	60.12(0.3)	59.89(0.1)	59.90 (0.0)	59.92(89.2)	-	61.0147

This discrepancy is due to the pseudopotential, k-point and cut-off energy in the compute process of the simulated systems and different algorithms.

### **3.3 Computational Method of Rolling Mechanism and Discussion**

Mineralogists have explained the structure of the Halloysite nanotube is directly formed of Halloysite layers. HNT can be experimentally generated of kaolin clay in water for a long time by joining a detergent [11]. They used a one-step method through the dispersion of the kaolinite in methanol and mixing by several alkyl trimethylammonium salts and 1-hexadecyl-3-methylimidazolium chloride for 1 day. After that, the samples were washed then heat treatment was conducted to cause the formation of the nanoscrolls [11]. One of the common explanations of the rolling mechanism is geometric influence such as Si–O tetrahedra arrangement on the external face of HNT, or surplus length of the Al-dioctahedral layer over the length of Si-tetrahedral layer.

The microscopy observation has shown Halloysite formation of kaolinite [62]–[64]. These experimental researches have exposed a key role of the rolling of the Halloysite layer [65]. Usually twisting axis is orientated in the crystalline c-direction, some examples twisted around ac-axes [65]–[67] as displayed in Figure 3. 5.

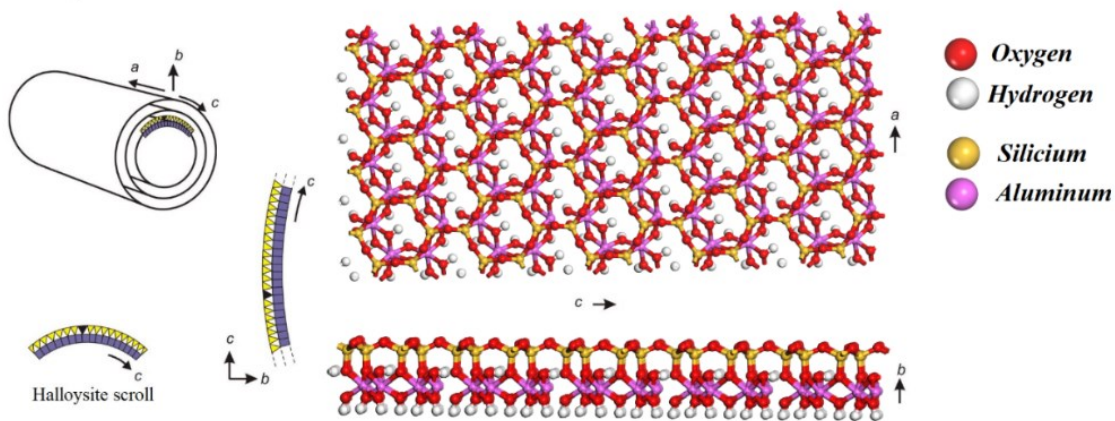


**Figure 3. 5:** Schematic of Nanosheet and Nano scroll form an HNT [59]

This type of geometric model of the natural rolling of the Halloysite samples sheet provides a qualitative description of the geometry formation. On the other hand, the influence of external conditions (temperature, pressure) on the geometry and energy of the Halloysite must be taking into consideration on microscopic forms, besides chemical arrangement and chemical bonding which are required to get insight into the nature of the rolling of the Halloysite layer as shown in Figure 3. 6.

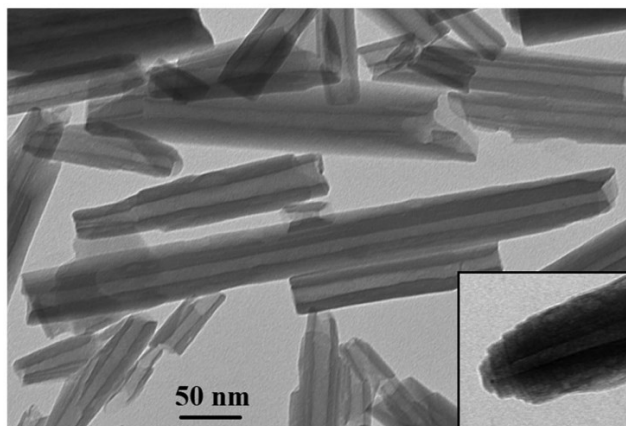


**Figure 3. 6:** Transmission electron microscopy image of Halloysite nanotubes [11]. copyright permission to reuse this image was obtained from the publisher.

Some previous computational studies of Halloysite concentrated on the electronic properties with using the simplified HNT structure, for example, the study on the single-walled Halloysite nanotube [10], [68]–[70], Halloysite nano scroll with overlapping arms [71], [72] and two slab surface arrangement [57]. In those studies, the researchers mainly were used as a pre-defined structure then allowed the structure to be optimized.

Here, by using computational approaches that are classical molecular mechanic (MM) simulations, we evaluated the structure of the Halloysite nanotubes. To study the rolling mechanism of the Halloysite, All the MM simulations are performed using the LAMMPS [35] package, which allows us to examine the configuration model based on the type of the used potential. In this section, because of computational accuracy, we used the polymer consistent forcefield (PCFF) with interface extension (PCFF-IFF) [32], [33], [73]. Also, we used the particle-particle, particle-mesh (PPPM) algorithm with a relative force accuracy of  $10^{-5}$  [74] and a real-space cut-off of 18 Å.

In the previous literature, the configuration of Halloysite is related to the rolling process around the c-axis, but rolling around the ac-axis is also possible (see Figure 3. 7) [11].

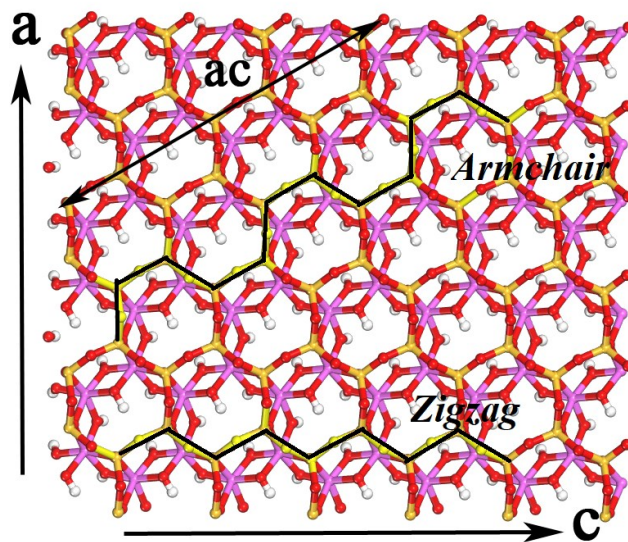


*Figure 3. 7: Schematic diagram showing zigzag and armchair of Halloysite*

The unit cell employed in molecular mechanic simulations has been provided as follows. The primitive cell of Halloysite was obtained from ref. [59]. In our simulation, we applied a supercell including 24480 atoms. It was generated by replicating 30 and 24 unit cells along with a and c crystal axes, respectively, then, we removed the periodic boundary conditions to provide a zero-stress boundary condition as seen in Figure 3. 8. We performed structure optimization applying the conjugate gradients algorithm [58] as performed in the LAMMPS package.

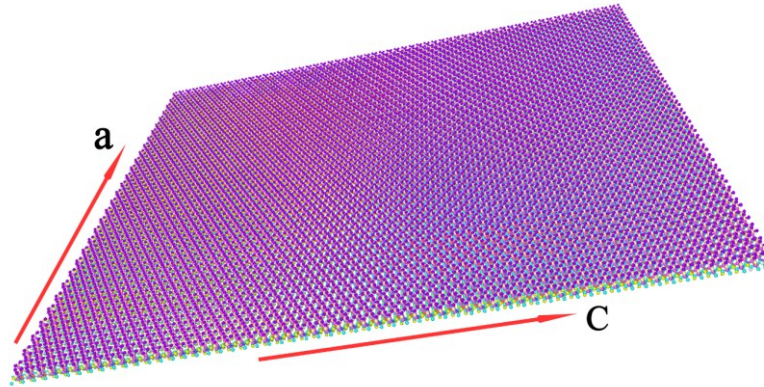


**Figure 3. 8:** supercell including 24480 atoms ( $156.4 \times 212.6 \text{ \AA}^2$ )

As a result, the twin rolling of the layer occurs as shown in Figure 3. 9. The rolling axis is bent toward of ac axis, which is illustrated rolling around Armchair arrangement as described in Figure 3. 7.

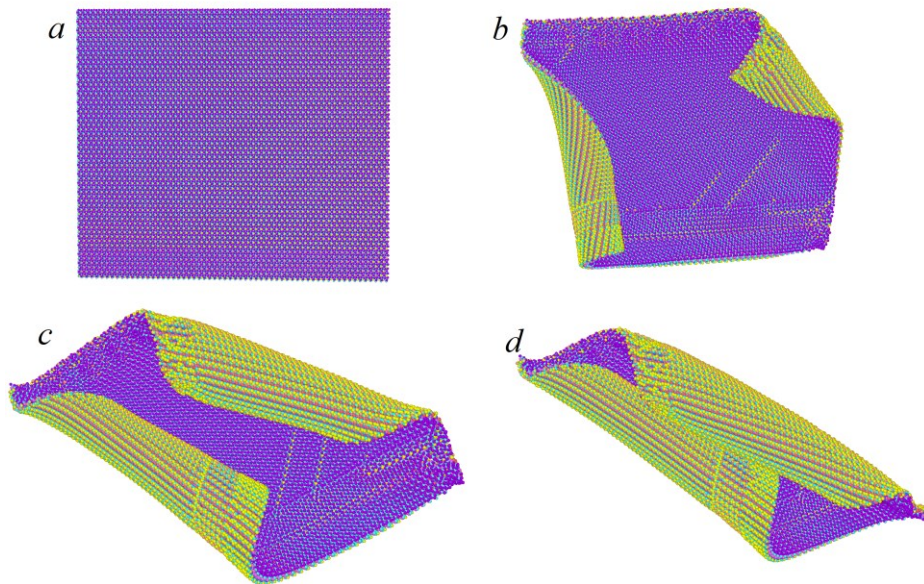


**Figure 3. 9:** molecular dynamics simulations of twin rolling of the layer of Halloysite, (a) 0 ps, (b) 2 ps, (c) 3 ps and (d) 5 ps.

An experimental result of previous research can verify the molecular dynamics simulations. We used Atomic Force Microscopy (AFM) imaging of Halloysite nanotubes

of ref [11]. Prishchenko and et al (2018) [11] used the Peak Force Tapping technique to capture topography images as depicted in Figure 3. 10. These experimental morphologies sufficiently verify our computational model base on an appropriate choice potential. Although the dimensions of this nanotube are larger than our simulation.

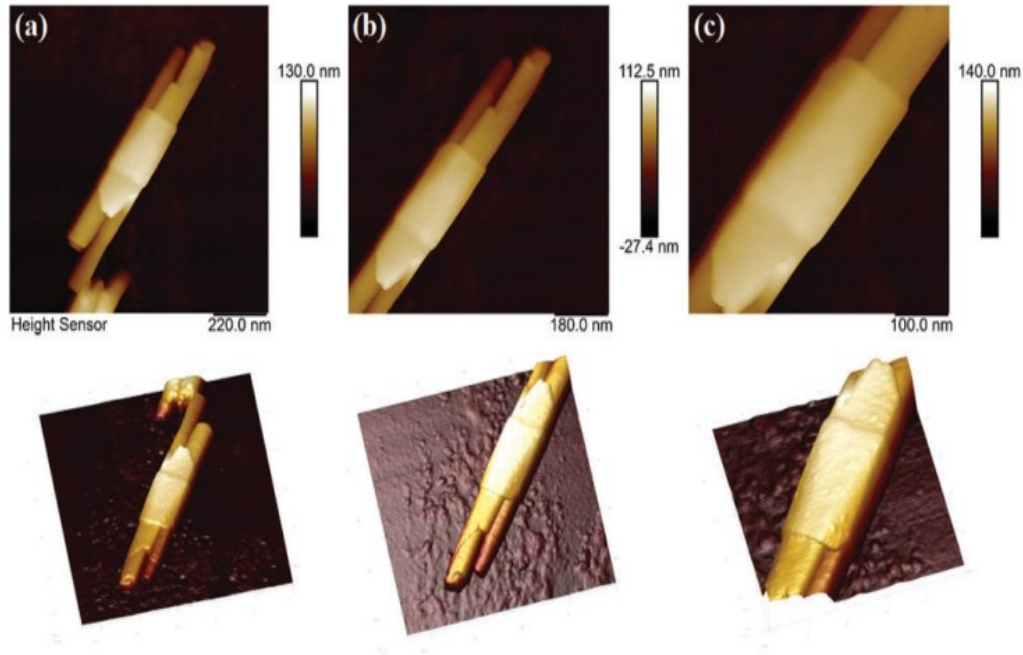


**Figure 3. 10:** AFM images of Halloysite nanotubes [11]. copyright permission to reuse this image was obtained from the publisher.

The single Halloysite nanotube can be generated from the smaller initial layer as described in Figure 3. 11. A supercell was created of 18 and 15 replicated unit cells along a and c crystalline axis, respectively. Then, we applied molecular mechanics to optimize the structure by the conjugate gradient algorithm [36]. We can observe that the horizontal geometry of the HNT layer is unstable and rolling starts at corners. The rolling axis is bent toward the Armchair axis, which is compatible with the experimental result demonstrated in Figure 3. 12 [11]. We can see if the initial structure is somewhat near to square sheet, a

twin nanotube would be tack place, in contrast, a rectangular initial structure generates a single nanotube. However, the final configuration of both is rolled around the diagonal of the layer. One primitive explanation for rolling is that the bond lengths of Al-dioctahedral and Si-tetrahedral layers are different.

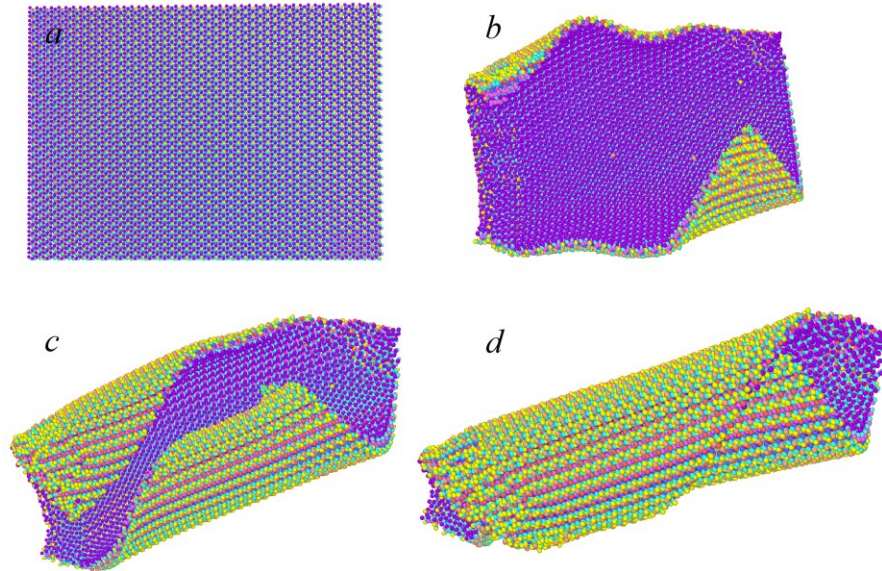


**Figure 3. 11:** The rectangular supercell model has 93 nm 132 nm elongated in a and c directions exhibited in the structure of twisted formations with a diameter of 15 nm. (a) 0 ns, (b) 2 ns, (c) 3 ns and (d) 5 ns.

We also used the image of ref [11] that shows the spiral ending of a single Halloysite nanotube (Figure 3. 12).

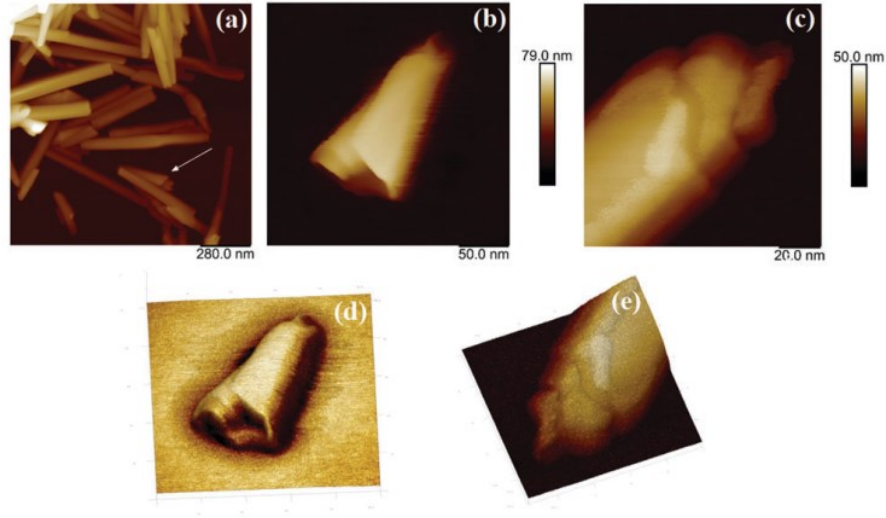


**Figure 3. 12:** single Halloysite nanotube [11]. copyright permission to reuse this image was obtained from the publisher.

According to the results obtained from the MM simulations, it is necessary to consider different types of the potential of the primary Halloysite layer and the effect of formation. We left this for future studies.

### 3.4 Mechanical Properties of the HNT (Atomic Simulation)

According to Section 2.4, in this section, we study the mechanical properties of the HNT by applying static and dynamic methods [38], [39].

#### 3.4.1 Static Approach

The static approach ignores the fluctuations which happened due to thermal movement. This technique is usually applied to a geometry optimized structure. Analytical calculation on the response in an optimized structure by using the cell Hessian matrix, or by applying a small and finite strain. As introduced in section 2.4.1.

In our case, DFT and MM simulations have been used to calculate the mechanical properties of HNT with a defined structure cell. In DFT, we are using a single repeating unit of Halloysite which there are 34 atoms in the unit cells (See Figure 3. 3) [59]. DFT method was carried out with the plane wave (PW) methods [75] to simulate the mechanical properties of Halloysite. The calculation was performed at zero temperature. Reciprocal space was represented by 3\*3\*3 centred k-points grid meshes. The structures are relaxed without symmetry constraints with a cut-off energy of 650 eV. The result is provided in Tables 3.2 and 3.3.

In order to obtain the mechanical properties of HNT with MM, simulations were performed on a flat surface of HNT. The mechanical properties of the slab surface were calculated under different input variables. With this aim, all simulated HNTs were set up under finite uniaxial tensile loading at a constant temperature and the maximum strain amplitude was 0.01. The slab surface of HNT, consisting of supercell was generated from 18\*15 optimized unit cells of HNT including 9180 atoms (132 Å \*92 Å) as illustrated in Figure 3. 8. The calculation was performed at zero temperature. The Dreiding, PCFF and COMPASS potential energy functions are used [28]–[33]. The result is provided in Tables 3.2 and 3.3.

Elastic stiffness constants obtained from the static method at  $T = 0$  K are reported in Tables 3.2 and 3.3. Elastic moduli were calculated by assuming triclinic symmetry and determining the tensor and subsequently, the elastic moduli, as described in section 2.4.1.

**Table 3. 2:** Elastic constants of halloysite calculated by the MM and DFT approach, (Subscripts 1, 2 and 3 referred to X, Y and Z of Cartesian coordinates system.

	atoms	<b>C<sub>11</sub></b> (xxxx) (GPa)	<b>C<sub>22</sub></b> (yyyy) (GPa)	<b>C<sub>33</sub></b> (zzzz) (GPa)	<b>C<sub>12</sub></b> (xxyy) (GPa)	<b>C<sub>13</sub></b> (xxzz) (GPa)	<b>C<sub>23</sub></b> (yyzz) (GPa)	<b>C<sub>44</sub></b> (yzyz) (GPa)	<b>C<sub>55</sub></b> (xzxz) (GPa)	<b>C<sub>66</sub></b> (xyxy) (GPa)
HNT (DFT)	15	201.282	57.667	40.493	24.1712	10.901	52.587	3.549	22.725	27.339
HNT (MM Dreiding FF)	24480	136.164	0.637	152.12	19.300	31.877	7.400	4.453	53.949	14.873
HNT (MM PCFF FF)	24480	53.736	7.559	113.389	37.515	102.008	22.578	13.454	63.1054	33.227
HNT (MM COMPASS FF)	24480	202.960	26.674	17.862	103.003	32.909	71.459	48.017	11.187	98.679

**Table 3. 3:** Mechanical; properties of the single Halloysite sheet with assuming the material is isotropic and using Vigot and Reuss notation through the molecular mechanic and DFT simulation

	Atoms	Bulk Modulus (GPa)	Young modulus (GPa)	Poisson's ratio $\nu$	Elastic moduli $E_1(\text{xx})$ (GPa)	Elastic moduli $E_2(\text{yy})$ (GPa)	Elastic moduli $E_3(\text{zz})$ (GPa)
B Lecouvet et al [50]			60-240				
Dong Lu et al [51]			$130 \pm 24$				
HNT (DFT)	15	80.9325	68.6398	0.3587	154.805	44.990	288.37
HNT (MM Dreiding FF)	24480	45.112	73.695	0.228	312.2601	31.029	142.485
HNT (MM PCFF FF)	24480	55.432	60.144	0.319	124.796	43.468	139.849
HNT (MM COMPASS FF)	24480	73.582	88.953	0.298	109.544	7.215	74.481

Generally, applying PCFF represents good agreement with DFT result in the static approach for instance  $C_{66}$ , However, there are some overpredict amounts for example ( $C_{11}/C_{22}$ ) at  $T = 0$  K. Lecouvet et al (2013) [55] estimated Young's Modulus slightly higher than our DFT and PCFF results. Presumably, this difference correlated different algorithms to simulation non-bonded interaction in different potential and charged atoms which are constants in MM, but it could be flexible in the relaxation process in DFT calculations, k-point and cut-off radius in the computing process.

### 3.4.2 Dynamic Approach

The dynamic approach examining the elastic moduli through applying a constant strain in a specific direction and calculate the consequent average stress at, for example, constant temperature to an arrangement. In our case, uniaxial tensile with the constant strain rate was applied for all models at a constant temperature and the elastic modulus was calculated from corresponding stress-strain curves. See section 2.4.2.

Various atomic arrangements are available to Halloysite nanotubes, which are defined by the cylindrical and flat surface [68]–[70]. The proper arrangement allowing the effective analyst and reduced assumptions. In the following section, the molecular dynamics simulation approach is applied to study mechanical properties for a different arrangement of Halloysite structure.

#### **Model 1:**

Atoms in a Halloysite are organized within different layers, consequently, it has anisotropic mechanical properties. To study anisotropic mechanical properties, a periodic supercell was created by the replicating layer of HNT as introduced in Figure 3. 11(a). The model was created with 1080-unit cells and 36720 atoms ( $18 \times 15 \times 4$  along with OA, OC, and OB directions respectively). After the creation of a multilayers structure of the Halloysite sheet structure, the boundary condition was removed then energy minimization was conducted. It was continued until the subsequent difference energy steps are less than  $10^{-4}$  kcal/mol. Then an equilibration process was carried out for 40 ps through an NPT ensemble at constant 300 K temperature and 1.0 atmosphere pressure. During this time, we

monitor the density of the system until it reaches a stable value as shown in Figure 3. 14. To analyze the strain rate influences on mechanical properties the model was deformed with three strain rates ( $1 \times 10^8$ ,  $1 \times 10^9$  and  $1 \times 10^{10} \text{ s}^{-1}$ ) along OA axis. Also, as illustrated in Figure 3. 15, three uniaxial tension tests were conducted along crystal axes. The models were deformed at 300k temperature with a strain rate equal to  $10^9 \text{ s}^{-1}$  with 0.1 fs time step. We used the PPPM method with  $10^{-5}$  force accuracy [74].

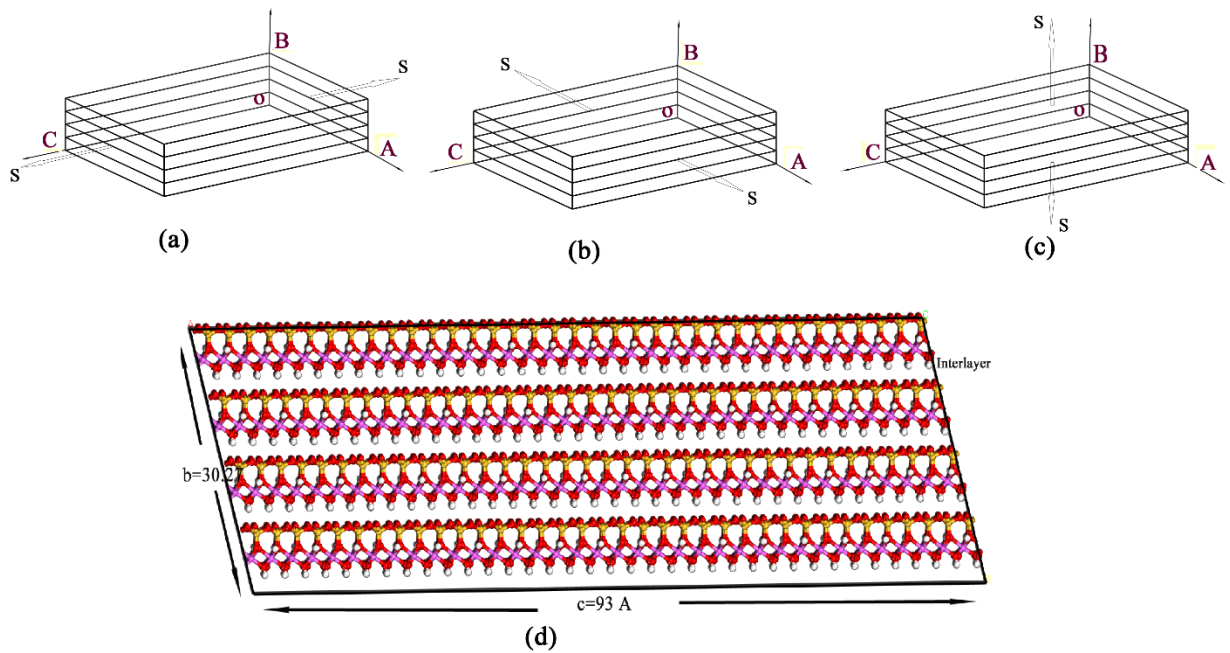


**Figure 3. 13:** Schematic of loading direction (a) OA axis (b) OB axis (c) OC axis (d) The simulation cell of HNT is arranged into four layers, silicon (yellow) aluminum (pink). Oxygen and hydrogen atoms are displayed

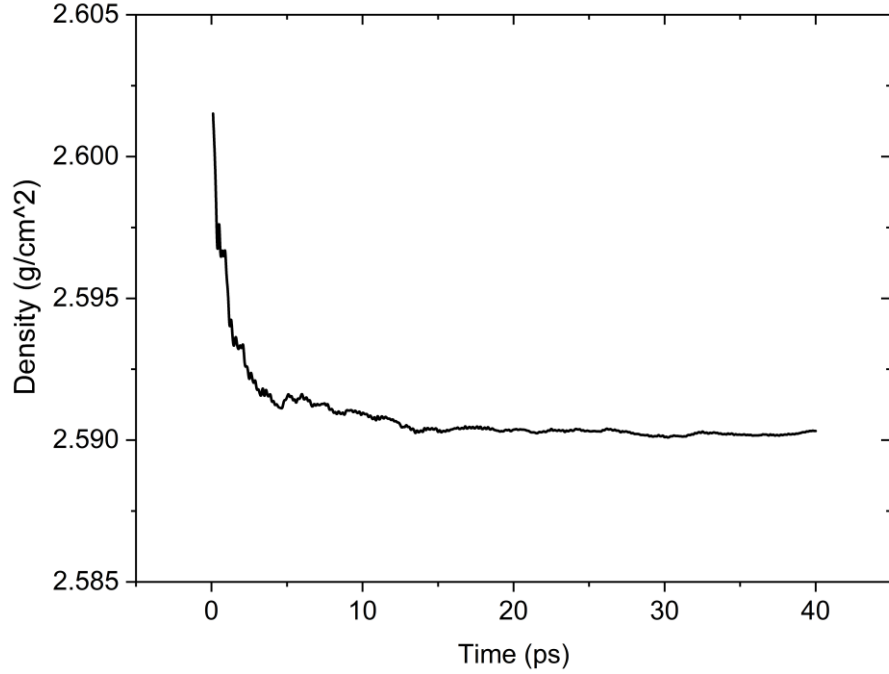


**Figure 3. 14:** Density of models during the relaxation process

To determine Young's modulus, an available approach is applying a small strain to a structure then calculating the elastic modulus of the stress-strain curve by using equation 3.1:

$$\sigma = \frac{\partial U}{\partial \varepsilon} = D\varepsilon^2 + E\varepsilon + C \quad 3.1$$

Where D refers to the third-order elastic modulus, E refers to Young's modulus, and C refers to the residual stress[76] with fitting to a quadratic form we calculated Young's modulus. It can be obtained from a fitted straight line to the stress-strain curve if the deformation is small enough. In our case, the strain that is less than 0.04 can be described as the linear elastic regime. In order to study strain-rate sensitivity on the stress response, we used incremental changes in strain rate during the deformation process at the same configuration and the same temperature, to determine corresponding differences in the

result. The results in Figure 3. 15 depict the deformation response of model 1 with three strain rates ( $1 \times 10^8$ ,  $1 \times 10^9$  and  $1 \times 10^{10} \text{ s}^{-1}$ ) along the OA axis . According to the result of Figure 3. 15, with decreasing strain rate from  $1 \times 10^9$  to  $1 \times 10^8 \text{ s}^{-1}$  the deformation response approaches the same result. Therefore, the strain rate  $1 \times 10^9 \text{ s}^{-1}$  is appropriate for the next step of deformation. In addition to, Figure 3. 16 depicted deformation along three axes.

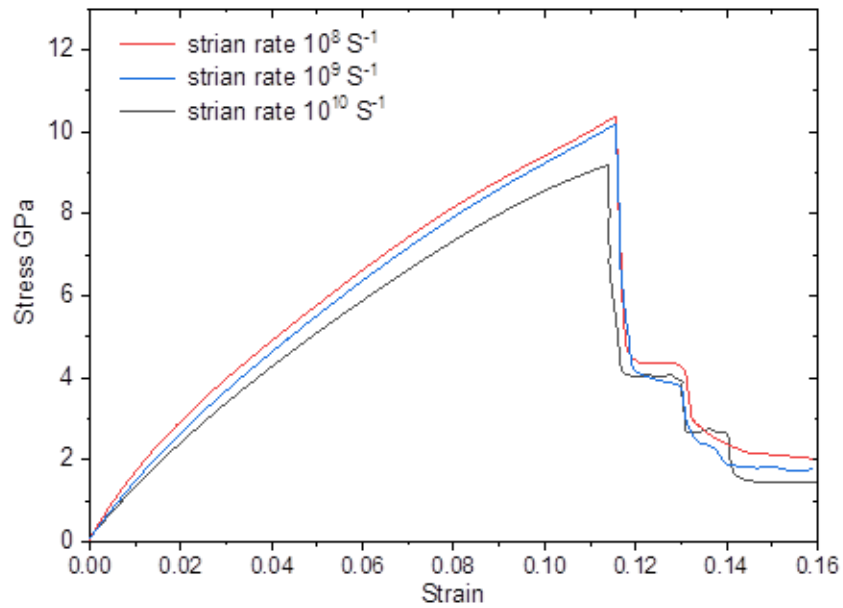


**Figure 3. 15:** Stress-strain curves for three strain rates ( $10^8$ ,  $10^9$  and  $10^{10} \text{ s}^{-1}$ ) along the OA axis

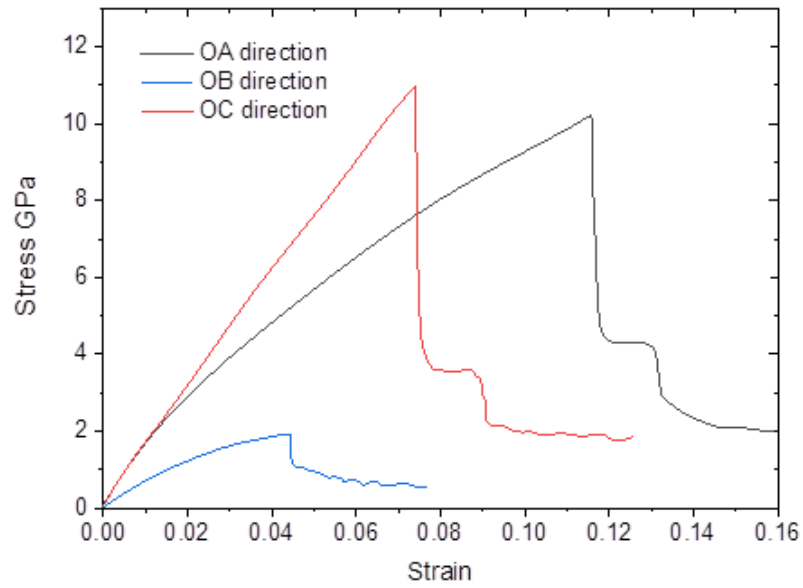


**Figure 3. 16:** Stress-strain curves for three perpendicular loading directions (along with OA, OB and OC axis)

In this classical force field, bonds can be stretched, twisted and interacts with the other atoms or molecules in the neighborhood, but cannot be broken. Thus, the failure states are more challenging through applying PCFF-IFF. Therefore, the methodology of Hua Yang and et al [77] was selected to determine the failure process of the system. According to their definition, the failure state was defined as the cutoff distances for bond breakage. Similarly, we employed a radial distribution function (RDF) to specify the criteria to define the break of individual bonds. When the first smallest value of the RDF curves arrives mean the possibility of detecting atom pairs with the detachment length is approximately zero. Hence, we used this assumption that the bond is broken if the length between atom pairs is larger than this amount. This allows Halloysite bonds to be broken in model 1 of MD simulation without using quantum mechanics. Figure 3. 17 displays the radial

distribution function and table 3.4 is listed the cutoff distances for bond breakage. Figure 3. 18-20 illustrated axial simulation test for model 1 for 3 perpendicular directions.

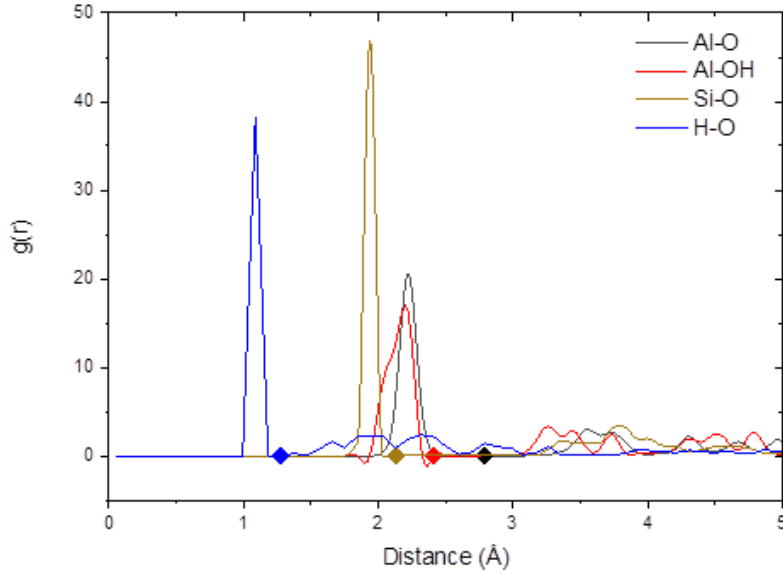


**Figure 3. 17:** radial distribution function (RDF) bond types in the Halloysite and the first minimum

**Table 3. 4:**List of bond and cutoff distance based on the minimum valve in the RDF result

<b>Bond Type</b>	<b>Cutoff distance (Å)</b>	<b>Cutoff distance (Å) [77]</b>
<b>Al-O</b>	2.88	2.74
<b>Al-OH</b>	2.43	2.66
<b>Si-O</b>	2.03	1.84
<b>O-H</b>	1.18	1.24

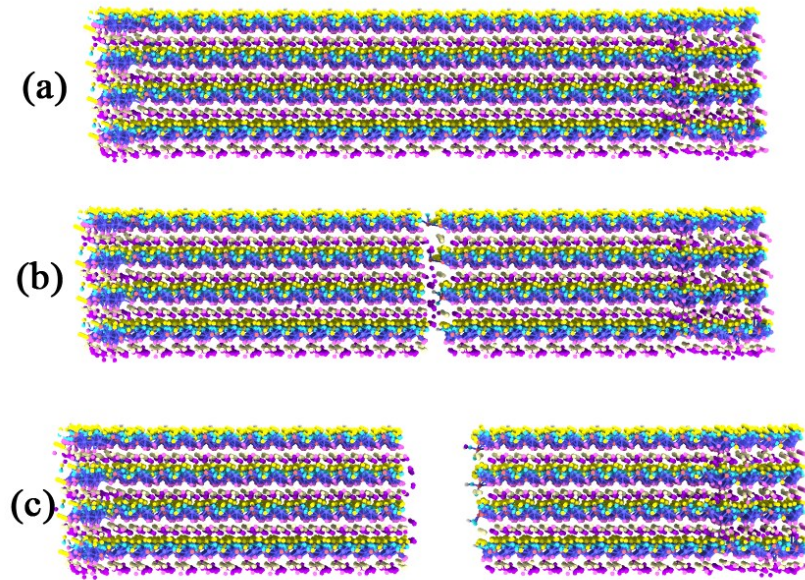


**Figure 3.18:** Fracture process for Halloysite nanosheet (model 1) in OA direction

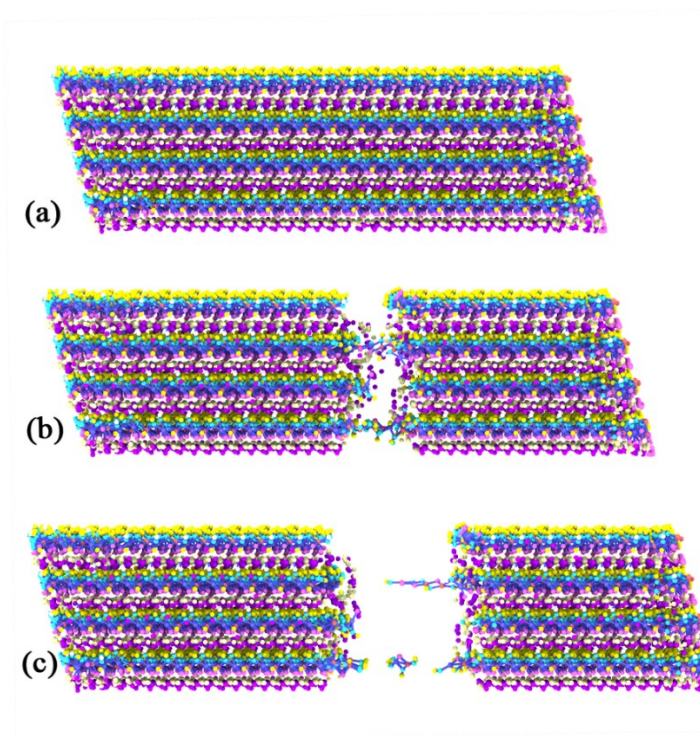


**Figure 3.19:** Fracture process for Halloysite nanosheet (model 1) in OC direction

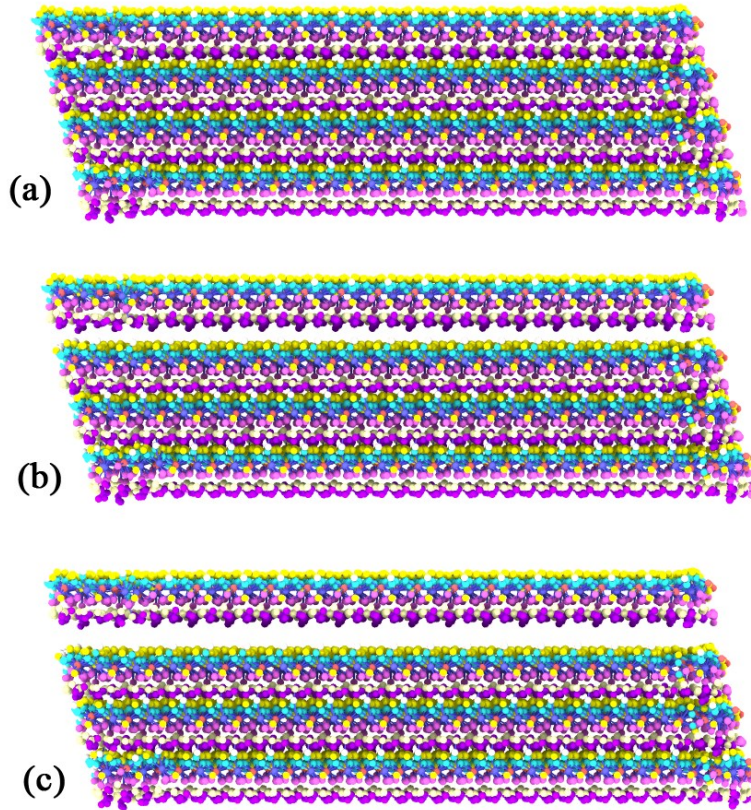


**Figure 3. 20:** *Fracture process for Halloysite nanosheet (model 1) in OB direction*

In model 1 of the HNT arrangement, the linear elastic regime of stress-strain curves of Figure 3. 16 was used to obtain Young's moduli. Thus, Young's moduli are 118, 148, and 42 GPa at OA, OC, and OB directions, respectively. As presented in Figure 3. 16, the tensile strain of the Halloysite nanolayer are 0.079, 0.118 and 0.042 at OA, OC, and OB directions, respectively, this result is in agreement with the tensile strain reported by Yang[77] and Yendluri [53] which is  $0.08 \pm 0.04$ .

### **Model 2:**

In addition, the MD method is used to study the influence of zigzag (ZZ) and armchair(ac) arrangement on the mechanical properties of Halloysite nano scroll. To this

purpose, the pre-rolled models were generated from 18\*15 optimized unit cells of HNT including 9180 atoms and rolled with a 12 Å radius as displayed in Figure 3. 21. [78] Then geometry optimization by using conjugate gradient [76] methods was conducted and it was continued until the subsequent difference energy steps are less than  $10^{-4}$  kcal/mol. Then the structure was equilibrated with an NPT ensemble at 1 atm pressure and 300 K for 50 ps. Then all models HNTs were deformed along the tube axis at 300k temperature with a strain rate equal to  $10^9$  s<sup>-1</sup>. All simulations were incorporated with a canonical NVE ensemble with 0.1 fs time step. We used the PPPM method with  $10^{-5}$  force accuracy[74]. In this section, to avoid the effect of the cutoff radius, Lennard Jones cutoff radius is chosen as 18 Å[79]. LAMMPS is used for all the MD simulations[36]. PCFF-IFF has been used for both arrangements[32], [33]. The results are presented in Figure 3. 22.

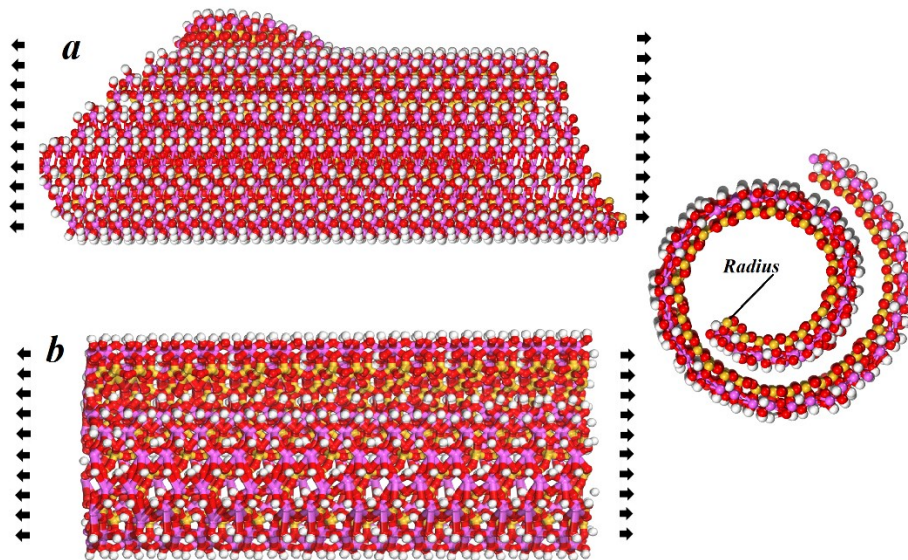


**Figure 3. 21:** The structure of HNT (a) armchair HNT, (b) zigzag HNT

For the rolled Halloysite models, the stress-strain result obtained from the dynamic method at  $T = 300$  K is provided in the following graph.

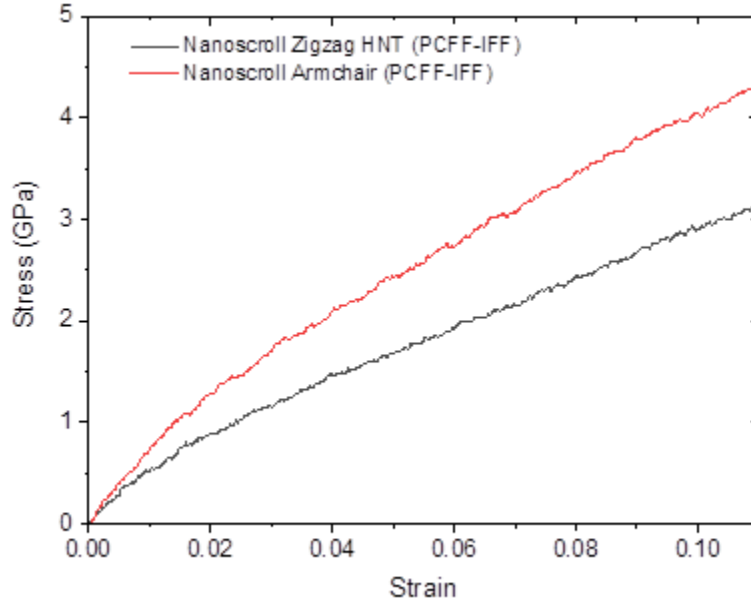


**Figure 3. 22:** Stress-strain curves of the armchair (ac) and zigzag (ZZ) HNT

At this step, we estimated Young's modulus of the armchair and zigzag HNT while the radius and temperature are  $12 \text{ \AA}$  and  $300 \text{ k}$  respectively. As we can see in Figure 3. 22, Young's modulus can be obtained from the stress-strain response of both arrangements. It is obvious that Young's modulus of armchair arrangements was completely higher than that of zigzag arrangements. The zigzag arrangement showed a relatively Young's modulus is  $219.90 \text{ GPa}$ . The elastic modulus of the armchair structure is  $328.46 \text{ GPa}$ .

To study the effect of temperature on Elastic modulus, one ac and one zz arrangement of HNT with a  $12 \text{ \AA}$  radius was chosen. Their Elastic modulus was calculated with an increase in temperature from  $300 \text{ K}$  to  $700 \text{ K}$ , under tensile loading with a similar strain rate equal to  $1 \times 10^9 \text{ s}^{-1}$ , the results are provided in Figure 3. 23.

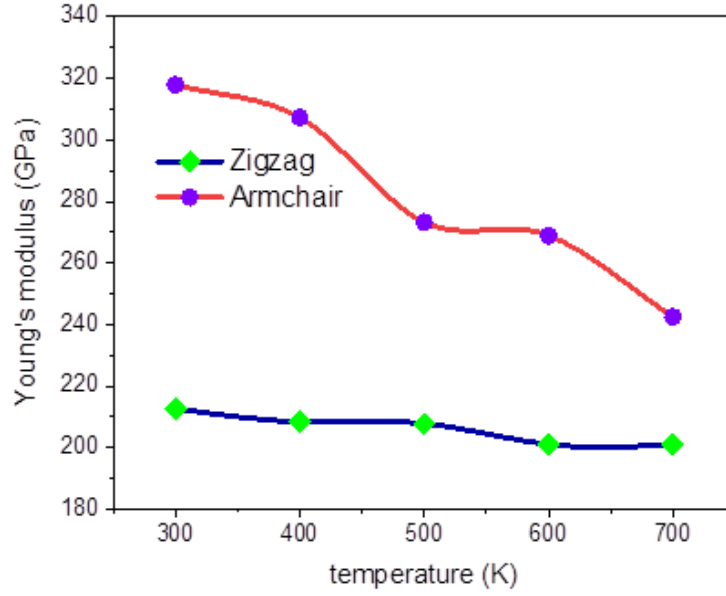


**Figure 3. 23:** Effect of temperature on Young's modulus of HNT armchair and zigzag under uniaxial tensile

We can observe a decline in Elastic modulus for both models. There is an obvious decrease in Elastic modulus for ac respect to zz. By increasing temperature to 700 k, Elastic modulus decrement is around about 5% and 21% for zz and ac respectively.

At this step, we calculated the Elastic modulus of the ac and zz structure of model 2 while the radius slightly increased from 12 Å to 25 Å and all models have 132 Å length. During the calculation, the boundary condition was removed then energy minimization was conducted. Then models were deformed along the tube axis (c crystal axis) at 300k temperature under three different strain rates ( $10^{10}$ ,  $10^9$  and  $10^8$  S<sup>-1</sup>). LAMMPS is used for all the MD simulations[36]. The results are provided in Figure 3. 24.

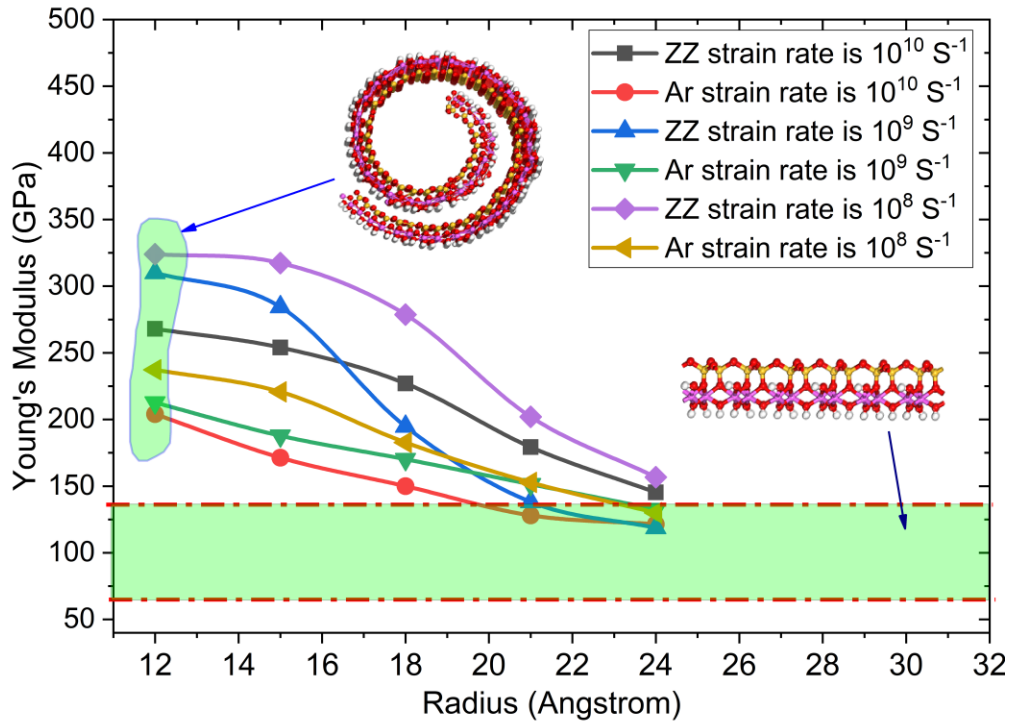


**Figure 3. 24:** variation Young's modulus respect evaluated radius for armchair and zigzag configurations of HNTs. The Elastic modulus of the flat sheet of HNTs is represented within dashed lines(different calculation) [55], [56]

As observed in Figure 3. 24, the Elastic modulus of armchair configurations was higher than the zigzag structure. ZZ recorded a slight reduction in Elastic modulus around 55 GPa in the radius 24 Å. In opposite, armchair reduction in Elastic modulus decreased from 320 GPa for structure with a 12 Å radius to about 133 GPa for structure with a 24 Å radius. A similar result was reported by Lecouvet et al [55]. Also, our result has good agreement with Guimaraes et al. (2010) calculations [10]. They determined Young's modulus of single-walled zz and ca Halloysite nanotubes by the DFT calculation. They found that the Elastic modulus of zigzag was in the range of 230–300 GPa for 15–36 Å diameters and 300–340 GPa for armchair structure for 21–46 Å diameters [10] as Figure 3. 24, we can observe an obvious reduction of Young's modulus for the larger radius (>20

Å), that explained with increasing radius, the elastic modulus of Halloysite Nano scroll is approaching the Halloysite flat sheet.

### **3.5 Conclusion**

In this chapter, we studied molecular mechanic simulations to illustrate the transformation of a slab surface aluminosilicate to a single Halloysite nano scroll. It was observed that the initial size of flat surface aluminosilicate plays a crucial role to generate a Halloysite nano scroll. We also have chosen the molecular dynamics simulation to determine the Elastic modulus of Halloysite nanotube with zigzag and armchair arrangements. The elastic modulus of both arrangements is decreased with an increase in radius. Although the Elastic modulus of the armchair arrangement was higher than the zigzag arrangement, the zigzag has more stable with an increasing radius. The elastic modulus of Halloysite nano scroll is approaching the Halloysite slab configuration which was calculated by DFT and MM methods. As well, we showed that increasing temperature made a significant decrease in elastic modulus in both arrangements. The results of this research propose a great help for understanding Halloysite which can be used for designing nanocomposites.

## Polyurethane

Polyurethane is a polymer composed of organic units joined by urethane units. While most polyurethanes are thermosetting polymers that do not melt when heated, thermoplastic polyurethanes are also available [3]. These polymeric structures are used in the manufacture of various industrial materials such as high-resilience foam seating, rigid foam insulation panels, spray foam, durable elastomeric wheels and tires and etc [80], [81]. Structurally, polyurethanes are in the class of compounds called reaction polymers, which include epoxies, unsaturated polyesters, and phenolics. The mechanical properties of polyurethane base structures are dependent on temperature and on the time scale of any deformation. At low temperatures, a polymer may be glasslike and it will break or yield at strains greater than a few percent. At high temperatures, it may be rubber-like, with a modulus and it may withstand large extensions of order 100% or more with no permanent deformation. In an intermediate temperature range, called the glass-transition range, the polymer is neither glassy nor rubber-like; it has an intermediate modulus and has viscoelastic properties. This means that, under constant load, it undergoes creep, i.e., the shape gradually changes with time, whereas at constant strain it undergoes stress relaxation, i.e., the stress required to maintain the strain at a constant value gradually falls [82]. Moreover, than temperature parameter, other parameters such as nanoparticles can be changing the polyurethane-based structures mechanical properties.

Traditional composite material has been reinforced with micro-scale fillers such as carbon fibres [3], [83]. However, as technologies continue to place rigorous demands on the materials, conventional polymer composites cannot satisfy these requirements. Therefore, the demand to design new composites reinforced at the nanoscale has increased. Nanoscale materials offer new insights into the physical properties of materials and the unique performance of nanocomposite compared to micro-scale fillers [82], [84].

Polyurethane has an inherent large strain capacity [82], and when reinforced with nanomaterials, it becomes promising as a nanocomposite for defence application [80], [81]. Therefore, when employing different materials in a composite, it is essential to have knowledge of the properties of individual components in order to estimate the properties of the entire system. This chapter provides a review of polyurethane (PU) (polymer matrix) in this project.

#### **4.1 Mechanical Properties of the PU**

To understanding of the mechanical properties of polyurethane, we develop an amorphous model of polyurethane, then we deform an amorphous model of PU using the static method. Figure 4. 1 shows the composition of a monomer polyurethane chain employs in this research.

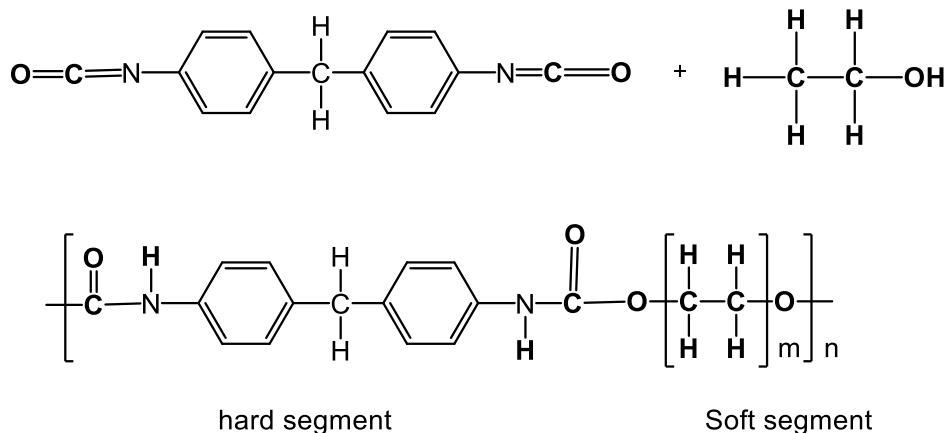


**Figure 4. 1:** Schematic of the basic reaction scheme of urethane formation [85]

A PU polymer model was prepared using the polymer builder in MS Modeling [86]. We consider linear PU with a molecular structure consists of butanediol and hexamethylene diisocyanate. The molecular structure of the monomer is  $([\text{C}_{17}\text{H}_{32}\text{N}_2\text{O}_4]_n)$ , where  $n$  is the repeat units of the monomer [85]. The “ $n$ ” could be amounts 5, 10, 15 or 20 and  $m$  is 1. The amorphous PU model was developing base on random distribution PU chain. The amorphous supercell model was formed from 20 random repeat chains and a single hexamethylene ( $n=20$  and  $m=1$ ). The supercell has  $a = b = c = 46.3 \text{ \AA}$  dimensions and the total atom is 8020 (as shown in Figure 4. 2).

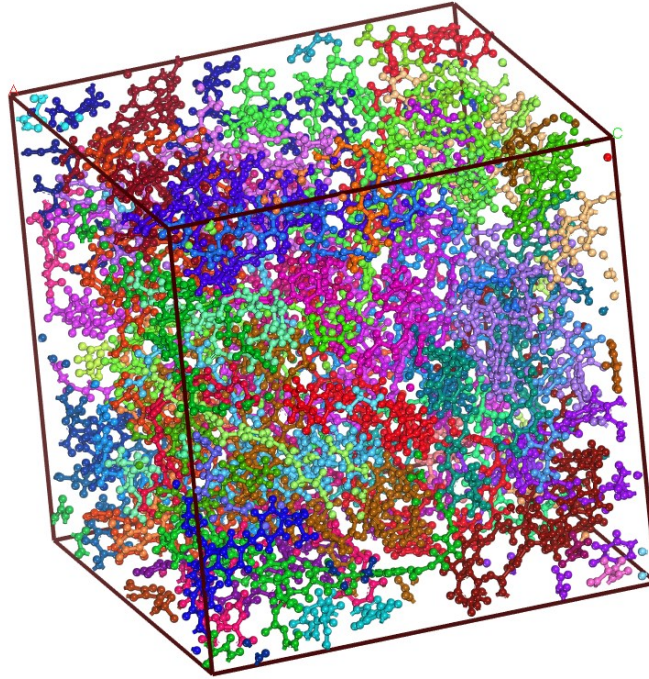


**Figure 4. 2:** Snapshot of an amorphous model of polyurethane with lattice parameters with dimensions  $a = b = c = 46.3 \text{ \AA}$ , repeat units ( $n=20$ ), No of chain = 15, No of atoms=8020

In order to obtain the mechanical properties, two ways could be employed. For this section, we are applying small strains upon the amorphous periodic structure (see the static approach in section 2.4.1).

The Dreiding, PCFF and COMPASS potential energy functions are used [28]–[33] to calculate mechanical properties. The Long-range electrostatic interactions were treated using the particle-particle-particle-mesh (PPPM) [87] summation method. All simulations were set up under 0.01 maximum strain amplitude.

The dimensions of the supercell were uniformly expanded in the three directions to create a deformation loading. Then, the new coordinates of the atoms within the new dimensions were calculated. Then, the stress in the minimized structure was computed.

This was repeated for a series of compressive and tension strains on supercell then strain energy as a function of applied strain was computed. Finally, the stiffness matrix has been calculated which is a basic feature of the isotropic strain energy. Table 4. 5 shows the elastic constants of amorphous polyurethane calculated by the molecular mechanic approach. The mechanical behavior of polyurethane assumed is isotropic at zero temperature. This procedure is based on reference [2].

*Table 4. 5: Elastic constants of amorphous polyurethane calculated by the molecular mechanic approach*

	atoms	C11 (GPa)	C22 (GPa)	C33 (GPa)	C12 (GPa)	C13 (GPa)	C23 (GPa)	Bulk Modulus (GPa)	Young modulus (GPa)	Poisson's ratio $\nu$
PUR-I (MD Dredging FF) [2]	8040	7.83	7.95	7.64	2.95	2.59	2.76	4.57	6.22	0.27
PU <sup>2</sup> (MD Dredging FF)	8040	5.3761	5.0770	4.8635	3.4144	3.3302	3.3988	3.715	2.86	0.3717
PU <sup>3</sup> (MD Compass FF)	8040	7.0733	6.7630	6.9855	5.8356	5.4753	5.3843	6.21	1.596	0.45
PU <sup>4</sup> (MD PCFF-IFF)	8040	6.2868	7.6208	3.8240	4.6641	4.4752	3.1242	1.6430	0.811	0.392

The elastic moduli and Poisson's ratio for the PU models were calculated, which are essential in characterizing the mechanical properties of a system. Young's modulus of 1.596 – 2.86 GPa was calculated for the amorphous model of PU. Table 4. 6 compared Elastic constants of the amorphous cell of current works with previous experimental

<sup>2</sup> density 1.0 and 8040 atoms and force field is Dredging

<sup>3</sup> density is 1.0 and 8040 atoms and force field is COMPASS

<sup>4</sup> density is 1.0 and 8040 atoms and force field is PCFF-IFF

results. We expect that this work will add to the understanding of the next step of generation of our nanocomposites which are augmented with Halloysite nanotube.

*Table 4. 6: Elastic constants of amorphous polyurethane calculated by molecular dynamics*

Model	atoms	density (g/cm <sup>3</sup> )	Bulk Modulus GPa	Young Modulus GPa	Shear Modulus GPa	Poisson's ratio
Martienssen et al Experimentally [88]		1.00-1.20	-	0.015-0.7	0.006-0.23	-
Bicerano et al Experimentally [89]		-	3.93	1.69	0.592	0.43
PU2 (MD Deriding FF)	8040	1.0	6.21	1.596	0.5477	0.45
PU3 (MD COMPASS FF)	8040	1.0	3.715	2.86	1.0426	0.372
PU4 (MD PCFF-FF)	8040	1.0	1.6430	0.811	0.2915	0.392

This discrepancy between Young modules is due to computing the ideal nature of the simulated systems, while the experimental samples, which may contain impurities or defects during formation which expect simulations model have higher results compared to experiments. Finally, the different temperatures between simulated models (0 K) and room temperature (300 K) may also affect the result.

## 4.2 Nanocomposite

In order to improve the efficiency and functionality of PU, it is necessary to study to combine it within composites. Nanomaterials and nano-composites have been extensively studied in different disciplines, such as physics, chemistry and material science. Halloysite nanotubes are commonly studied nanomaterial;

Wei Ling Tham et al. fabricated nanocomposites of Polylactic acid reinforced with Halloysite nanotubes (PLA/HNTs). They used Ethylenebis (Stearamide) (EBS) and

Epoxidized Natural Rubber (ENR) in order to improve the dispersion of HNT in PLA. A thermogravimetric analyzer (TG) was used to measure the thermal properties of the PLA/HNTs under different loading. Their results revealed that the thermal stability of PLA/HNTs was increased by the adding of EBS. They conducted an impact test to identify the mechanical properties of the PLA/HNT nanocomposites and they found that the optimal percent of EBS was 5 mass%. While adding 15 wt% ENR increased the tensile modulus and impact strength of the PLA/HNTs to approximately 340 percent in the PLA/HNT nanocomposite compared with pure PLA [90].

Vishwa Pratap Singhl et al. investigated the distribution of Halloysite nanotube (HNT) on the nanocomposites of Polyethylene. They evaluated the effects of adding various percentages of HNT (ranging from 1 to 10 wt %) and its distribution on the morphology and properties of nanocomposites. A fine distribution of HNTs in the matrix was found to enhance the mechanical properties of the Polyethylene nanocomposites, where the addition of Halloysite nanotubes significantly enhanced their modulus and strength. The modulus and strength increased by 17% and 12% respectively for the addition of 5 wt% HNT [91].

Nan-Ying Ning et al. fabricated a polypropylene (PP) composite reinforced with Halloysite nanotubes (HNTs). A scanning electron microscopy was used to consider the distribution of Halloysite nanotubes (HNTs) on polypropylene. The crystallization behavior and the mechanical properties were also investigated for both the PP/HNT composites and the pure PP. The impact test indicated that a good dispersion of HNTs in

the PP matrix improved significantly with a greater degree of crystallization, although the tensile and impact strength of the PP/HNT with 10 wt% of HNTs did not much improve [92].

Ismail et al. employed both mechanical and solution mixing methods to prepare Halloysite for the fabrication of a natural rubber (NR) nanocomposite. They found that nanocomposites prepared with the solution mixing method had higher tensile strength and tensile modulus, and lower fatigue life compared to the mechanical mixing method fabrication [93].

Halloysite can improve the strength and modulus of polymethyl methacrylate (PMMA) and epoxy without losing the thermal properties. The addition of 3–5 wt% of Halloysite to PMMA and epoxy resin significantly increases its strength; However, elongation of that material could be decreased [70]. The stress-strain rates of various Halloysite percentages added to PMMA and polymers epoxy resin are presented in Figure 4. 3 and Figure 4. 4, where the optimal level of Halloysite into both polymers is determined to be 3–5 wt%.

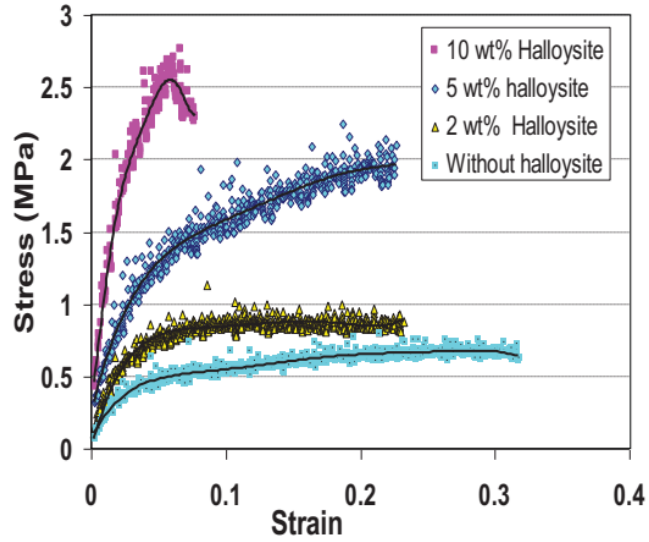


**Figure 4. 3:** Stress-strain PMMA with various Halloysite percentages [70]

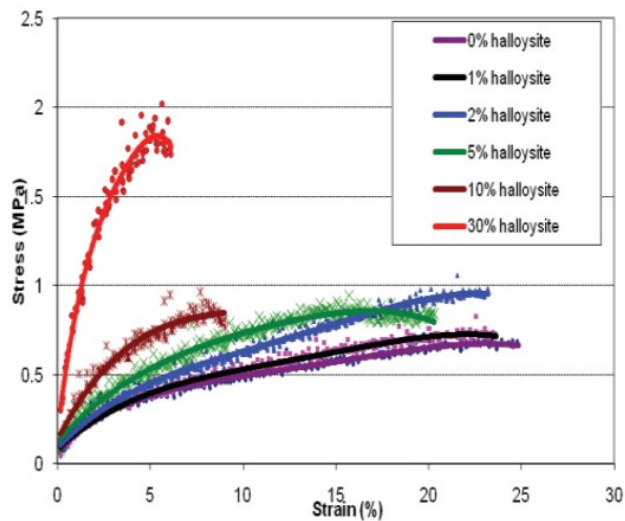


**Figure 4. 4:** Stress-strain of polymers epoxy resin with various Halloysite [70]

In terms of reinforcing PU, Wei Chen and colleagues fabricated a PU composite reinforced with 9.3 wt% Multi-Walled Carbon Nanotube (MWNT) fibres. They measured Young's modulus and elongation of the PU with MWNTs and then compared it to the same PU without MWNTs. The results designated that Young's modulus was significantly

increased with the fine distribution of MWNTs into the PU matrix, while elongation and fracture properties were reduced [94].

The work aims to provide a conceptual framework for the development of PU/ HNT nanocomposite for use in ballistic applications (high strain rate performance) in both civilian and defense applications. Understanding the structure, properties and dynamic response of these materials at the atomistic scale can estimate mechanical properties and help design new material for the ballistic application. The next chapter will describe a computation technic that would be useful to design better materials.

## Modified Force Field

Accurate simulation of non-bond interaction is more challenging in a classical forcefield. In this chapter, we are going to make a bridge between DFT and MM. For this purpose, first, we compute the energy of PBC optimization HNT-PU with density functional theory (DFT), second Machine learning (ML) method through the particle swarm optimization (PSO) algorithm has been applied to fitting force field parameters of Molecular Mechanic (MM) by using data from DFT calculations for different configurations. The best Lennard Jones parameters were obtained through the DFT interaction energy and original PCFF-IFF force field.

### 5.1 Motivation

In order to employ HNT in different applications, it is necessary to consider HNT into different loading conditions. HNT has extraordinary properties, in specific, stiffness and strength which make it attractive as the reinforcing component in a composite material. The reason for applies an HNT as the reinforced particle is the high density of cross-link between matrix and HNT that unites the polymer chains. The characteristics of the combination composite material depend on the properties of the fibers and matrix and the nature of the interface. Determining the influence of the interactions interface on the properties of materials is becoming more essential for reliable predictions of material behavior, especially, in extreme conditions to design appropriate materials for a particular purpose.

In this chapter, we are going to introduce a method to develop the classical potential to calculate interaction energy between HNT and PU. This potential energy will be used for classical molecular dynamics and molecular mechanics simulations. Furthermore, molecular modelling and the availability of computational methods provide an approach for understanding the fundamental behavior of new materials in materials science or interdisciplinary science.

The incorporation of HNTs can possibly improve the ability of PU to absorb energy during high strain rate conditions, due to HNTs ability to chemical interact with the PU and fine dispersion around the polymeric structure. The study of this interaction can possibly indirectly provide a better understanding of the energy absorption mechanism at the atomic level of the polyurethane under high strain conditions. The main purposes of this chapter are to compute HNT/PU interaction with DFT then develop an interaction potential that will be used for classical molecular dynamics and molecular mechanics simulations which is too expensive to consider with DFT.

The purpose of machine learning (ML) is to solve efficiency and accuracy interatomic interaction in a large system by using higher accurate DFT calculations [95], [96]. Lately, a variety of complex machine learning (ML) algorithms for small and large systems have been introduced for using the total energy data of DFT calculations [97]. Those results are applied in ML fitting to improve the potential coefficient from an accurate data. Usually, those ML models have developed for small atomic configurations, which is inefficiency in using precision DFT techniques [98].

In this chapter, we introduce an alternative technique to develop force fields in MM with the precision results of DFT calculations. Overall, accurate modeling of the interaction interface is more challenging to define in the classical force field [12], [13]. The purpose of this research is to implement a proper ML to study the interaction energy between HNT and PU chains and improve the PCFF-IFF force field. Subsequently, after calculating the mechanical properties of amorphous PU and the optimized structure of Halloysite nanotubes, we can calculate the interaction energy between HNT and PU. In this stage, we compute interaction energy between HNT and PU. For this purpose, we were employed the density function approach to calculating the non-bonding energy between HNT and PU.

## **5.2 Methodology of Fitting Process**

In order to employ HNT in different applications, it is necessary to consider materials exposed to different loading conditions. In this section, we applied computational techniques for fitting the interaction energy between HNT and PU obtained from DFT and MM calculations at the atomistic level. Here are steps for this computation method:

- 1- A slab surface is created according to the optimum unit cell of HNT and extended in the z-direction to embed a monomer PU.
- 2- For DFT calculations, the cut-off energy and minimal k-point mesh are determined through convergence studies to be 580 eV and 10 (auto mesh) respectively. These parameters are used for all trajectory calculations to minimize computational cost.

- 3- We calculate the potential energy by rotational PU monomer respect to the flat surface of HNT, after obtaining of total energy as a function of rotational movement, we are also able to recognize the lowest energy of the monomer state.
- 4- We calculate the potential energy by laterally relocating PU monomer respect to the flat surface of HNT, after obtaining of total energy as a function of lateral displacements, we are also able to recognize the lowest saddle points of the potential energy.
- 5- We repeat the computational method this time vertical relocating of PU. Consequently, we are able to calculate the interaction energy for different vertical movements.
- 6- We repeat step 5, this time with PCFF-IFF. Then, the interaction energy is calculated for the different vertical positions of the PU.
- 7- In our approach, the particle swarm optimization (PSO) was applied to find the best fit between DFT and the non-bonded Lennard-Jones (LJ) parameters used in PCFF-IFF.

### **5.2.1 Preparation of Supercell**

In chapter 3, we used DFT calculations to obtain optimum lattice parameters. The result was provided in table 3.1. Then a supercell was generated from replicated 3\*3\*1 the optimized unit cell and extended in the z-direction to form a vacuum space to embed a PU

chain (*Figure 5. 1*). The distance between PU and HNT was calculated based on the center of mass of the HNT slab and the polymer chain.

### 5.2.2 DFT Calculation

Density functional theory (DFT) calculates the density of electrons instead of the complete analysis of wave function. The benefit of DFT is the capability to model chemical transformations, particularly bond breaking or bond forming. Various atomic arrangements are available for Halloysite nanotubes, such as cylindrical shape, flat surface and helicity rollup. The proper arrangement allowing the effective study by reducing assumptions and constitutive requirements.

One major advantage of DFT simulation is the capacity to model interactions with a discrete approach, due to the occupation of molecular species, noncovalent interactions such as hydrogen bonding and van der Waals forces which play a critical function in the balance of the two or three body structures. Accurate predication of vdW interactions is possible by high-level wave functions or the DFT method.

Alternatively, the gradient-corrected functionals PBE [21] of DFT approaches provides a great agreement between the computational costs and high-level results of conventional DFT calculations. In this section, we provide the defined configuration structures to calculate total energy with the DFT technique.

The DFT approach was applied to compute total energy calculations for interaction energy between HNT/PU. For this purpose, we simulated the PU monomer ( $C_{17}N_3O_3H_{18}$ )

interacting with HNT. As shown in *Figure 5. 1*, a supercell was generated from 3\*3\*1 the optimized unit cell of HNT, and extended cell in the z-direction to form a vacuum surface of HNT to embed a PU chain. There are 350 atoms in the supercells.

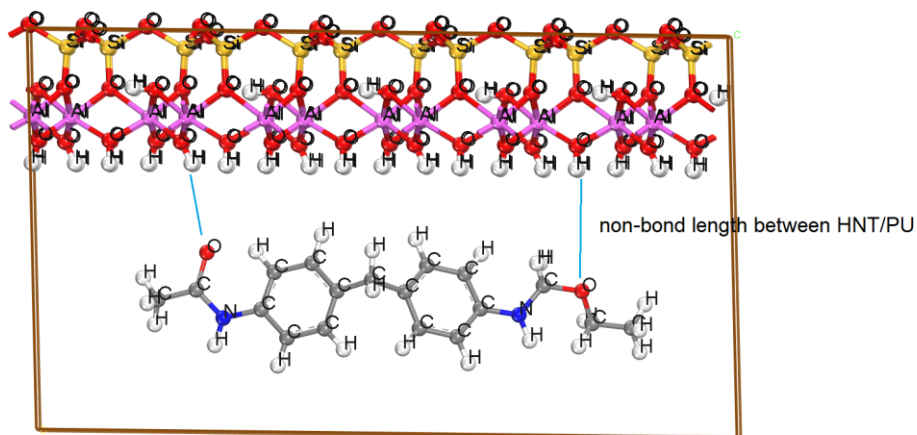


**Figure 5. 1:** interact between HNT with simple PU chain in a periodic periodic cell with 15.6 Å \*25 Å \*27.2 Å

After the generated model, we employed the density function approach to calculate the non-bonding energy between HNT and PU. We calculate the total energy of the above structure associate with changing cutoff energy and the k-point mesh size to achieve to efficiently and accurately calculations. Hence, an initial automatic k-point mesh starts with 8 weight and cutoff energy (maximum energy of pseudopotential which is oxygen atom) is assigned then potential energy versus these changes was calculated. The cutoff is increased by 10% and auto mesh increases one unit. The method is repeated until the potential energy versus these changes was steady as displayed in Figure 5. 2.

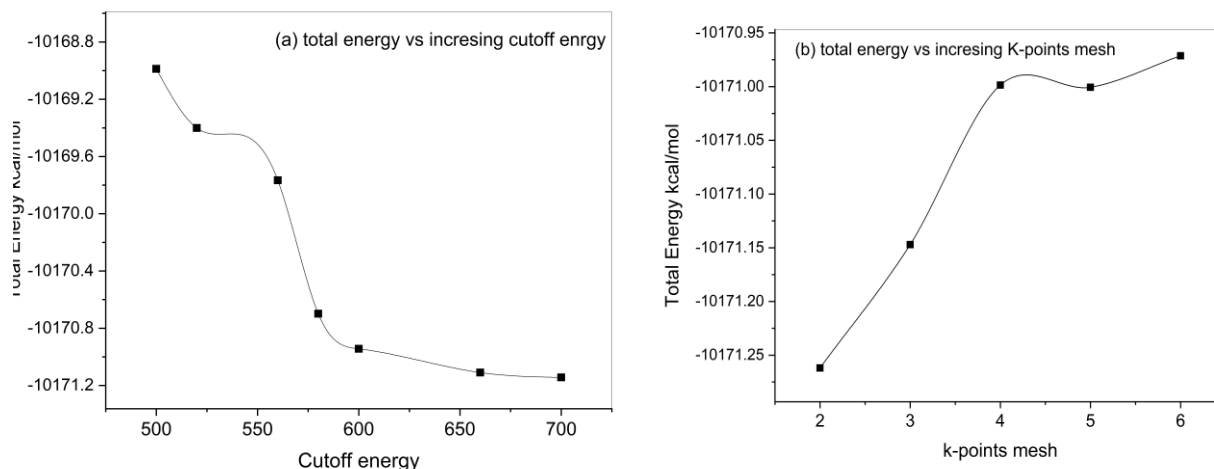


**Figure 5. 2:** Total energy convergence of HNT structure with (a) increasing cutoff energy, (b) with increasing k-points.

Density Functional was carried out with “Vienna Ab-initio Simulation Package (VASP)” [49] with the PBE gradient-corrected functionals [21] methods to calculate the total energy of the mentioned system. The projector augmented wave (PAW) pseudopotential [26] was applied for describing the core electrons interactions. The calculation was performed at zero temperature. As Figure 5. 2, we select k-points grid meshes with auto mesh with weigh 10 and 580 eV for cut-off energy for next DFT calculations.

In contrast to the rigid molecule state, PU-HNT incorporates flexible degrees of freedom such as different types of rotational and sliding and opening positions PU versus HNT. We proceed with the DFT method by dividing them into two stages. The first stage is to obtain fixing phases of PU by calculating the total energy of all states of rotational and sliding of PU positions. At this step, total energy was obtained by the DFT approach, the second stage is to obtain the interaction energy for the opening movement.

### 5.2.3 Rotational Movement

The advantage of fixing the phases is that we can significantly decrease the number of parameters, thereby saving the computational cost. Therefore, step one gives us an opportunity to make a comparison among different positions. We calculated the total energy for different angles (0-360 degrees) of rotational PU axes respect to the flat surface of HNT as shown in Figure 5. 3.

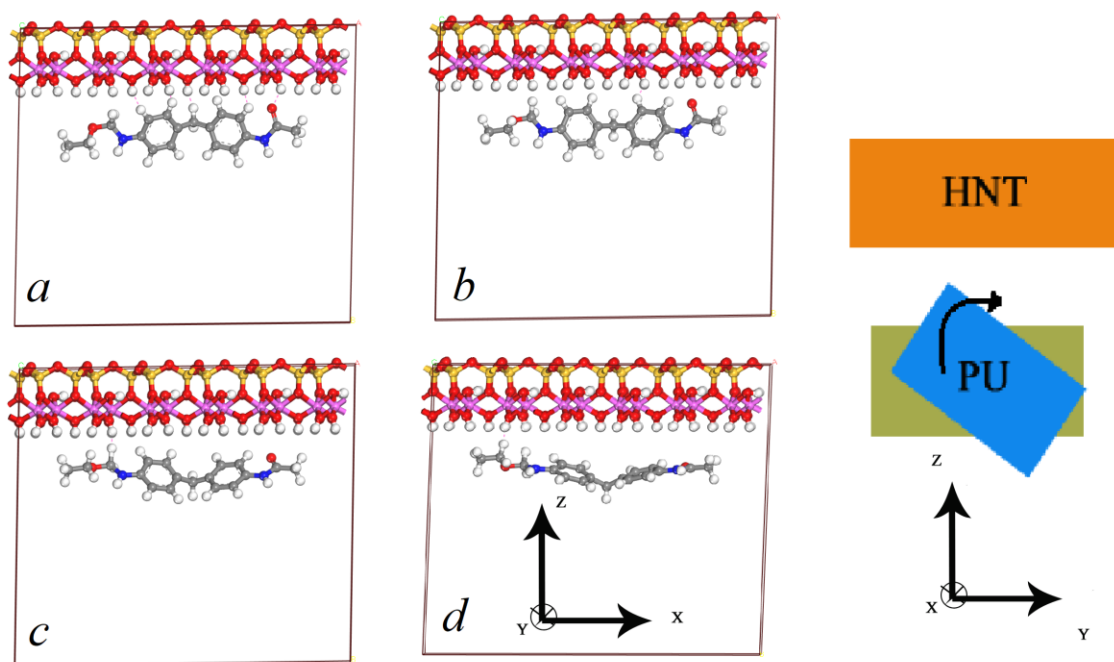


**Figure 5. 3:** PU axes position respect to the flat surface of HNT, a) 0-degree, b) 30-degree, c) 60 degree and d) 90 degrees

Figure 5. 4 illustrated scans of the total energy for the different angles of PU respect to the flat surface of HNT. Thereby, the fixing phase is in 60 degrees.

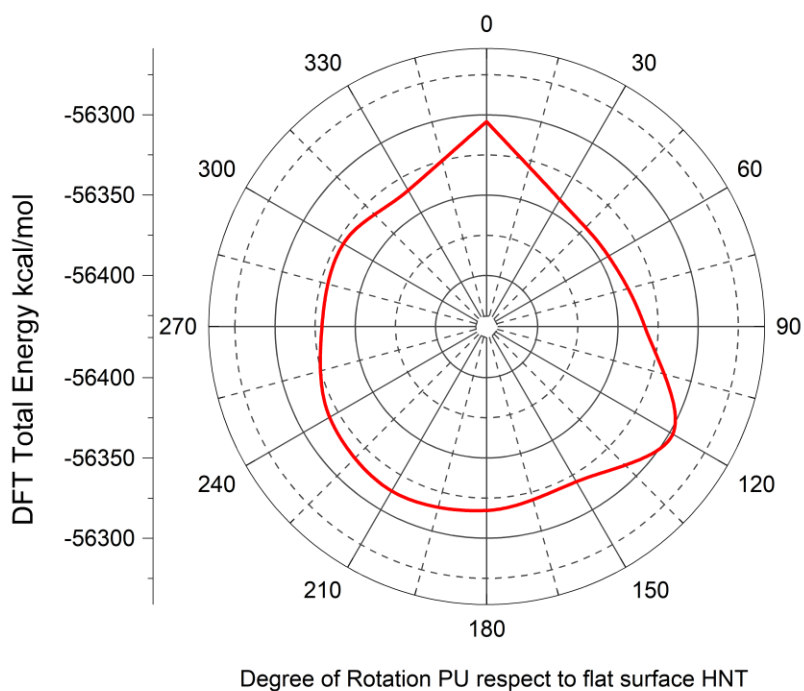


*Figure 5. 4: scans of the total energy for the different angles of PU respect to the flat surface of HNT*

#### 5.2.4 Sliding Movement

Similar to rotational movement, we evaluate a sliding movement by utilizing 60-degree arrangement of PU. We calculated total energy for different sliding of the position of the center mass of PU monomer respect to the center mass of the flat surface of HNT as shown in Figure 5. 5.

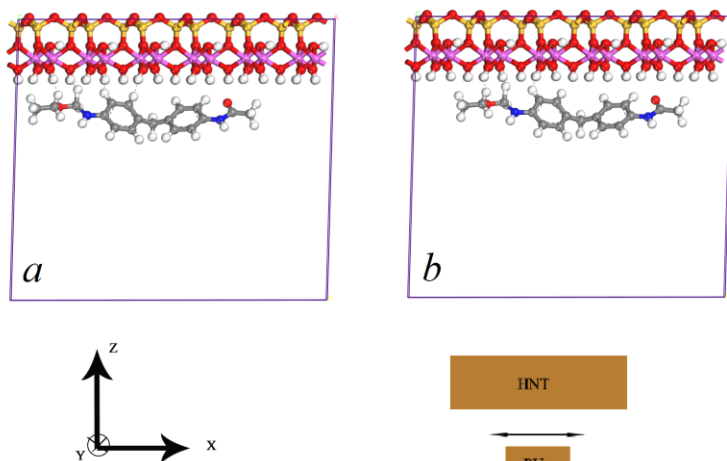


**Figure 5. 5:** sliding of the position of the center point of PU monomer respect to the center point of the flat surface of HNT

Figure 5. 6 illustrated scans of the total energy for the sliding of the position of the center mass of PU monomer with respect to the center mass of the flat surface of HNT. Thereby, the saddle point represented to minimum energy. We use this point to start the vertical trajectory.

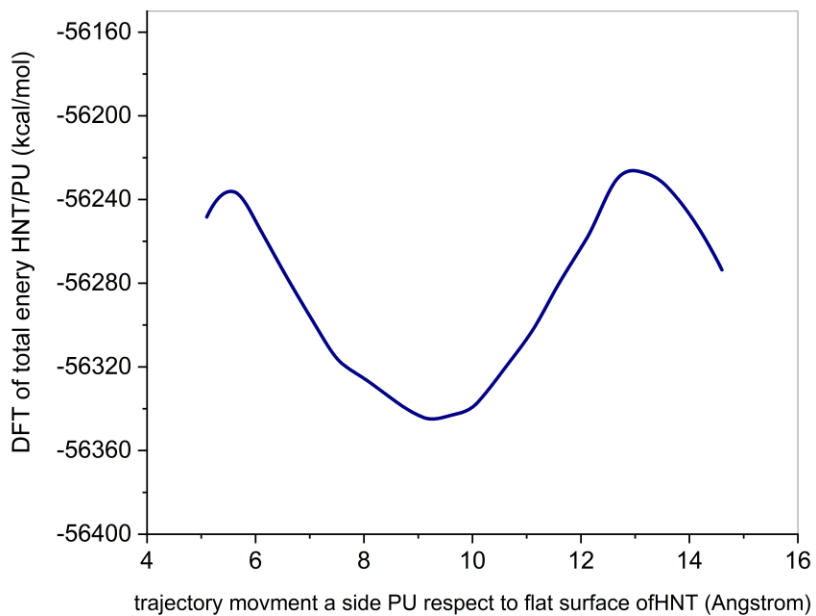


**Figure 5. 6:** scans of the total energy for the different lateral movements of PU respect to the flat surface of HNT

### 5.2.5 Opening Movement

In order to compute the interaction between HNT/PU, a supercell structure for both the HNT and a chain of PU was created according to the minimum state of PU state in the two earlier steps (rotational and sliding). As introduced at 5.3.1, the supercell is formed of  $3*3*1$  the optimized unit cell of HNT, then extended in the z-direction to form a vacuum space for embedded PU chain. Then PU moves vertically with equal increments (0.35 Angstrom) as illustrated in Figure 5. 7. The distance was calculated based on the center mass of slab HNT and polymer chain.

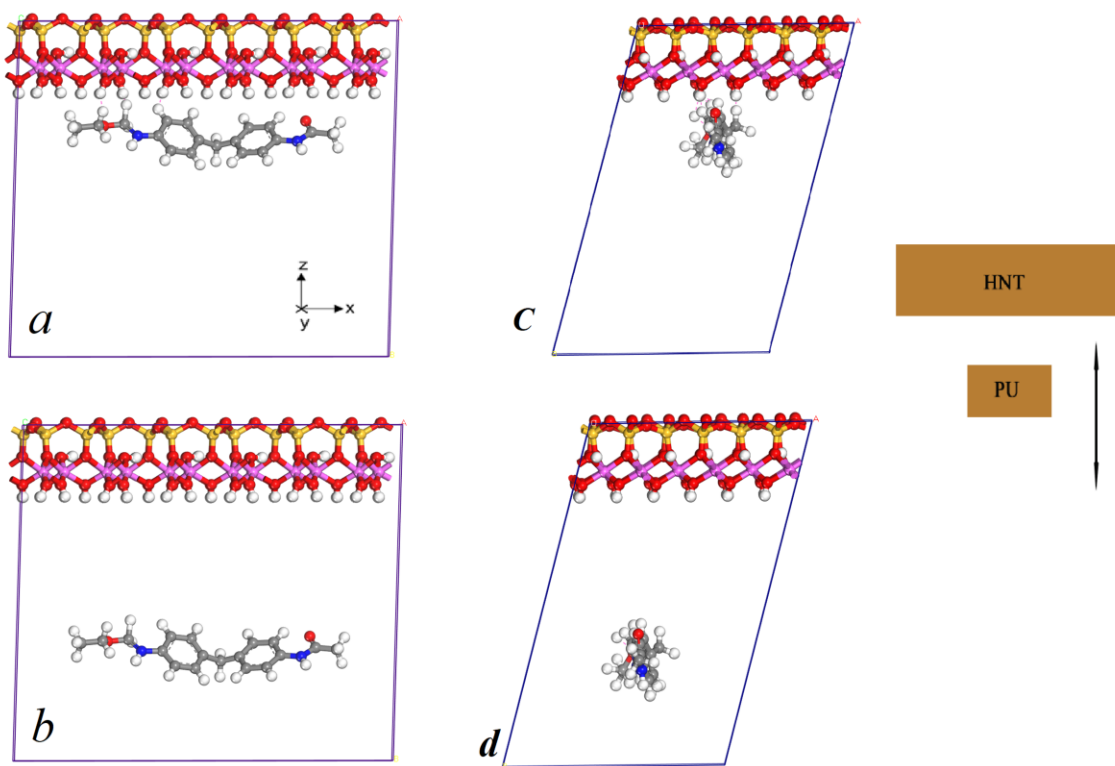


**Figure 5. 7:** trajectory, which is formed of the smaller vacuum gap (a, c nearest two-body) to the largest distance rearrangement (b, d far way PU monomer) periodic cell with  $15.6 \text{ \AA} * 25 \text{ \AA} * 27.2 \text{ \AA}$



interactions. The calculation was performed at zero temperature. Reciprocal space was represented k-points grid meshes by an auto mesh with weighing 10. There are 350 atoms in the supercells and the cut-off energy was 580 eV. The ions were relaxed with a conjugate gradient algorithm until the energy components on any ions were smaller than 0.01 eV. The result is depicted in Figure 5. 9.

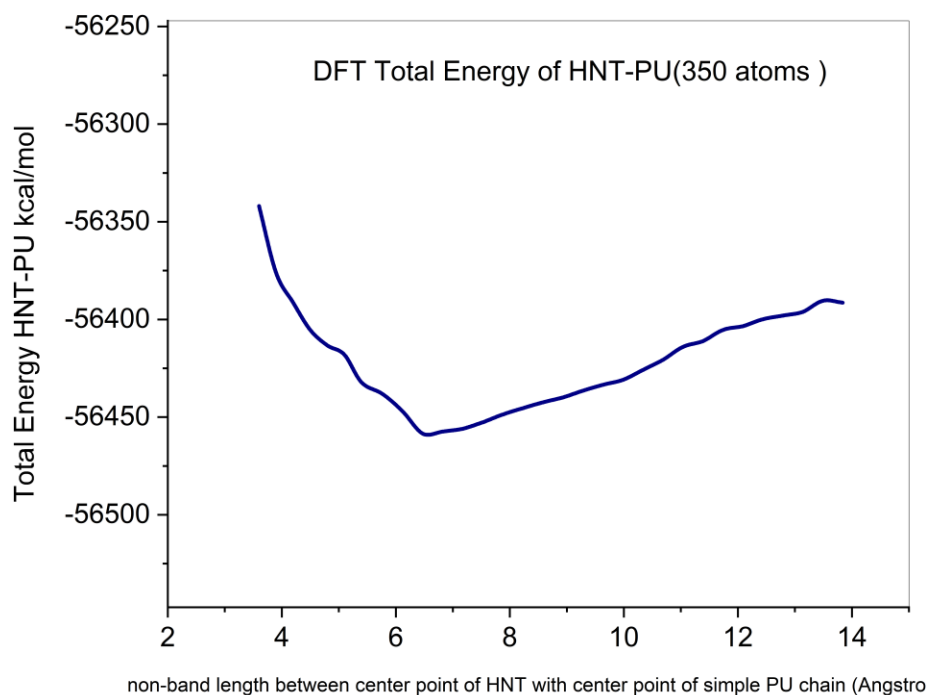


**Figure 5. 9:** total Energy vs non-band length between HNT with simple PU chain

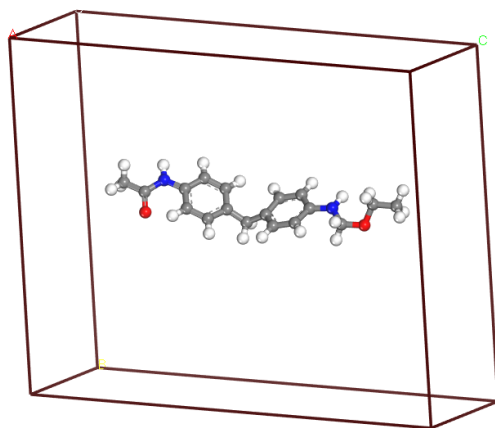
### 5.2.6 Interaction Energy

The interaction energy between the PU and the HNT was computed by the following equation;

$$E_{interact}^{DFT} = E_{tot-DFT} - (E_{PU} + E_{HNT})$$

Where  $E_{\text{tot-DFT}}$  refers to the total energy of the structure (HNT and PU),  $E_{\text{HNT}}$  indicates the energy of the isolated slab HNT,  $E_{\text{PU}}$  refers to the energy of the isolated polyurethane and  $E_{\text{inter}}^{\text{DFT}}$  indicates interaction energy between HNT and PU molecules.

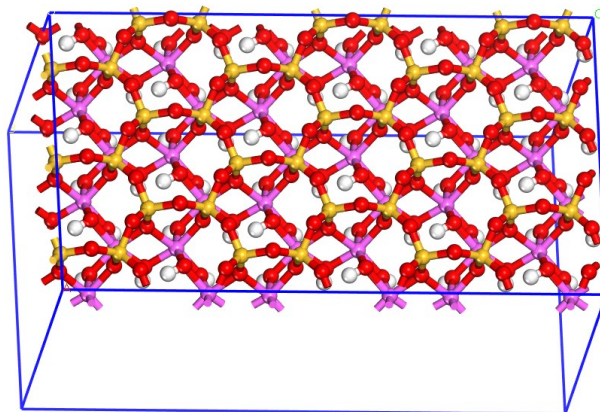
In order to calculate  $E_{\text{inter}}^{\text{DFT}}$ , we simulated isolated the optimized polyurethane chain ( $\text{C}_{17}\text{N}_3\text{O}_3\text{H}_{18}$ ) in the same lattice parameter of supercell illustrated Figure 5. 10. Then, Density Functional was performed at zero temperature to calculate the energy of PU. Reciprocal space was represented k-points grid meshes by an auto mesh with weighing 10. There are 44 atoms in the supercells and the cut-off energy was 580 eV. Similarity, the ions were relaxed with a conjugate gradient algorithm [58] until the energy components on any ions were smaller than 0.01 eV.



**Figure 5. 10:** the optimized polyurethane chain PU ( $\text{C}_{17}\text{N}_3\text{O}_3\text{H}_{18}$ ) with dimension  $15.6 \text{ \AA} * 25 \text{ \AA} * 27.2 \text{ \AA}$

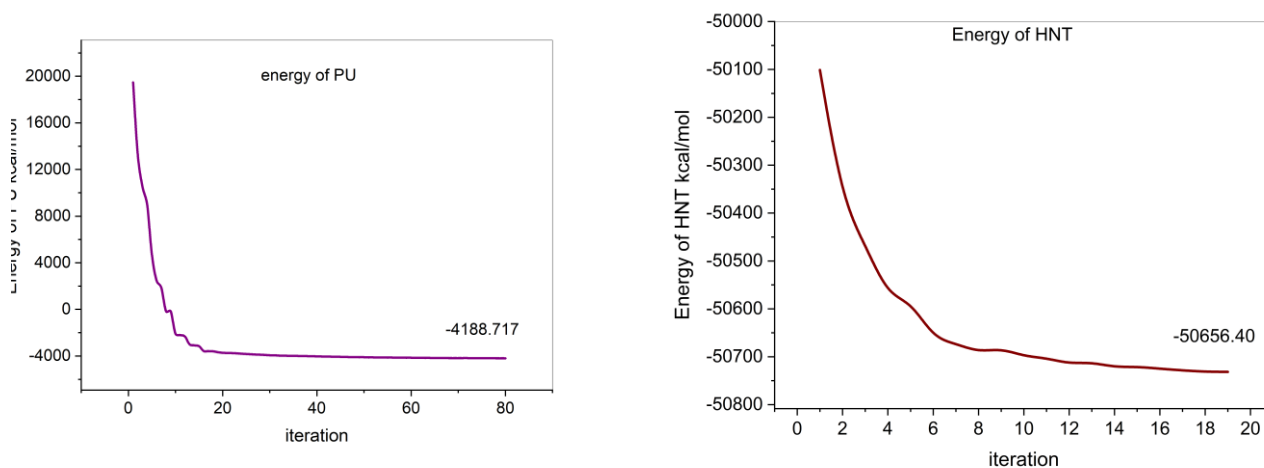
We repeat this process for simulated isolated a supercell HNT which was generated from of  $3*3*1$  the optimized unit cell of HNT and  $15.6*25*27.2$  cubic Angstrom length as illustrated Figure 5. 11. Then, DFT was performed at zero temperature to calculate the

energy of HNT. The k-points grid meshes are represented by an auto mesh with weighing 10. There are 306 atoms in the supercells and the cut-off energy was 580 eV.



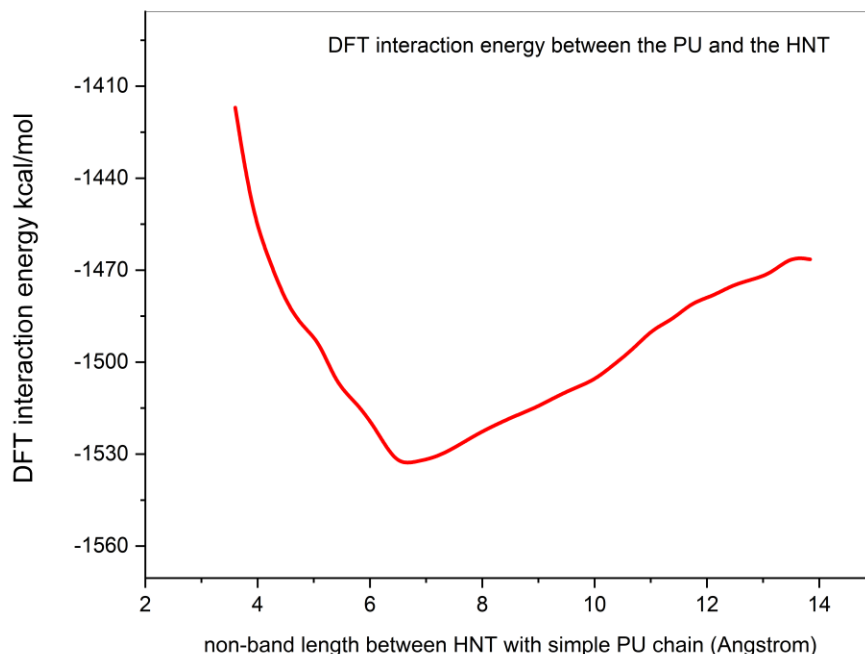
**Figure 5. 11:** the optimized HNT with dimension 15.6 \*25\*27.2 cubic Angstrom

Figure 5. 12 illustrates the minimum energy versus iteration steps for isolated PU and HNT structures. As a result of the equilibration process, the energy for a single polyurethane chain is  $E_{PU}=-4188.717$  kcal/mol and energy for the flat surface of Halloysite is  $E_{HNT}=-50656.40$  kcal/mol, as displayed in fig 5.12.



**Figure 5. 12:** total energy evolution during the equilibration of the individual PU and the HNT

Therefore, we substituted individual energy of PU and HNT in equation 5.1, subsequently, the interaction energy between the PU and the HNT was calculated and the result is shown in Figure 5. 13.



*Figure 5. 13: scans of the interaction energy for the sliding of the position of the center point of PU monomer respect to the center point of the flat surface of HNT for opening movement.*

After employed the ab-initio approach within density functional theory, the next step is calculating interaction energy though implement in the molecular mechanic by using PCFF-IFF force field. The force field is defined base on combination rules for local potential energy terms (bond, angle, and dihedral) and non-bond interaction terms.

### 5.3 Molecular Mechanics

Molecular Mechanics is basically a method that uses potentials that are functions of intramolecular bonds lengths, bond angles, and bond dihedral angles of the molecules for the bonded (covalent) interactions. Meanwhile, classical interatomic interactions are

calculated by summation over van der Waals and electrostatic interactions. These methods are widely employed in the connection of weak (non-covalent) interactions [99], [100].

The total energy between the PU and the HNT was calculated by the following equation (5.2)

$$E_{interact}^{MM} = E_{tot-MM} - (E_{PU} + E_{HNT})$$

5.2

Where  $E_{tot-MM}$  refers to the total energy of the structure (HNT and PU).  $E_{HNT}$  indicates HNT energy.  $E_{PU}$  refers to the polyurethane energy of the and  $E_{inter}^{MM}$  indicates interaction energy between HNT and PU molecules. In order to measure  $E_{inter}^{MM}$  and eliminate local interaction, we minimize the energy of an isolated, optimized polyurethane chain ( $C_{17}N_3O_3H_{18}$ ) in the same supercell as illustrated in Figure 5. 10. Then, conjugate gradient [58] minimization was performed at zero temperature to calculate the energy of PU. This process was continued until the subsequent difference energy steps are less than  $10^{-4}$  kcal/mol.

We repeat this process for to simulate an isolated, optimized HNT sheet as a supercell with of 3\*3\*1 copies of the optimized unit cell of HNT as illustrated in Figure 5. 11. Then, conjugate gradient [58] minimization was performed at zero temperature to calculate the energy of HNT. This process was continued until the subsequent difference energy steps are less than  $10^{-4}$  kcal/mol. Figure 5. 14 illustrated conjugate gradient minimization of isolated the polyurethane chain and the individual flat surface Halloysite.

After the equilibration process, energy for a single polyurethane chain is  $E_{PU}=4699.8$  kcal/mol and energy for the flat surface of Halloysite is  $E_{HNT}=30471.5$  kcal/mol.

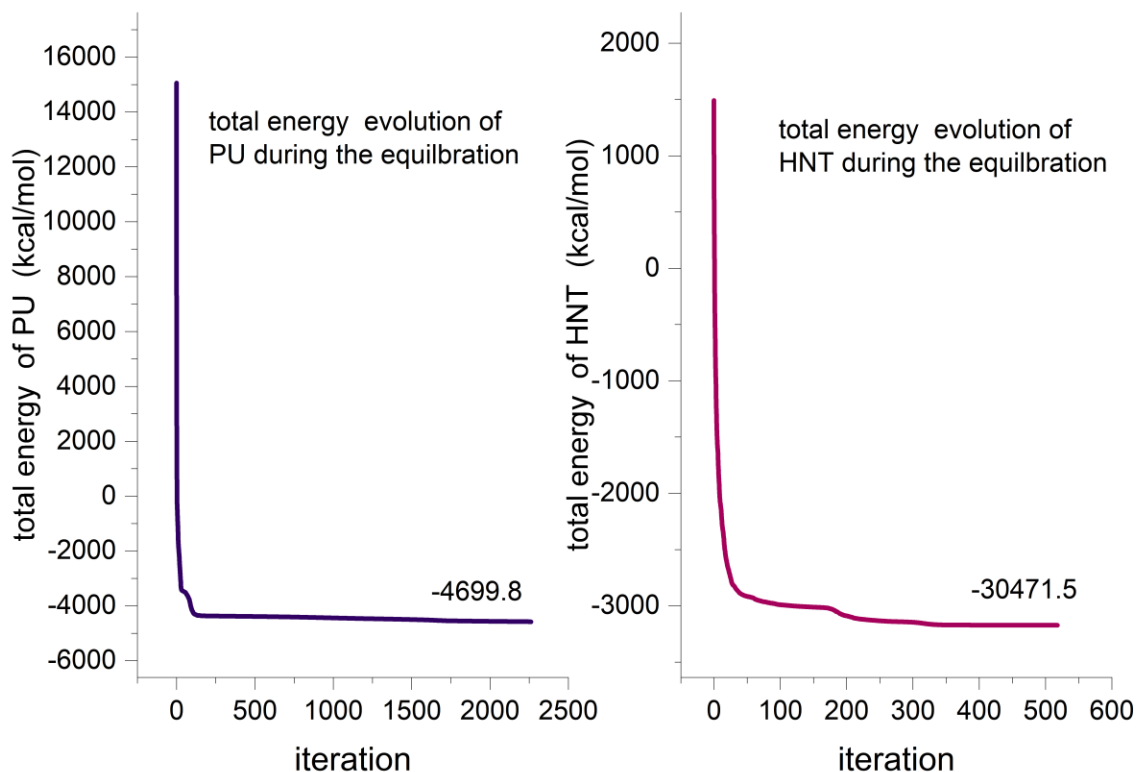


*Figure 5. 14: conjugate gradient minimization isolated the polyurethane chain and Halloysite flat surface*

In the classical molecular dynamic method, the non-bond energy between atoms pairs is calculated with the 9-6 Lennard-Jones potential (implemented 96 LJ format due to applying class2 for defining bond coefficients) and Coulomb part as described in equation 5.3;

$$E_{Interaction}^{MM} = \sum_{i,j \text{ nonbonded}} \varepsilon_{ij} \left[ 2 \left( \frac{\sigma_{ij}}{r_{ij}} \right)^9 - 3 \left( \frac{\sigma_{ij}}{r_{ij}} \right)^6 \right] + \sum_{i,j \text{ nonbonded}} \frac{q_i q_j}{4\pi\varepsilon_0 \varepsilon r_{ij}}$$

5.3

Where  $E_{Interact}^{MM}$  is the non-bonding potential energy,  $r_{ij}$  is the distance between a pair of atoms,  $\varepsilon$  identify the well depth of potential,  $\sigma$  refers to equilibrium length and  $q$  is the atomic charges.

The non-covalent bond breaking and configuration is more challenging to define in the classical force field potential [12], [13], due to the dynamic evolution of the potential energy surface.

The aim of this section is to utilize DFT to obtain the non-bonded interaction energy between the HNT and PU chain, and thereby improve the PCFF-IFF force field. This developed force field will be applied in classical MD and MM to simulation HNT/PU structure under external loading which is too expensive to evaluate with DFT.

In this section, as in the DFT discussion, a vertical trajectory of the PU chain was used in the MM simulation (opening mode). A supercell was generated from 3\*3\*1 the optimized unit cell of HNT then extended the cell in the z direction to form a vacuum space and embed a PU chain. The PU has moved away from the HNT with equal increments of 0.35 Angstrom as shown in *Figure 5. 1*

Because of computational accuracy, the polymer consistent forcefield (PCFF) with the interface extension (PCFF-IFF) has been used for this section [32], [33]. The PCFF-IFF force field has been developed to achieve a balance between accuracy and efficiency

for modeling materials [32], [33]. It has been employed to a variety of systems. However, it has a limitation, in terms of the inability to adjust the potential for interatomic interactions of new complex systems.

Lately, the energy-fitting method has become a common way to optimize force fields [99], [101]–[103]. Energy-fitting utilizes atomic energy obtained from a high-accurate DFT simulation and energy obtained from MM and minimizes the error between MM-DFT as described following equation 5.5.

$$\chi^2 = \sum_i \left( E_i^{\{inter/DFT\}} - E_i^{\{MM\}} \right)^2$$

5.5

The index  $i$  refers to the unique set of atomic coordinates in the training set. Ercolessi and et. al (1994), [104] presented Energy-fitting for the first time and it was employed in numerous simulations [105]–[108] to expand the efficiency of semi-empirical quantum methods [109], [110].

In order to solve the least-squares problem described in equation 5.5, we explored which Lennard-Jones parameter could minimize the discrepancy between the DFT interaction energy and molecular mechanic potential of all trajectories. The process was started with assigning initial Lennard Jones parameters for interatomic interaction for the molecular mechanic potential, then the interaction energy was computed and compared with the corresponding DFT result. In order to eliminate local interaction, only a specific Lennard Jones parameter was explored that allowed atoms of the PU group to only interact with the atoms of the HNT group or vice versa.

In order to estimate the Lennard-Jones parameters, we are used the Particle Swarm Optimization (PSO) technique [111], [112]. PSO became a very successful approach due to multi-purposes and more consistent exploration for the best answer. The method relocates the particles with a specific speed in every iteration. The “flying bird” is controlled by the best-estimate position of each particle and the excellent-estimate condition by others in the searching area. Consequently, the group converges to a high-grade answer. In the next section we will describe PSO.

During PSO, the least-square minimizing process was applied to minimize the interaction energy difference between DFT and MM. A MATLAB program was used to implement the PSO algorithm process. During iteration, the interaction energy of the MM arrangement was computed and compared with the interaction energy of the corresponding DFT arrangement.

#### **5.4 Particle Swarm Optimization (PSO)**

Force fields contain simplified analytical expressions to calculate total interatomic interactions. These expressions include a set of parameters  $\{\epsilon\}$  and  $\{\sigma\}$  that require to optimize from high-quality reference data at similar chemical conditions and thermodynamic statuses. The efficiency of force fields is restricted to agreement conditions to their reference data. Historically, reference data has usually been derived from experimental or theoretical expression (lattice dimension, bond length) or energetic information. Lately, the reference Energy-matching technic has become a popular method to develop force fields. Energy-matching employs atomic energy obtained from a high-

quality DFT data and minimizes the least-squares deviation. In this section, we introduce our energy-matching method to expand PCFF-IFF force fields for simulating interacting between HNT-PU composite.

There are several non-linear optimization techniques, such as iterative direct gradient minimization methods which correspond to a local minimum (e.g., Levenberg-Marquardt [111]), or global minimum explorations (e.g., simulated annealing [113]), which are computationally expensive for energy matching function.

In our method, the coefficients  $c_i$  and  $d_i$  are assigned to Lennard Jones parameters which are quickly obtained by linear least-squares fitting using the particle swarm optimization (PSO) algorithm. The optimal coefficients were obtained within amplitude bound (upper and lower bound). This amplitude was provided of a 10 percent deviation of the original Lennard Jones coefficients with the PCFF-IFF force field.

PSO algorithm performs as a group of “birds” that are randomly exploring a specific area for food, but there is only one seed. Some birds may not find the location of the food but at least one bird is near the food and it can recognize how far it is. Therefore, a convincing scenario is that following the bird which is close to the seed. PSO operates according to this scenario and implements it to resolve the optimization problems. In PSO the group of birds achieves a unique answer in each iteration.

The population has a fitness variable that is assessed by the matching criteria to be optimized which are the target error (in our case it is  $5 \text{ kcal mol}^{-1}$  for the potential energy of the system). The population has velocities that allow them to fly over explore areas. The

PSO starts by generating the initial particles and assign them a primitive velocity. During iterations, the particle positions and velocities are updated [114], [115]. The new velocity is estimated according to the individual velocity of the bird and the individual best position and the best conditions of their population. The iterations are continued until the PSO approaches an optimum criterion.

The purpose of a nonlinear optimization issue is to identify a variable, for example vector  $Y=[Y_1Y_2Y_3\dots Y_n]$  to describe the target function  $f(Y)$ . The vector variable  $Y$  is determining the state of each bird; This vector describes a parameter with  $n$  dimensions vector, where  $n$  designates the number of parameters that are defined as a problem, which is, discovering the location of the landing bird. The function  $f(Y)$  is a fitness function or goal function, which is evaluating each position  $Y$  as a favorable or unfavorable result, i.e., that means how fine the approaching point which the bird recognizes after each iteration exploration. In our case  $n$  represents the number of Lennard Jones' coefficients for all types of interacting atoms within the simulation and  $f(Y)$  represents the minimize interaction energy as described in equation 5.6 [116].

$$f(Y) = \sum_i \left( E_i^{\{inter/DFT\}} - E_i^{\{MM\}} \right)^2$$

5.6

The index  $i$  refers to a unique set of atomic coordinates in the training set.

Granting a group of birds ( $P$ ) with identification  $i$  for each particle and location vector  $Y_{ti}=(Y_{i1}Y_{i2}Y_{i3}\dots Y_{in})^T$  and a velocity vector  $C_{ti}=(C_{i1}C_{i2}C_{i3} \dots C_{in})^T$  at  $T$  time. The

following equations present the renewed state after each iteration, as we will explain in the next few paragraphs [116]:

$$C_{ij}^{t+1} = wC_{ij}^t + c_1r_1'(pbest_{ij} - Y_{ij}^t) + c_2r_2'(gbest_{ij} - Y_{ij}^t) \quad 5.7$$

And

$$Y_{ij}^{t+1} = Y_{ij}^t + C_{ij}^{t+1} \quad 5.8$$

Where  $i$  refers to each particle ( $i = 1, 2, \dots, P$ ) and  $j$  refers to each iteration ( $j = 1, 2, \dots, n$ ).

Equation 5.7 consists of three terms for each iteration, while, equation 5.8 expresses the update of the bird's locations. The constant value  $w$  refers to the weight parameter which identifies the basic PSO and it is in the range  $0 \leq w < 1$ . This value is essential for adjusting the global search when higher values are choice, or local search exploitation by select lower values. So, this parameter is one of the main distinctions between the classical version of PSO and other versions derived. In our case, we choose 0.8 for  $w$  [116].

The velocity update equation is controlled with parameter  $w$  and the previous velocity of the particle, Therefore, for example, if  $w=1$ , the particle's motion is entirely dependent on the previous motion, so the particle continues travelling in the same direction. On the other hand, if  $0 \leq w < 1$ , the dependent is decreased, which means that a particle preferably travels to other regions in the exploration area. Hence, choose the lower value for parameter  $w$  leads to an increase in the possibility of discovering a global area. However, there is a disadvantage when applying lower  $w$  values, which is increasing computational cost [116].

The individual identification term, which is placed in the second term of Equation 5.7, is determined through averages of the difference between the particle's best position, for example,  $pbest_{ij}$ , and current position  $Y_{ij}^t$ . The concept behind this term is when the particle moves farther away from the  $pbest_{ij}$  position, the difference ( $pbest_{ij}-Y_{ij}^t$ ) needs to increase; Hence, this term increases, pushing the particle to move toward the best position.

The parameter  $c_1$  is a positive constant and refers to an individual-identification parameter, and it considers the effect of previous experiences of particle. The other parameter in the second term is  $r_1$  which is a random value in range  $[0, 1]$ . This random parameter performs an influential role, to avoid abrupt convergences, and consequently increasing the possibility of global optima [116]. In our case, we chose constant 2 for Personal Best (Individual) Learning Coefficient ( $c_1=2$ ).

Finally, the third term in equation 5.7 refers to group awareness. Every particle in the swarm is able to share the information and realizing which one is the best point, for example,  $gbest_j$ . Its term is quite similar to the second term but concerning group exploration. Similarly,  $c_2$  is a group awareness parameter, and it balances the influence of the global exploration of the swarm. And  $r_2$  performs exactly the same function as  $r_1$ . In our case we chose constant 2 for Global Best (Social) Learning Coefficient ( $c_2=2$ ).

In summary, Figure 5. 15 exhibits the flowchart of the PSO algorithm, and the optimization philosophy. All position vectors are evaluated by the function  $f(Y)$  which is identified as the fitness function. Also, Figure 5. 16 displays the updated particle's velocity

base on the position at each iteration, concerning a two-dimensional problem with variables  $Y_1$  and  $Y_2$  [116].

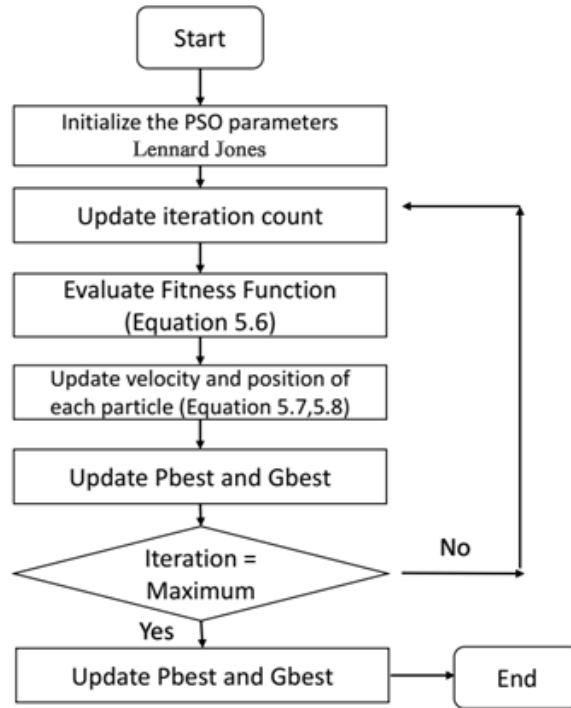


Figure 5. 15: The PSO algorithm

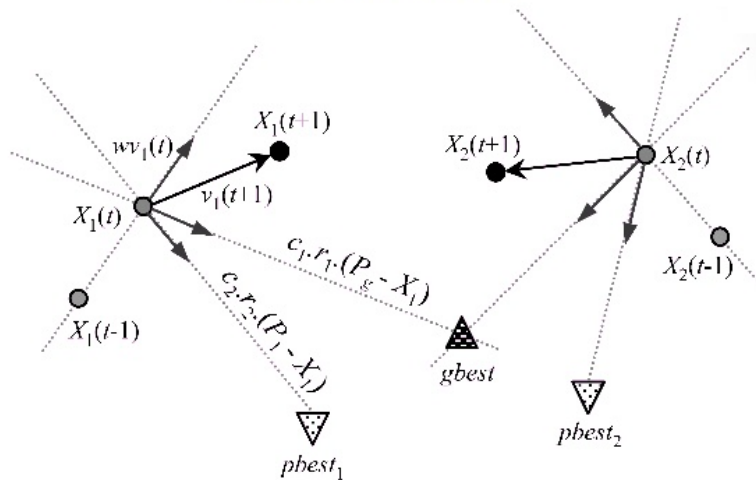
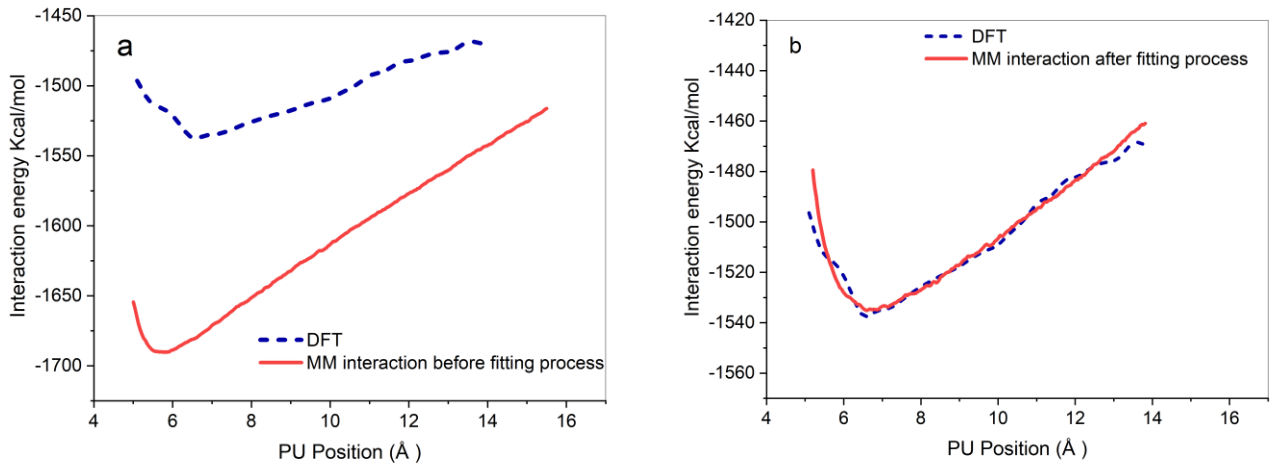


Figure 5. 16: the position vector and the velocity vector being updated at a  $t$  iteration as being composed by two components regarding a bi-dimensional problem [117].

During each iteration of PSO new Leonard-Jones parameters are chosen as the position vector, then the molecular mechanic potential is calculated through LAMMPS [36]. Then interaction potential derived from MM is compared to corresponding reference DFT in each trajectory. Table 5. 1 presents the best-fit Leonard-Jones parameters between HNT/PU computed by DFT and MM approach. Figure 5. 17 shown interaction energy matching results. We are able to implement this modified force field to investigate dynamic response HNT/PU Nano-composite.



**Figure 5. 17:** Interaction energy vs Position of PU chain, a) before and b) after the fitting process

Pairwise non-bonded energy terms were calculated using the following equation:

$$E_{ij} = \frac{q_i q_j}{r} + \epsilon_{ij} \left[ 2 \left( \frac{\sigma_{ij}}{r} \right)^9 - 3 \left( \frac{\sigma_{ij}}{r} \right)^3 \right] \quad 5.9$$

Where  $E_{ij}$  is the non-bonded energy between atoms  $i$  and  $j$ ,  $r$  is the distance between these atoms,  $q_i$  is the charge on atom  $i$  and likewise for atom  $j$ . Lennard-Jones parameters

and charges for HNT and PU atoms were taken from the PCFF-IEFF force field [32], [33]. Pair style used for MM was lj/class2/coul/long.

According to Figure 5. 17 , the new Lenard Jones parameters present good agreement between MM interaction energies with the corresponding DFT results with precision less than (5 kcal mol<sup>-1</sup>).

*Table 5. 1 : improved pair coefficients for classical simulations*

<i>Atom</i>		Al	O	H
C	$\epsilon_{ij}$ (kcal·mol <sup>-1</sup> )	0.033836	0.028527	0.001001
	$\sigma_{ij}$ (Å °)	4.222966	3.892939	3.501295
N	$\epsilon_{ij}$ (kcal·mol <sup>-1</sup> )	0.055334	0.038907	0.001428
	$\sigma_{ij}$ (Å °)	4.419411	3.995249	3.77849
O	$\epsilon_{ij}$ (kcal·mol <sup>-1</sup> )	0.064659	0.057637	0.003619
	$\sigma_{ij}$ (Å °)	3.778643	3.642636	4.338017
H	$\epsilon_{ij}$ (kcal·mol <sup>-1</sup> )	0.014066	0.015391	0.001482
	$\sigma_{ij}$ (Å °)	4.268376	3.456217	2.469121

## 5.5 Model Validation

The previous sections of this chapter showed the capability of applying PSO for energy matching. However, there are several non-linear optimization techniques, such as iterative direct gradient minimization methods (e.g., Levenberg-Marquardt [111]), or global minimum explorations (e.g., simulated annealing [113]), which are computationally expensive compare with our method. However, it is essential at this step to verify the accuracy of our optimization process on simulations. So that, we analyze the strain-stress of PU/HNT with 1% wt of HNT by MD simulations and compare to an experimental sample. The amorphous models in this section were created with 1450 chains of PU. The system has 174801 atoms. LAMMPS was used for all the MD simulations [36]. The

updated potential is applied in this simulation. Following [118], an equilibrium process was applied to the nanocomposite under an NPT ensemble at zero pressure and 500 K for  $5 \times 10^6$  steps. This step allows the grafted chains to move in the periodic cell. During this process, we adopted the PPPM summation method [74] with the Lennard-Jones cutoff radius 18 Å. Also, the time step was 0.1 fs, and PBC was implemented along all directions. The final density of the system was  $0.93826 \text{ g/cm}^{-3}$  as displayed in Figure 5. 18.

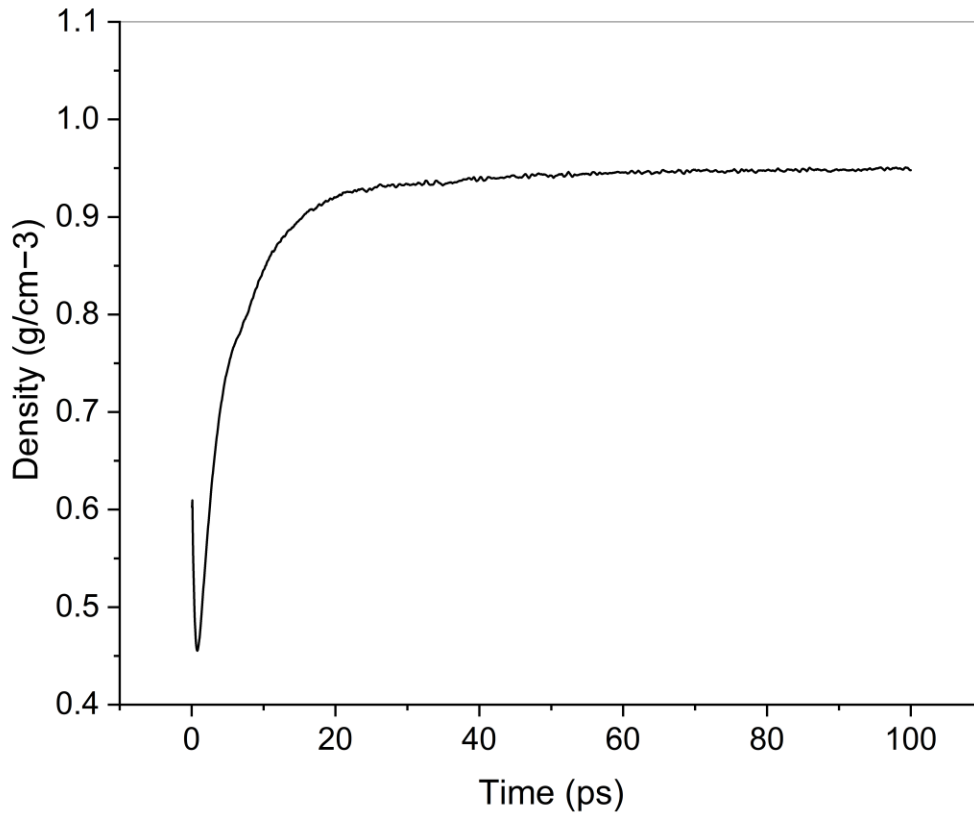


**Figure 5. 18:** density of the system vs time during equilibrium process

After preparation, the PU/HNT structure is deformed by changing the cell length with constant speed (strain rate is  $1 \times 10^9 \text{ s}^{-1}$ ) in the z-direction while the PBC length in the other two directions was fixed (as displayed in Figure 5. 19). The normal stress  $\sigma$  in the

stretching axes was calculated [114], [115], [119], [120]. The resulting stress-strain curve is depicted in Figure 5. 20.

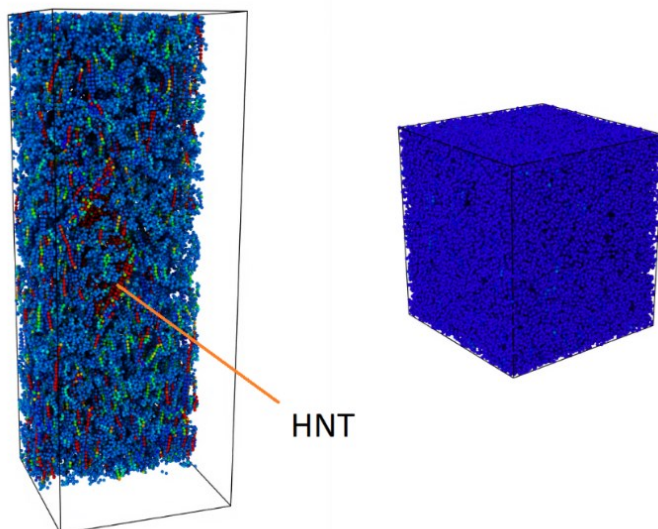


**Figure 5. 19:** *The Molecular dynamics models of PU/HNT composite under the stretching test*

An experimental sample was prepared by Rafaela Aguiar to conduct a uniaxial test. The experimental sample was functionalized with an amino silane and the sample was mixed by loading HNT with PU at 0.8 wt.%. HNT was supplied by Sigma-Aldrich Canada Co[121]. The chemical composition was  $H_4Al_2O_9Si_2 \cdot 2 H_2O$  and the Molecular weight was 294.19 g/mol. Then a tensile test was conducted to measure stress vs relative elongation of the sample. Figure 5. 20 depicts a comparison between MD simulations and experimental.

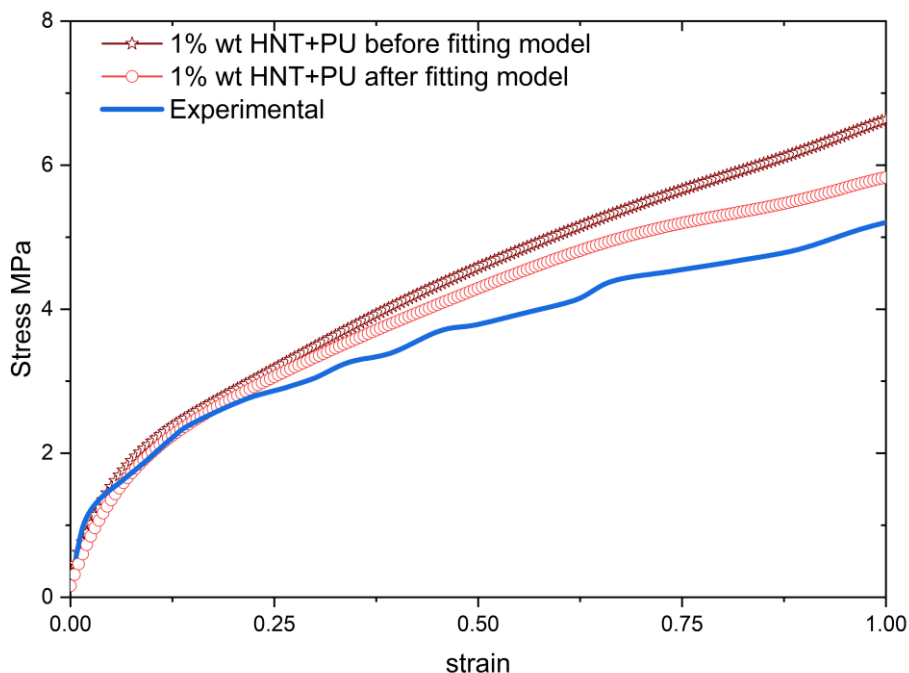


**Figure 5. 20:** Stress-Strain diagram for MD and Experimental PU/HNTs samples

According to the stress-strain result in Figure 5. 20, there is an improved agreement between MD results with the experimental result after our fitting process. However, the discrepancies between MD simulation and experimental are associated with accurate simulation of interatomic interaction, thus, this study was an attempt to eliminate them by PSO.

## 5.6 Concluding Remarks

In this chapter, we introduced a technique to make a bridge between DFT and MM. A machine learning method with the particle swarm optimization algorithm has been applied to energy-matching between MM and DFT calculations.

The advantage of this approach is to minimize the criteria of computational effort. This method was concentrated on the interatomic interaction energy of the structure.

Therefore, the PSO model allows us to accurately predictive intermolecular systems. The new Lennard Jones parameters present good agreement between MD stress-strain responses and the corresponding experimental result. However, discrepancies in adsorption energies came from differences in the atomic charges between the structure in MD and the corresponding quantum values. Moreover, it would be beneficial to expand this approach to improve the link between molecular simulation and properties like the bulk modulus, shear stress, vibration frequency and other forcefields. We left this part for future work.

## Pull-out Simulation

### 6.1 Introduction

In nano-composites, the load transfer from the matrix to a nanoparticle occurs in the interface between the two. This depends on the cohesion strength between nanocomposite components. The interfacial interaction energy can determine the cohesion strength between matrix and nanoparticle. In the case of non-functionalized HNT-PU composites, the interfacial interaction energy is generated from van der Waals forces and Electrostatic forces.

In the current simulation, the mechanical response of HNT-PU nanocomposites to including the interface's influence is restricted. Therefore, the interfacial reaction within atomic simulations is not possible for general loading. As exception is pullout tests, which are represented to shearing loads [122]–[124].

Most studies of the combined loading response concentrate on the effective response of the composite [122]–[124]. Hence, they do not explicitly study the interfacial performance for detachment. Subsequently, many micromechanical simulations predict the effective behaviour of nanocomposites based on an assumption that the interface is completely bonded or partially bonded [125]–[127].

There are two mechanisms to explain the strengthening of a composite by combining fibres. First is the energy absorption when the fibre is pulled out, another is concentrated on the fibre at the crack zone. Usually, resistance to fibre pull-out is an essential way for

achieving better stiffness. Thus, the understanding of the mechanism of the pull-out in the HNT–any polymer composites is essential to increase the stiffness of the nanocomposites augmented by the HNT.

In this chapter, a pull-out simulation has been conducted by the molecular dynamics method to study the effects of the chemical interactions within the HNT-PU nanocomposites. Energy variation has been proposed as cross-links travelling on the HNT. We considered this energy with the updated Lennard Jones parameters.

We again use the PCFF-IFF potential for modelling the interactions between atoms in the current study. However, we used the updated Lennard Jones parameters which were obtained in the previous chapter.

## **6.2 Modeling Simulation**

MD was performed to simulate the pull-out of a single HNT from the PU matrix to determine the interface interaction energy for an HNT-PU nanocomposite. In this simulation, the PU was arranged in a random distribution around the HNT scroll axis. The model applied in this section has a total of 102095 atoms; The computational region was embedding inside a periodic structure. Periodic boundary conditions (PBC) were applied in all directions. The approach of Haghghatpanah (2014) was adopted for the pull-out simulation, the method included the following steps [128]:

step 1: first, geometry optimization (GO) was conducted. GO was performed using conjugate gradient [58] methods and it was continued until the subsequent difference energy steps are less than  $10^{-4}$  kcal/mol.

Step 2: Then the system was equilibrated by using MD and the NPT ensemble at 1 atm pressure and 300 K and for 100 ps. The HNT was constrained during the equilibration. The relaxation process was conducted to eliminate residual stress [118]. The equilibrium step was continued until the average total energy and density reach a constant value. Therefore, the final density of the composite was  $0.4664\text{g/cm}^3$  as displayed in Figure 6. 1.

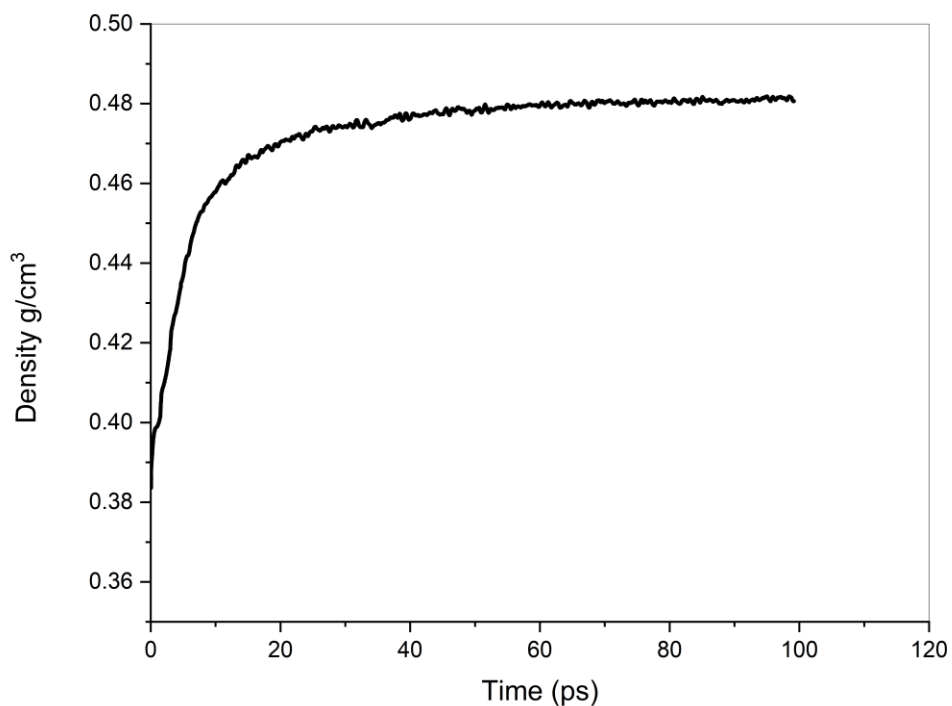


*Figure 6. 1: density of the system vs time during equilibrium process*

Step 3: after the equilibrium stage, the model was subjected to the pullout simulation. First, the PBC was extended along the HNT axis, then the HNT was pulled out from the PU matrix along the HNT axial direction. The left end of the PU matrix was fixed as displayed in Figure 6. 2. The HNT was pulled out of the PU by 0.005 Å displacement increments. During this process, we adopted the PPPM summation method [74] with the Lennard-Jones cutoff radius 18 Å. Figure 6. 3 illustrates the pull out simulation.

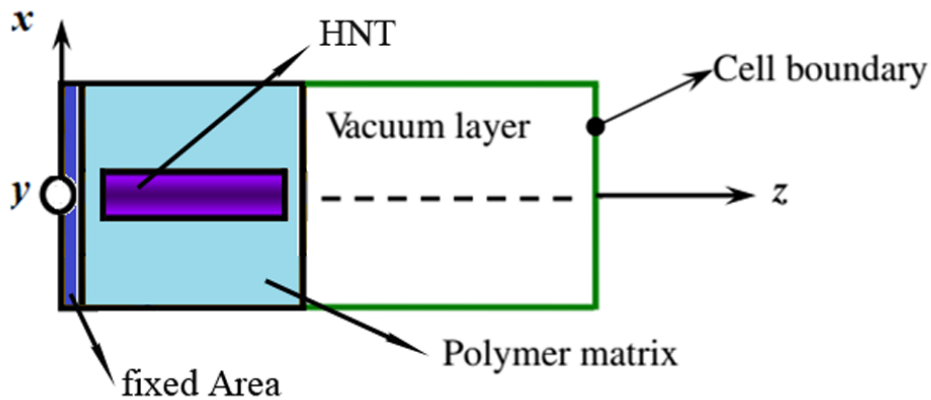


*Figure 6. 2: snapshots pull-out of the HNT from the polymer matrix*

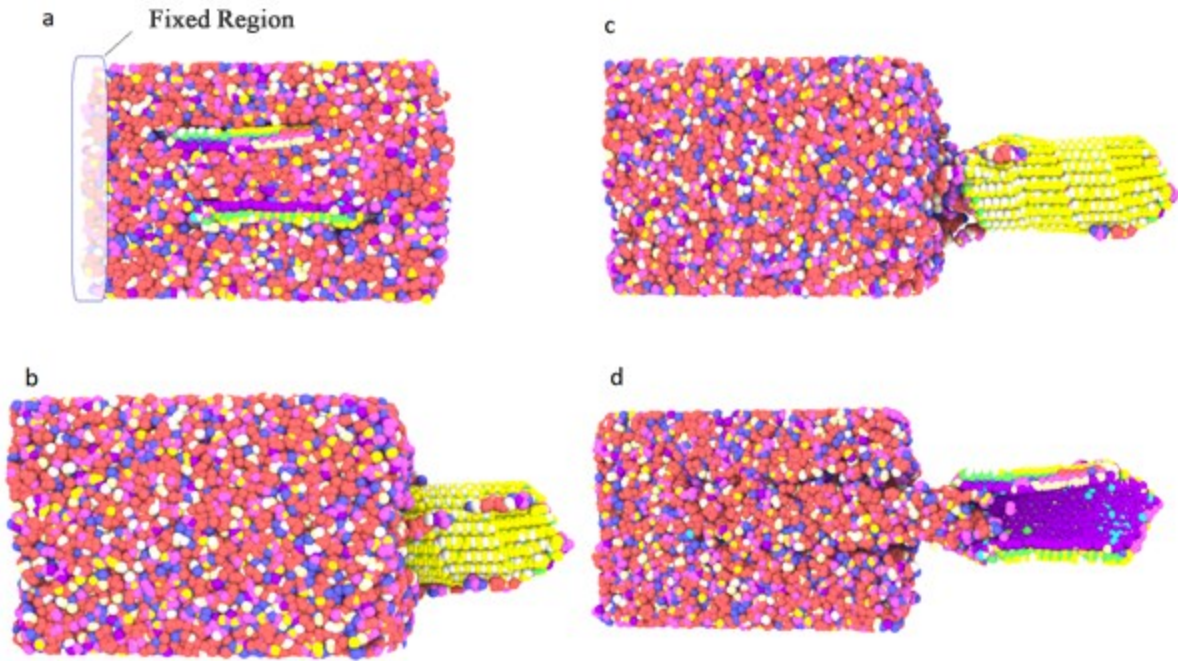


**Figure 6. 3:** pull-out of the HNT from the PU matrix. (a) Fully embedded, (b) at 60 Å displacement of the HNT, (c) fully extracted HNT from PU and (d) cross-cut of fully extracted HNT

### 6.3 Result of Pulling-out Simulation

When the HNT is extracted from the polymer matrix, the total energy is increased, which is directly related to the increase of the potential energy. The potential energy is increasing due to developing new interface areas. Figure 6. 4 depicts the interaction potential energy of the HNT/PU composite for the different increments of the HNT movement during the pull-out simulation. Once the HNT is fully extracted from the matrix, the potential energy reaches a maximum. When the HNT has moved far away from the matrix, the potential energy is decreased.

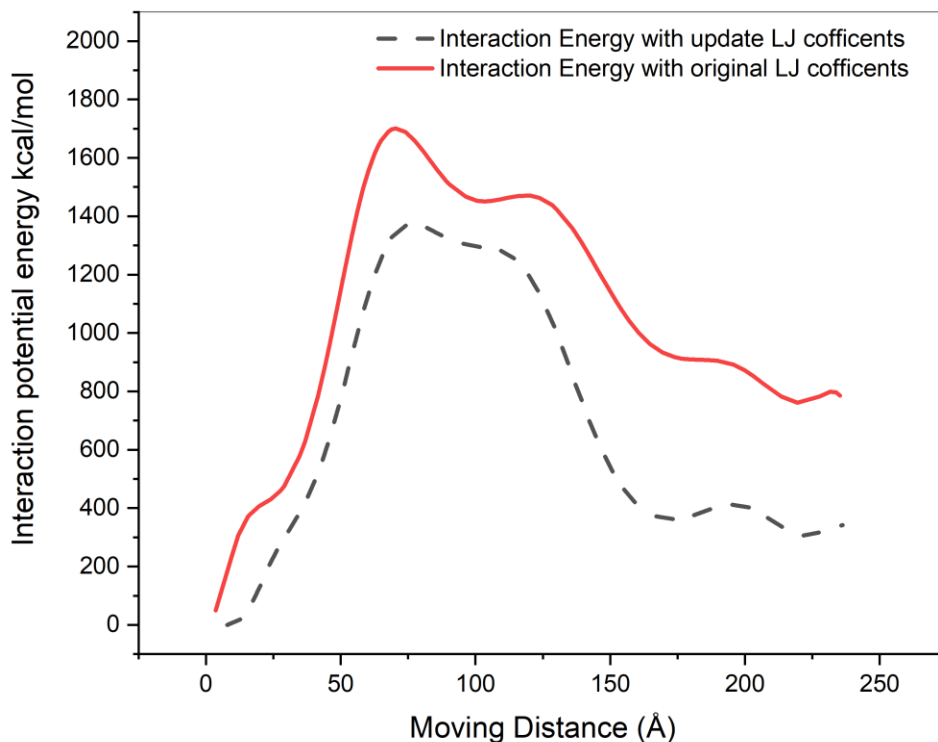


*Figure 6. 4: Interaction potential energy for HNT/PU during the pull-out test*

Gou et al [129] discuss how the variational extraction energy depends on the fully embedded HNT state and the complete pull-out of the PU, and it is associated with the interfacial strength. In addition, during the pull-out process, a few PU chains, particularly those near the Halloysite surface, stay adhered to the HNT and slip away from the remaining PU chains. This shows that some interatomic interactions between HNT and PU chains are stronger than those among the PU chains.

#### **6.4 Conclusions**

In this chapter, we studied the effects of the cross-links between the Halloysite nanotube and polyurethane nanocomposites. For this purpose, molecular dynamics have been used

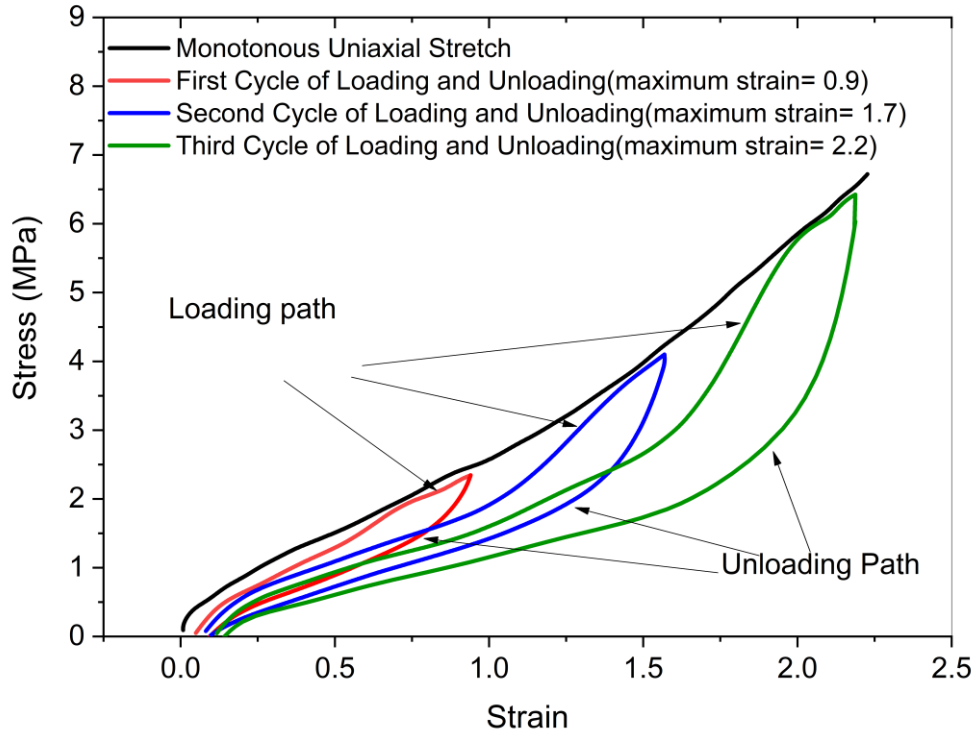
to pull-out HNT from the PU. Energy variation has been proposed as cross-links travelling on the HNT. Once, the HNT is pulling out of the PU, the variation in potential energy increases and finally reaches the summit. It is clear that weakening the HNT/PU bonding (to better match DFT results) leads to a reduction in composite strength, but we note that this effect is only a small contribution to the overall strength of the material.

## Study of Irreversible Strain and Permanent Set of PU Reinforced with HNT

In this chapter, Molecular dynamics (MD) simulation was applied to study the Mullins effect through loading and unloading cyclic tests of polyurethane (PU) reinforced with Halloysite nanotube (HNT). The influences of the stretching cycle rate, different temperatures, the volume of HNT and the density of the hard and soft domain of PU were studied on the permanent set. Also, an Ogden constitutive model and the theory of pseudo-elasticity were adopted to simulate this composite in the ABAQUS software.

### 7.1 Introduction

Elastomer materials experience substantial stress softening when subjected to stretching. As presented in Fig. 1, in a variety of materials such as polymers[130], [131], rubber [132]–[137] and living tissues [138], [139] the Mullins effect phenomenon is recognized. Mullins and Tobin (1957) [140] and Mullins (1969) [137] proposed an expression for modelling the hyperplastic behaviour for this type of material. The majority of stress softening happens at the first cycle, and sequenced cycles of stretching provoke the same or less stress softening. Thereby, the residual strain remains after the first cycle. This residual strain is the so-called permanent set [141].



c

*Figure 7. 1: Schematic of the Mullins effect*

Most studies on the Mullins effect concentrate on the filler [132], [140], however, stress softening is also observed only on the matrix during stress loading (instead of strain). Therefore, both methods indicate a universal principle of these materials. Different types of physical interpretations for this phenomenon have been proposed to date. Generally, we can group them into three categories [142]; (1) interactions between chains in the matrix. (2) the interface between matrix and filler surface, and (3) the bond strength within the reinforcement component [141]. Experimental observation of swelling analyses determined that the fracture in the matrix does not only depend on non-bonded interaction between chains or chain-breaking during the axial test, therefore bond breaking is not the only factor to explain the permanent set [142]. Technically, the challenging aspect of the study of large deformation of rubber material is understanding how microstructure changes

include the interface between polymer chains and polymer chain and filler during the mechanical stretching. However, Ma et al [141] studied the permanent set of a styrene-butadiene–rubber reinforced with silica particles, they employed a coarse-grained (CG), molecular model, without considering different segmental of the polymer composition.

Polyurethane/Halloysite is composed of more than 95% (by weight) content of polyurethane polymer and less than 5% hard mineral ingredient in the form of Halloysite structural. Figure 4. 1 shows the composition of a monomer polyurethane chain employs. In this chapter. The chain is composed of 5 repeating monomers ( $n = 5$ ), and 15 repeating polyol parts ( $m = 15$ ) and one di-isocyanate part.

Again in this section, the polymer consistent forcefield (PCFF) with the interface extension (PCFF-IFF) has been used for this study [29], [30], [32], [143].

In inhomogeneous material, different segments present different stiffness properties. Therefore, the role of each component on the behaviour has to be considered in the nanocomposite. Because of the complexity of elastomer systems combined with a filler, and interfaces between components, studying the Mullins effect and understanding microstructure movement in the nano-scale within the stretching becomes more challenging. A few types of research have been studied at a molecular scale [142], [144]. However, studying the molecular mechanism on the Mullins effect remains controversial. In this section, we develop an MD simulation of a reinforcement PU with HNT to study the atomic scale of the Mullins aspects such as permanent set, stress softening and

recovery. Finally, an Ogden-type constitutive model was derived to model composite with FEM analysis.

## **7.2 Molecular Dynamic Model**

The targeted system is a polyurethane (PU) reinforced with 1% wt Halloysite nanotube (HNT). This percentage is according to the desirable range of [145]. The models in this section were created using an amorphous polymer builder starting with 780 chains of PU and a single HNT with 1803 atoms [146]. The HNTs were randomly embedded in the cell and PU chains were randomly placed around it. The total number of atoms is 447739. All the MD simulations were carried out LAMMPS [36] with the PCFF-IFF force field [32], [33].

Following to Dewapriya and et al (2020) [147], an annealing process was applied upon the nanocomposite arrangement, then three steps of equilibration were performed under an NPT ensemble at zero pressure and a sequence of 300 K, 500 K and 300 K temperatures. During this process, we adopted the PPPM summation method [74] with the Lennard-Jones cutoff radius of 18 Å. Also, the periodic boundary conditions (PBC) were applied in states and the time step was 0.25 fs, and the total time step is 1200 ps, the final density of the composite was 1.1071 g/cm<sup>3</sup>.

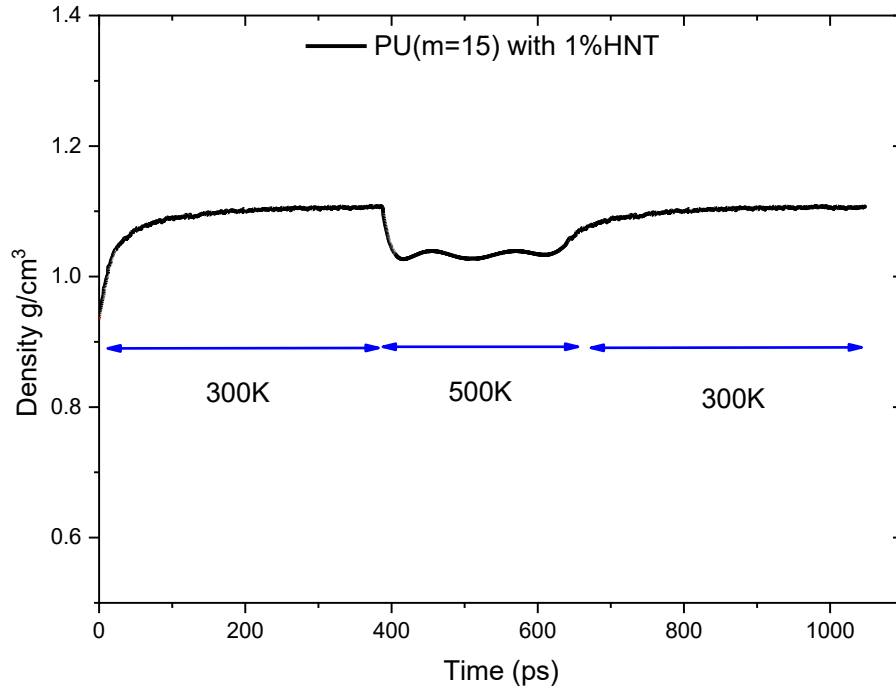


**Figure 7. 2:** Density of models after annealing cycle and relaxation process for PU ( $m=15$ ) with 1% wt HNT,

In the MD simulation, the following approach is applied to study a mechanical stretching test. The PU and HNT systems were stretched by increasing the PBC length with constant speed (strain rate is  $5 \times 10^9 \text{ s}^{-1}$ ) in the z-direction while the other box length directions were unchanged. When we reach a desirable strain, strain rate deformation is removed. During stretching, the NVE ensemble and Langevin thermostat [45] is used to keep the temperature at 1 K. During deformation, we adopted the PPPM summation method [74] with a Lennard-Jones cutoff radius 18 Å. Also, the total time was 50 ps.

### 7.3 Results and Discussion

In this section, MD simulations observation was used to study a permanent set and recovery and microstructure to reveal the root of the Mullins effect.

### 7.3.1 Cyclic Loading

Permanent set is defined as the inability to incapacity to return to the original state. The first detection of the permanent set is observed when the PU/HNT composite was stretched to a maximum of 250% strains and returned to the zero-stress state. It can be noticed From Fig. 4 that, after releasing the load, the PU/HNT composite cannot come back to the original state. Instead, a residual strain remains. The residual strain is 43% when the strain load is 250%.

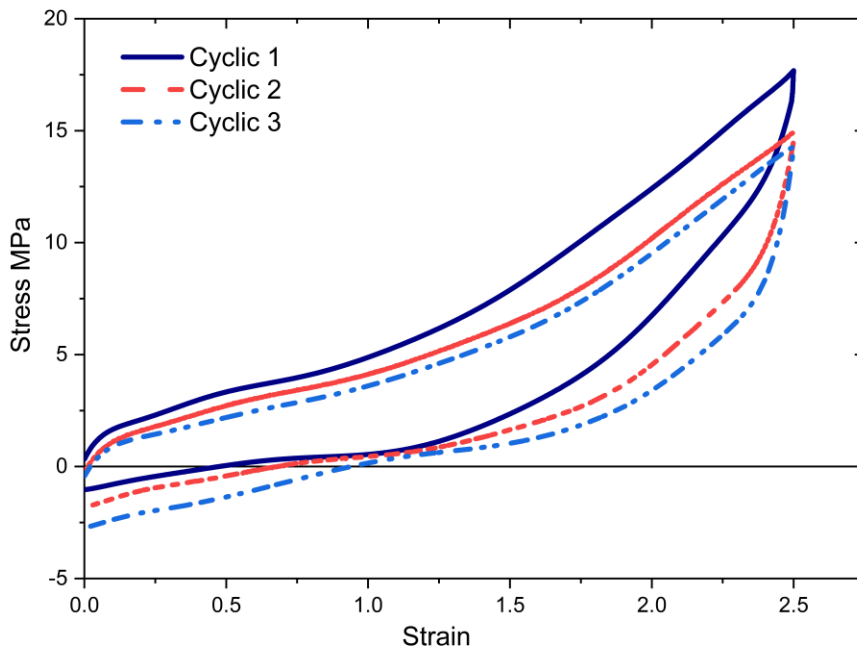
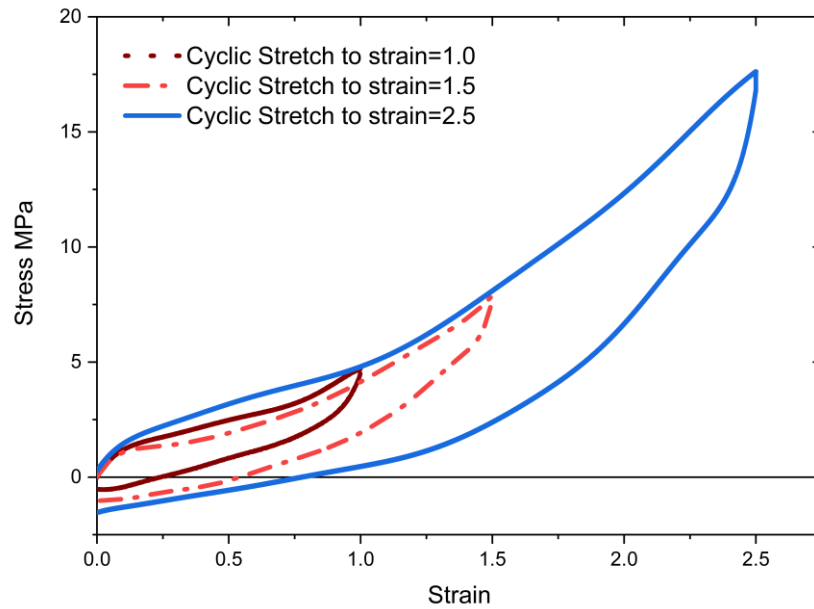


*Figure 7. 3: Stress-strain curves the PU/HNT composite*

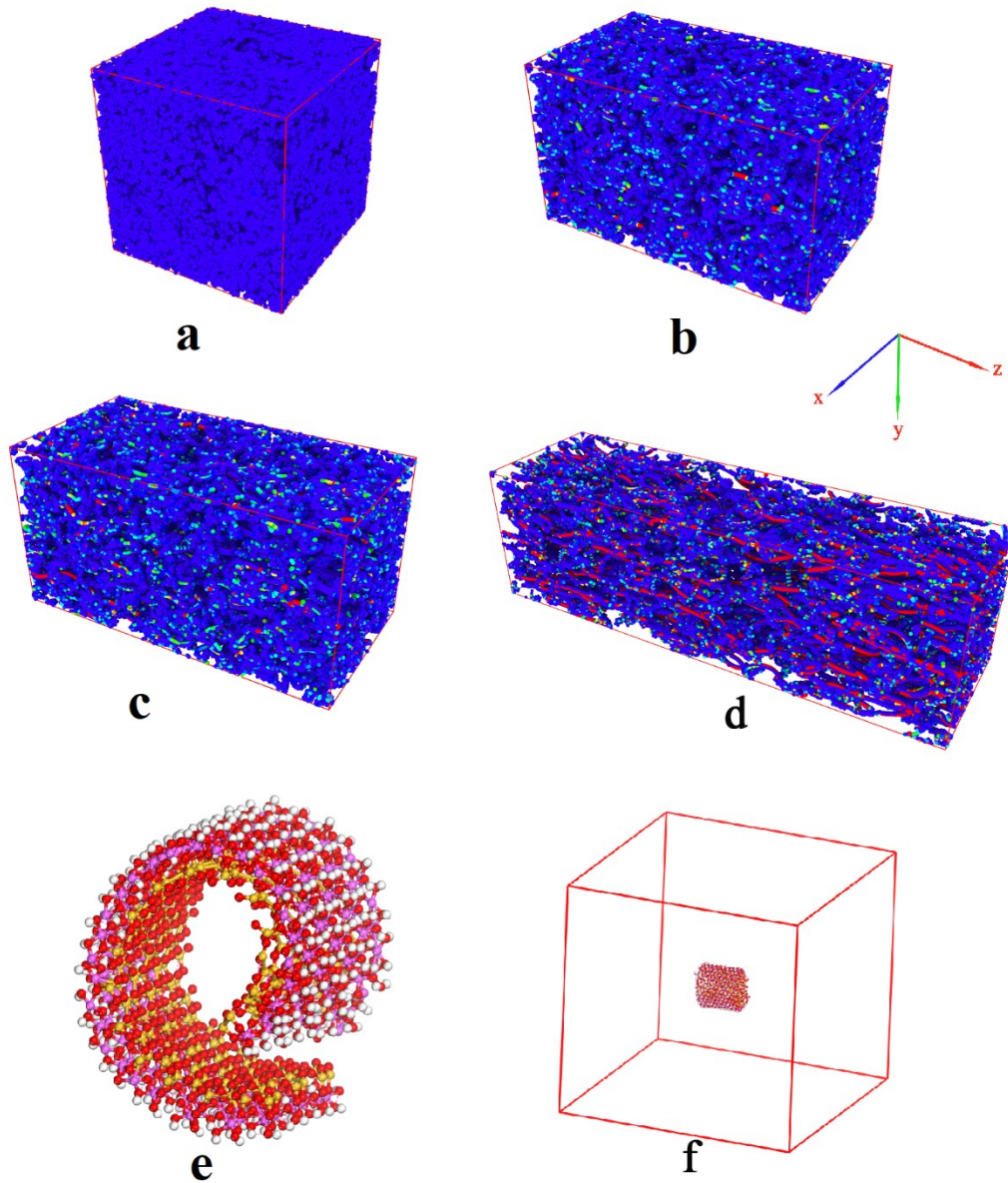
As displayed in Fig. 4, the first stretch generates the majority of stress softening. The stress is reduced considerably between the first two stretch cycles. Also, during the subsequent stretching cycles, the softening rate occurs. The area surrounded by the cyclic curves was used to determine the stress softening which identifies the dissipated energy

density [141]. The value in the first cycle is at  $10.82 \text{ J cm}^3$ , and  $8.96 \text{ J cm}^3$  for the second and  $4.036 \text{ J cm}^3$  for the third cycle.

As presented in Figure 7. 4 we have recognized residual strain was expanded with increasing strain load for example with increasing strain load to 250% the residual strain increases to 25%.



*Figure 7. 4: Stress-strain response of HNT/PU composite versus different strain amplitude from 1 to 1.5 to 2.5.*



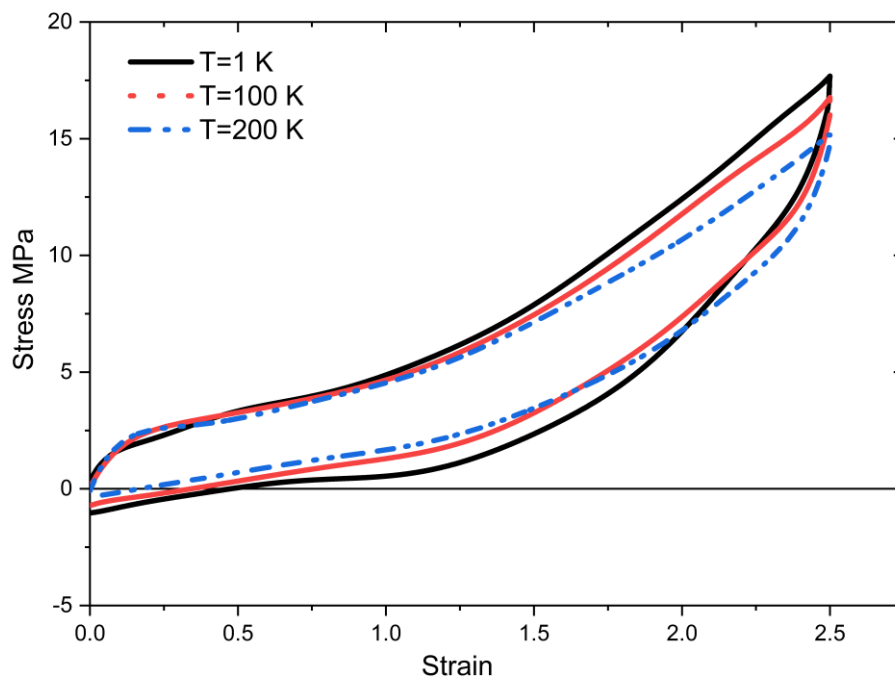
*Figure 7. 5: loading-unloading applied strain cycles, (a) PU/HNT, (b) strain=1, (c) strain=1.5, (d) strain=2.5, (e) Halloysite nanotube,*

Figure 7. 4 shown three loading-unloading applied strain cycles extends from 100% to 150%, to 250%. The stress softening was also observed when the strain loading is surpassed by the previous strain. Also, the stress softening decreases at the subsequent stretch cycles. The dissipated energy density is  $1.51 \text{ J cm}^3$ ,  $2.92 \text{ J cm}^3$  and  $11.36 \text{ J cm}^3$  for first, the second and third cycles respectively. Fig. 6 shows the simulation model. In all

three models, deformation can be detected by two components, the HNT and the matrix. However, the deformation of the polymer chain matrix is more noticeable because the PU has a much lower yield strength.

### 7.3.2 Temperature Evaluates

Generally, the Mullins effect is dependent on the temperature and time, in which the temperature impacts exponentially, and time linearly, the recovery [148], [149]. Also, recovery of the residual set is achievable even at room temperature if relaxed for a long time [150]. The permanent set of nanocomposites is recovered by increasing the temperature. It has been found by various experiments [141], as pictured in Figure 7. 6, that by increasing the temperature from 1K to 200 K, the residual strain is decreased to 52%.



*Figure 7. 6: Recovery of residual strain at different temperatures*

The original simulation is performed at  $T = 1\text{K}$ , without external heat loading. As illustrated in Figure 7. 6, the blue dashed curve refers to the higher temperature ( $T = 200\text{ K}$ ), the red curve refers to the stretching of the nanocomposite at a medium temperature ( $T=100\text{ K}$ ). As depicted in Figure 7. 6, stress softening is seen in the higher temperature system. In order to evaluate the microstructure changes and consistent regeneration which are key characteristics of the Mullins effect, we look at the chain deformation in our MD simulation. Different macroscopic stresses are shown in Figure 7. 8. It can be seen that the folding and unfolding behaviour is compatible with the loading and unloading process.

We also studied the influence of the hard and soft segment ratio of PU on the mechanical response with changing repeating soft segment (SS) density through changing  $m$  (see Figure 4. 1) to 20 and 10. The dispersion energy goes down with an increase in soft segment density as shown in Figure 7. 7.

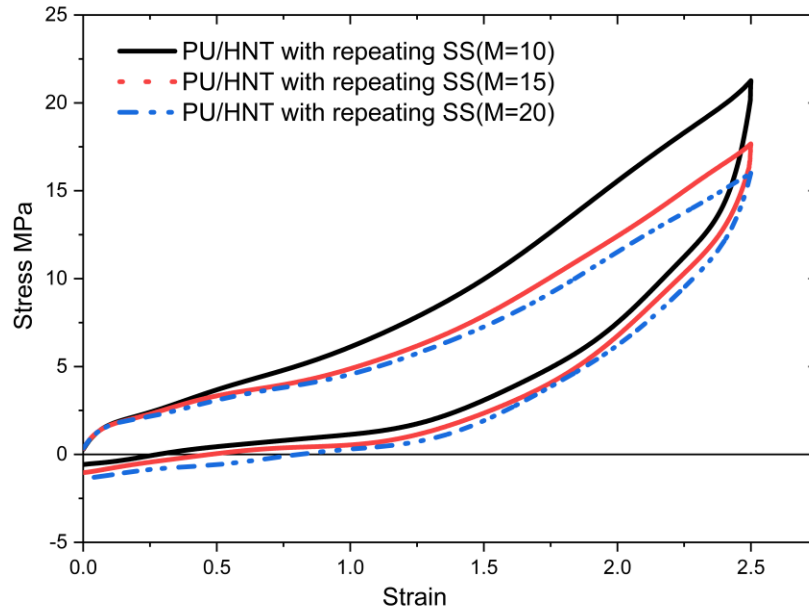


**Figure 7. 7:** Uniaxial stress-strain behavior of HNT/PU in the Hard and soft segment ratio

Figure 7. 7 displays the mechanical response of HNT/PU composite versus a fraction of hard segment content. The hard domains influence the crosslinks and restrict the soft segment mobility. Furthermore, the soft segments control chain mobility. Hence, increasing the hard segment content increases the elastic modulus and tensile strength due to reducing segment mobility. In contrast, increases in hard segment content reduce stress softening. However, increases in hard segment content reduce the soft segment mobility to diffusion which is unfavourable.

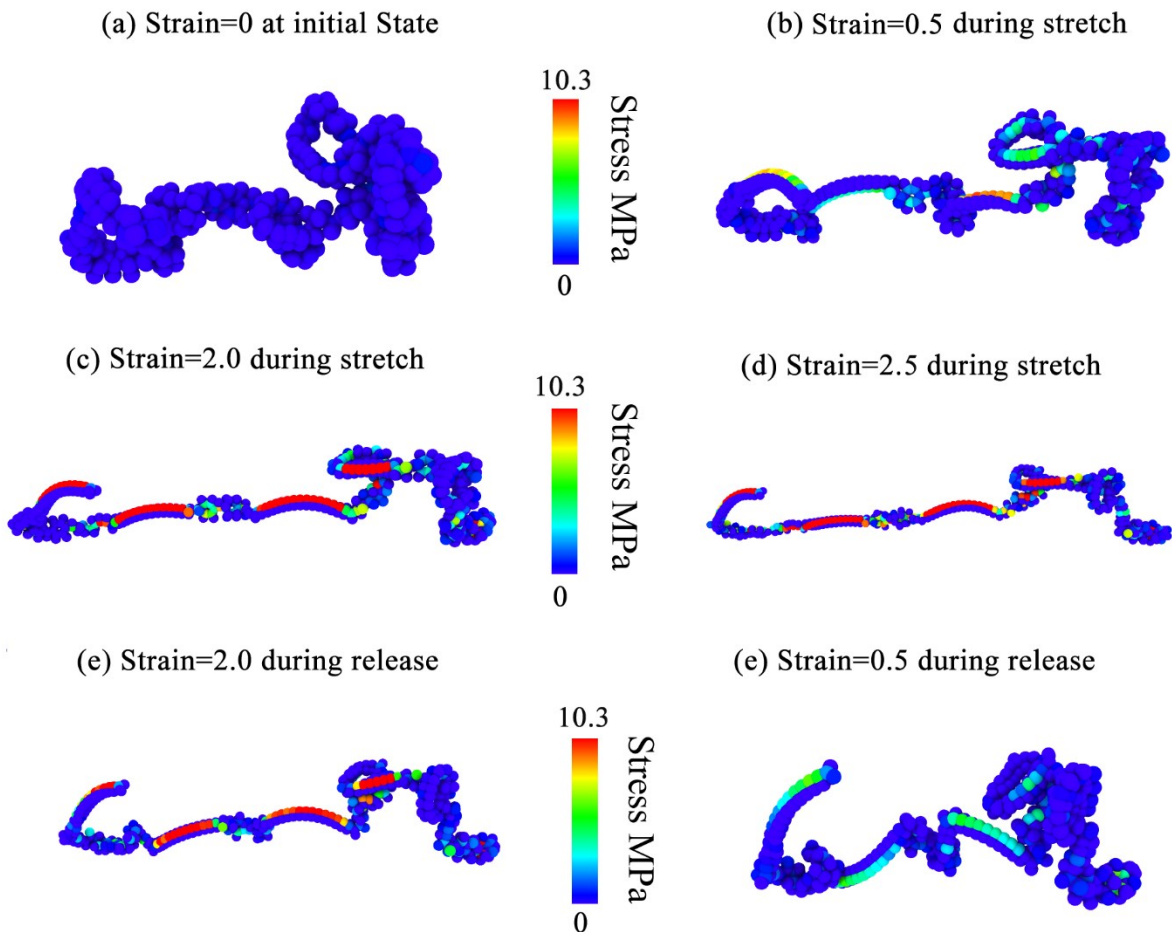


*Figure 7. 8: Expansion of atomic stress for different macroscopic strains.*

It can be observed that the atomic stress during loading tends to be higher than the release process (Figure 7. 8(c) vs. Figure 7. 8(e)). The inverse correlation between atomic stress is a clear, obvious parameter to identify disentanglement.

### **7.3.3 Chain Entanglement Evolution**

The methodology of Hossain and et al [151] was selected to quantify the entanglement of the system. According to their definition, the entanglement parameter was defined as the total fraction of flexion nodes. First, we calculate the angle between two vectors. These vectors are created from each atom to neighbouring atoms that are separated by 10 atoms on the same chain. For example, one vector is generated from atom  $i$  with the atom  $(i + 10)$  and another vector is created between atom  $i$  and atom  $(i - 10)$ . Second, we use a threshold angle of 90 degrees to decide that the atom is classified as entangled or not. Figure 7. 9 displays the distribution of the angle of atoms for the initial and stretched states (strain = 2.5). Figure 7. 10 displays the distribution of the entanglement parameter. Five curves are containing three different strain rates for PU with repeating chain sequence  $m=15$ , and two curves for different repeating chain sequences  $m=10$  and  $m=20$ .

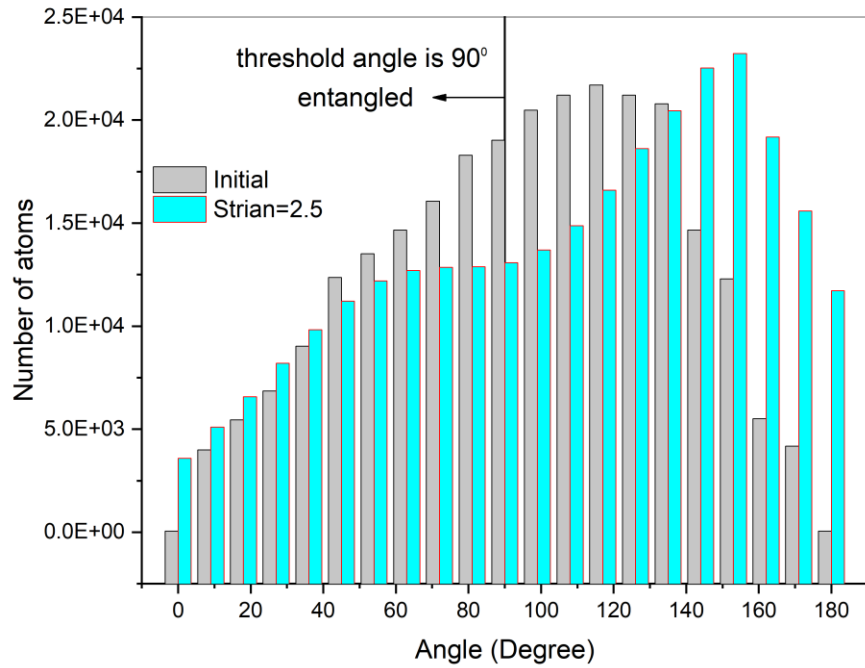


Figure 7. 9: The distribution of the angle of atoms for two states

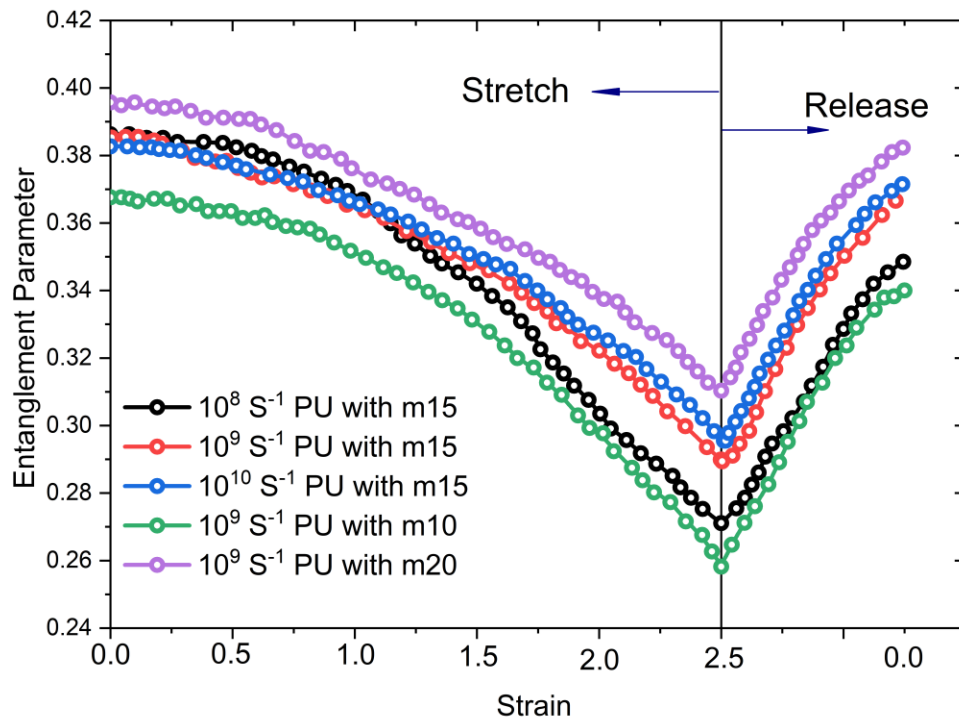
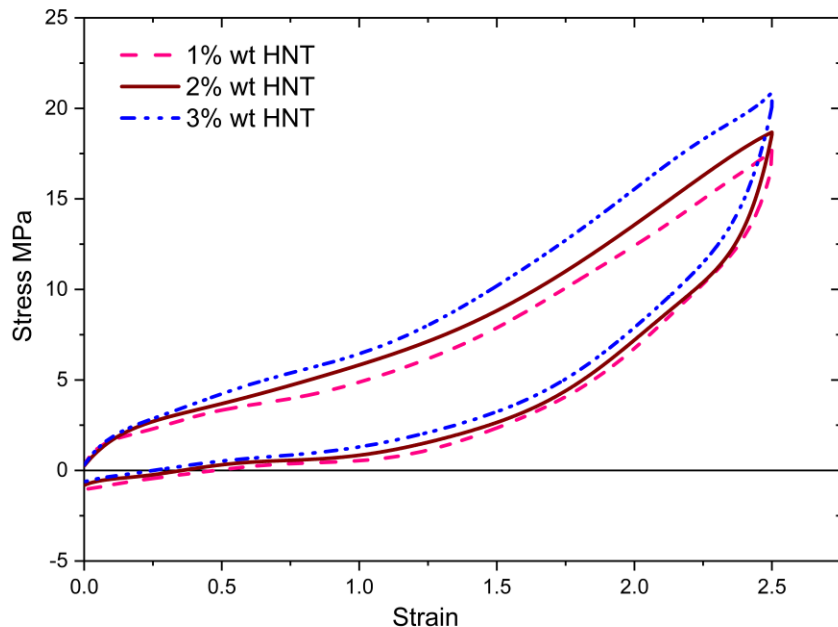


Figure 7. 10: The variation of the entanglement parameter during a stretch–release process.

When there is no external strain, the distribution of the angle of atoms approximately approaching the Gaussian distribution. When the strain increases, the angle between two vectors increases, consequently the entanglement parameter is decreased monotonically. In contrast during the release, the entanglement parameter raises. However, it is not able to reach the initial state. This unrecovered parameter is associated with the permanent set and chain length. Conclusively, the chain entanglement associates with the Mullins effect.

Additionally, we examine the influence of the HNT percentage in nanocomposite on the stretching cycles. The HNT volume fractions are increased from 1.0% to 3.0%. The residual strain goes down with an increase in HNT density as observed in Figure 7. 11, which is compatible with experimental observations [145]. Stress softening was observed in all three cases.



**Figure 7. 11:** *The stress-strain response for different HNT densities in the composite.*

Generally, the larger HNT density leads a lower percentage of the fraction of monomers. This can be interpreted that the HNT provides strong constraints on the polymer chains. Increasing the HNT density puts more restriction on some disentanglements, because of the strong chemical bonding and difficulty to break them. Overall, increased reinforcement causes enhanced entanglements, as well as stronger localized stress concentration. However, the disentanglement is depended on cross-link breakage among chains and between the chain and reinforcement filler. Thereby, there is an optimum value for HNT density beyond which entanglement would be decreased. Previous experimental research presented this percentage at around 0.8-1% wt [145].

#### **7.4 Ogden Pseudo-Elasticity Model**

There are enormous efforts that have been dedicated to formulating and explain the non-linear behaviours of elastomer materials. Ogden and Roxburgh (1999) [152], [153] introduced the idealized Mullins effect in elastomer materials using a softening damage variable. It successfully estimates the hyperplastic stress behaviour with proper expression. The benefit of this model is that it is comparatively easy to obtain a proper expression for hyperplastic behaviour. It can be directly derived from experimental or molecular dynamic data. These pseudo-elastic models are extensively employed due to adjustable and simplicity [154], [155]. In this section, we considering the basic equations of pseudo-elastic material models for HNT/PU composite.

The analytical expression of the strain energy for hyperplastic materials of Ogden(1972, 1982) [153], [156] method is given as follow:

$$W_{Ogden} = \sum_{i=1}^3 \frac{2\mu_i}{\alpha_i^2} (\lambda_1^{\alpha_i} + \lambda_2^{\alpha_i} + \lambda_3^{\alpha_i} - 3) \quad (7.1)$$

The uniaxial stretch is given as follows:

$$\lambda_1 = \lambda, \quad \lambda_2 = \lambda_3 = \lambda^{-1/2} \quad (7.2)$$

For uniaxial tensile stress, the Ogden (N = 3) strain energy is given in the following equation [157]:

$$W_{Ogden} = \sum_{i=1}^3 \frac{2\mu_i}{\alpha_i^2} (\lambda^{\alpha_i} + 2\lambda^{-\alpha_i/2} - 3) \quad (7.3)$$

The stress tensor for an isotropic material is obtained as follows:

$$\sigma_1 = \sigma, \quad \sigma_2 = \sigma_3 = 0 \quad (7.4)$$

The Mullins effect is estimated by applying a strain energy term and a damage function as defined by equ(7.5);

$$W(\lambda, \lambda^{-1/2}, \eta) = \eta W_0(\lambda, \lambda^{-1/2}) + \phi(\eta) \quad (7.5)$$

Where  $W_0(\lambda, \lambda^{-1/2})$  indicate the strain energy in the stretching pathway and  $W(\lambda, \lambda^{-1/2}, \eta)$  for the releasing path, and  $\Phi(\eta)$  indicates the damage function of the material during the loading and unloading deformation [157]. This function determines the energy dissipated during one cyclic loading and it is controlled by variable  $\eta$  which is given by eq (7.6).

$$\eta = 1 - \frac{1}{r} \operatorname{erf} \left( \frac{W^m - W}{m + \beta W^m} \right) \quad (7.6)$$

Where  $W^m$  is the maximum value of  $W$ ;  $r$ ,  $\beta$ , and  $m$  are Mullins effect parameters; and  $\operatorname{erf}(x)$  is the Gaussian error function [157];

In the loading process,  $\eta$  is equal 1 and, in the unloading process,  $\eta$  was declined in a range of  $0 < \eta \leq 1$ . finally, with the above introduction, the stresses are given by

$$\sigma = \lambda \frac{\partial W(\lambda, \lambda^{-1/2}, \eta)}{\partial \lambda} = \lambda \eta \frac{\partial W_0}{\partial \lambda} \quad (7.8)$$

The MATLAB package was used to fit the Ogden constitutive parameters through the Levenberg–Marquardt nonlinear least-squares technique. The parameters of the model were fitted to the MD results from the cyclic loading tests with different strain amplitudes of the PU-HNT composite, table 7.1 provided our result.

*Table 7. 1: Ogden constitutive parameters for loading and unloading curves of PU/HNT composite*

Parameters								
Ogden constitutive model						Mullins Parameters		
$\mu_1/MPa$	$\alpha_1$	$\mu_2/MPa$	$\alpha_2$	$\mu_3/MPa$	$\alpha_3$	$r$	$m/MPa$	$\beta$
0.1829	-9.8825	1.5516	4.9834	3.500	0.4972	1.18	1.2246	0.52

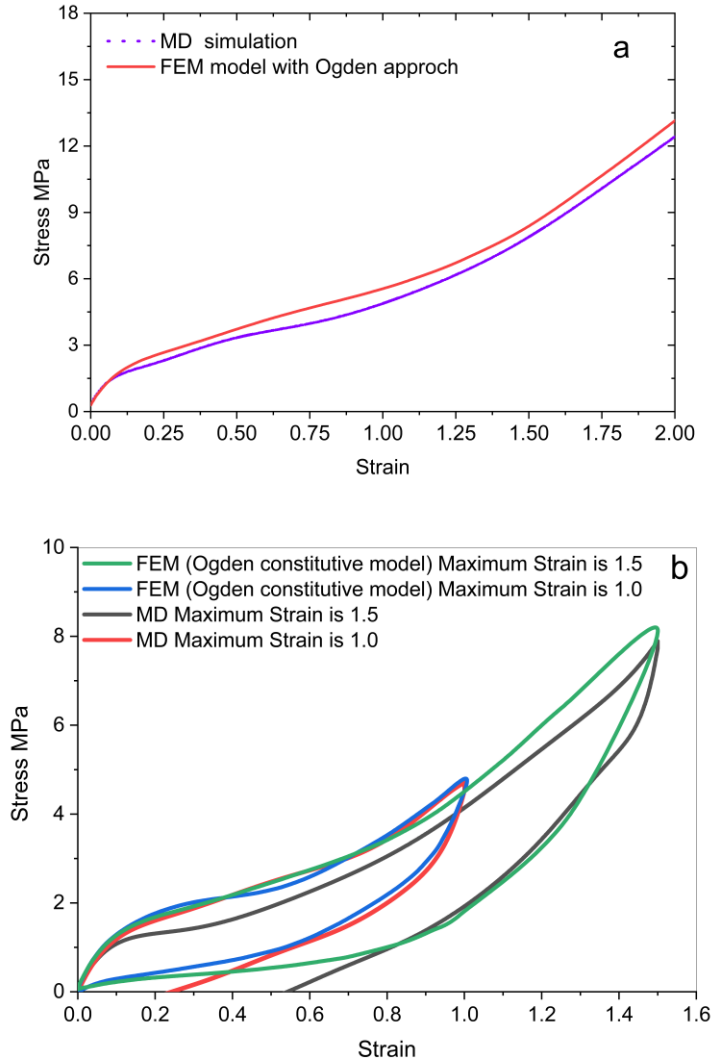


**Figure 7. 12:** (a) indicates loading, and to (b) shows loading and unloading MD and Ogden constitutive models of the simulation.

The hyperplastic behaviour and Mullin's effect were examined in the ABAQUS software with a rectangular planer model under the strain cycle. As depicted in Figure 7. 12, the simulation curves for loading and cyclic loading are basically in agreement with the MD curves. This model has proposed a reasonable prediction of plastic deformation.

### 7.5 Conclusion

To implement HNT in different applications, it is necessary to consider materials exposed to different loading conditions. HNT has extraordinary properties, in specific, stiffness and strength, which make it attractive as the reinforcing element in a composite material. To achieve the full benefit of these properties, it is necessary to understanding the combination with a matrix material. The reason for applying HNT as a reinforcement is cross-linking with the matrix and the influence on the polymer chain entanglement and disentanglement. The characteristics of the composite material are controlled by the features of the HNT and PU as well as the geometry of the interface. We have shown that MD simulation can demonstrate essential aspects of the Mullins effect and microstructure disentanglement of PU chains, which is an effective parameter to identify the residual strain. The analysis of the mechanical response of HNT–PU nanocomposites revealed that the PU chain entanglement is correlated with increasing strain rate. After the first stretch, the disentanglement is not fully reversible, and the permanent set and stress softening begin from the irreversible disentanglement. Generally, the entanglement originates from the interaction interface between HNT and PU and the PU chains together. A significant recovery is achieved when the structure is exposed to a higher temperature. The achieved maximum recovery of the residual strain can be explained by bond breakage, such as between chains, HNT/PU cross-links, and HNT bond breaking during stretching, all of which recover with increasing temperature. Note that the maximum recovery is available when the temperature does not exceed the glass transition temperature. Also, increasing the hard segment content of the PU chains increased the elastic modulus and tensile strength due to reducing segment mobility. In contrast, increases in hard segment content

reduces stress softening. An Ogden constitutive and the theory of pseudo-elasticity has been proposed as a reasonable prediction of plastic deformation of the HNT-PU nanocomposite.

## General Conclusions

Molecular Dynamic (MD) simulations offer a unique perspective on the behavior of chemical and composite systems. However, one of the noticeable issues in MD simulations is the lack of accurate interatomic potentials, which prevents effective prediction of behavior of combination molecular systems.

One feasible solution to the accuracy problem is using direct ab initio calculation, where the quantum-mechanical energy is computed based on atomic configurations at every trajectory. The majority of these methods apply density functional theory to the precise solution of the Schrödinger equation for nuclei and electrons system. However, employing of these methods is restricted to very small systems.

The purpose of machine learning (ML) is to improve efficiently and accurately in computational chemistry [95], [96]. Lately, a variety of complex machine learning algorithms for small and large systems have been proposed based on the total energy data of DFT calculations [158]. Those results are used in ML fitting processes to determine the potential coefficients. Usually, those ML models have been developed for small atomic configurations. In this research, we introduce an alternative method to improve force fields in MM with the precise results of DFT calculations.

Technically, the expansion of a general set of interatomic potentials is a considerable subject for the molecular simulation of the various molecular system [12], [13]. The PCFF-IFF force field provides a general set of interatomic potentials that allow

us to evaluate the complex response of natural materials. However, one of the noticeable issues in the PCFF-IFF force field is its inability to accurately simulate interatomic potentials for complex structures. In this research, a new method has been developed to generate new interatomic parameters for HNT-PU by applying the particle swarm optimization method (PSO) to fit MM calculation to the desirable DFT result, to obtain the best values of the Lennard-Jones parameters of PCFF-IFF potential.

We proposed a framework to increase the accuracy of force fields that can apply for general molecular dynamic systems. This is a significant improvement for conventional molecular simulations. The PSO model allows us to accurately predict intermolecular systems. Although the new Lennard-Jones parameters present good agreement between MM interaction energies and the corresponding DFT results, discrepancies in interaction energies came from differences in the charges of atoms in the MM structure and the corresponding quantum values. Moreover, it would be beneficial to expand these approaches to improve the link between molecular simulation and bulk modulus, shear stress and vibration frequency.

Overall, in this research, we highlighted a promising technique for the bottom-up redesign of nanocomposite materials. We expect that this research will help to understand next-generation nanomaterials. Moreover, this work provided to a broad knowledge of HNT/PU nanocomposites at the atomistic scale, in particular, interface interaction between HNT and polyurethane matrix.

This is a License Agreement between n/a ("You") and Royal Society of Chemistry ("Publisher") provided by Copyright Clearance Center ("CCC"). The license consists of your order details, the terms and conditions provided by Royal Society of Chemistry, and the CCC terms and conditions.

All payments must be made in full to CCC.

<b>Order Date</b>	24-Apr-2021	<b>Type of Use</b>	Republish in a thesis/dissertation
<b>Order License ID</b>	1114080-1	<b>Publisher</b>	ROYAL SOCIETY OF CHEMISTRY
<b>ISSN</b>	1463-9084	<b>Portion</b>	Chapter/article

## LICENSED CONTENT

<b>Publication Title</b>	Physical chemistry chemical physics	<b>Country</b>	United Kingdom of Great Britain and Northern Ireland
<b>Author/Editor</b>	Royal Society of Chemistry (Great Britain)	<b>Rightsholder</b>	Royal Society of Chemistry
<b>Date</b>	01/01/1999	<b>Publication Type</b>	e-Journal
<b>Language</b>	English	<b>URL</b>	<a href="http://firstsearch.oclc.org/journal=1463-9076;screen=info;ECOIP">http://firstsearch.oclc.org/journal=1463-9076;screen=info;ECOIP</a>

## REQUEST DETAILS

<b>Portion Type</b>	Chapter/article	<b>Rights Requested</b>	Main product
<b>Page range(s)</b>	4	<b>Distribution</b>	Canada
<b>Total number of pages</b>	3	<b>Translation</b>	Original language of publication
<b>Format (select all that apply)</b>	Electronic	<b>Copies for the disabled?</b>	No
<b>Who will republish the content?</b>	Academic institution	<b>Minor editing privileges?</b>	Yes
<b>Duration of Use</b>	Life of current edition	<b>Incidental promotional use?</b>	No
<b>Lifetime Unit Quantity</b>	Up to 499	<b>Currency</b>	CAD

## NEW WORK DETAILS

<b>Title</b>	simulation HNT	<b>Institution name</b>	carleton university
<b>Instructor name</b>	carleton	<b>Expected presentation date</b>	2021-09-14

## References

- [1] W. N. Sharpe, *Springer handbook of experimental solid mechanics*. Springer Science & Business Media, 2008.
- [2] J. L. Njoroge, “Atomistic Simulation of Graphene-Polyurethane Nanocomposite for Use in Ballistic Applications.” 2013.
- [3] Z. S. Petrović and J. Ferguson, “Polyurethane elastomers,” *Prog. Polym. Sci.*, vol. 16, no. 5, pp. 695–836, 1991.
- [4] D. K. Chattopadhyay and K. Raju, “Structural engineering of polyurethane coatings for high performance applications,” *Prog. Polym. Sci.*, vol. 32, no. 3, pp. 352–418, 2007.
- [5] C. M. Roland, J. N. Twigg, Y. Vu, and P. H. Mott, “High strain rate mechanical behavior of polyurea,” *Polymer (Guildf)*., vol. 48, no. 2, pp. 574–578, 2007.
- [6] M. B. Khan, “Intelligent viscoelastic polyurethane intrinsic nanocomposites,” *Metall. Mater. Trans. A*, vol. 41, no. 4, pp. 876–880, 2010.
- [7] J. Yi, M. C. Boyce, G. F. Lee, and E. Balizer, “Large deformation rate-dependent stress–strain behavior of polyurea and polyurethanes,” *Polymer (Guildf)*., vol. 47, no. 1, pp. 319–329, 2006.
- [8] J.-H. Lee *et al.*, “High strain rate deformation of layered nanocomposites,” *Nat. Commun.*, vol. 3, no. 1, pp. 1–9, 2012.
- [9] R. Bouaziz, K. Prashantha, and F. Roger, “Thermomechanical modeling of halloysite nanotube-filled shape memory polymer nanocomposites,” *Mech. Adv. Mater. Struct.*, vol. 26, no. 14, pp. 1209–1217, 2019.
- [10] L. Guimaraes, A. N. Enyashin, G. Seifert, and H. A. Duarte, “Structural, electronic, and mechanical properties of single-walled halloysite nanotube models,” *J. Phys. Chem. C*, vol. 114,

- no. 26, pp. 11358–11363, 2010.
- [11] D. A. Prishchenko, E. V Zenkov, V. V Mazurenko, R. F. Fakhrullin, Y. M. Lvov, and V. G. Mazurenko, “Molecular dynamics of the halloysite nanotubes,” *Phys. Chem. Chem. Phys.*, vol. 20, no. 8, pp. 5841–5849, 2018.
- [12] A. Glielmo, C. Zeni, and A. De Vita, “Efficient nonparametric n-body force fields from machine learning,” *Phys. Rev. B*, vol. 97, no. 18, p. 184307, 2018.
- [13] Y.-H. Tang, D. Zhang, and G. E. Karniadakis, “An atomistic fingerprint algorithm for learning ab initio molecular force fields,” *J. Chem. Phys.*, vol. 148, no. 3, p. 34101, 2018.
- [14] J. M. Wills, M. Alouani, P. Andersson, A. Delin, O. Eriksson, and O. Grechnev, *Full-Potential Electronic Structure Method: energy and force calculations with density functional and dynamical mean field theory*, vol. 167. Springer Science & Business Media, 2010.
- [15] E. B. Tadmor and R. E. Miller, *Modeling materials: continuum, atomistic and multiscale techniques*. Cambridge University Press, 2011.
- [16] Z. Wen *et al.*, “DFT Study of the Catalytic Mechanism for Urethane Formation in the Presence of Basic Catalyst 1, 4-diazabicyclo [2.2. 2] octane,” *Commun. Comput. Chem*, vol. 2, pp. 22–35, 2014.
- [17] R. M. Dreizler and E. K. U. Gross, *Density functional theory: an approach to the quantum many-body problem*. Springer Science & Business Media, 2012.
- [18] M. Probert, “Electronic Structure: Basic Theory and Practical Methods, by Richard M. Martin: Scope: graduate level textbook. Level: theoretical materials scientists/condensed matter physicists/computational chemists.” Taylor & Francis, 2011.
- [19] W. Kohn and L. J. Sham, “Self-consistent equations including exchange and correlation effects,” *Phys. Rev.*, vol. 140, no. 4A, p. A1133, 1965.

- [20] A. D. Beck, “Density-functional thermochemistry. III. The role of exact exchange,” *J. Chem. Phys.*, vol. 98, no. 7, pp. 5646–5648, 1993.
- [21] J. P. Perdew, K. Burke, and M. Ernzerhof, “Generalized gradient approximation made simple,” *Phys. Rev. Lett.*, vol. 77, no. 18, p. 3865, 1996.
- [22] C. Lee, W. Yang, and R. G. Parr, “Development of the Colle-Salvetti correlation-energy formula into a functional of the electron density,” *Phys. Rev. B*, vol. 37, no. 2, p. 785, 1988.
- [23] R. Martin, “Electronic structure: basic theory and practical methods Cambridge University Press,” *Cambridge Daw MS, Baskes MI Phys Rev B*, vol. 296443, 2004.
- [24] D. S. Biovia, “Materials Studio,” *R2 (Dassault Systèmes BIOVIA, San Diego, 2017.*
- [25] J. Laun, D. Vilela Oliveira, and T. Bredow, “Consistent gaussian basis sets of double-and triple-zeta valence with polarization quality of the fifth period for solid-state calculations,” *J. Comput. Chem.*, vol. 39, no. 19, pp. 1285–1290, 2018.
- [26] P. E. Blöchl, “Projector augmented-wave method,” *Phys. Rev. B*, vol. 50, no. 24, p. 17953, 1994.
- [27] G. P. Srivastava and D. Weaire, “The theory of the cohesive energies of solids,” *Adv. Phys.*, vol. 36, no. 4, pp. 463–517, 1987.
- [28] J. R. Hill and J. Sauer, “Molecular mechanics potential for silica and zeolite catalysts based on ab initio calculations. 1. Dense and microporous silica,” *J. Phys. Chem.*, vol. 98, no. 4, pp. 1238–1244, 1994.
- [29] H. Sun, “COMPASS: an ab initio force-field optimized for condensed-phase applications overview with details on alkane and benzene compounds,” *J. Phys. Chem. B*, vol. 102, no. 38, pp. 7338–7364, 1998.
- [30] S. L. Mayo, B. D. Olafson, and W. A. Goddard, “DREIDING: a generic force field for molecular

- simulations,” *J. Phys. Chem.*, vol. 94, no. 26, pp. 8897–8909, 1990.
- [31] H. Sun, S. J. Mumby, J. R. Maple, and A. T. Hagler, “An ab initio CFF93 all-atom force field for polycarbonates,” *J. Am. Chem. Soc.*, vol. 116, no. 7, pp. 2978–2987, 1994.
- [32] H. Heinz, R. A. Vaia, H. Koerner, and B. L. Farmer, “Photoisomerization of azobenzene grafted to layered silicates: simulation and experimental challenges,” *Chem. Mater.*, vol. 20, no. 20, pp. 6444–6456, 2008.
- [33] H. Heinz, T.-J. Lin, R. Kishore Mishra, and F. S. Emami, “Thermodynamically consistent force fields for the assembly of inorganic, organic, and biological nanostructures: the INTERFACE force field,” *Langmuir*, vol. 29, no. 6, pp. 1754–1765, 2013.
- [34] S. C. Glotzer and W. Paul, “Molecular and mesoscale simulation methods for polymer materials,” *Annu. Rev. Mater. Res.*, vol. 32, no. 1, pp. 401–436, 2002.
- [35] P. S. Crozier, “A brief survey of the LAMMPS particle simulation code: introduction case studies and future development.,” Sandia National Lab.(SNL-NM), Albuquerque, NM (United States), 2011.
- [36] S. Plimpton, “Fast parallel algorithms for short-range molecular dynamics,” *J. Comput. Phys.*, vol. 117, no. 1, pp. 1–19, 1995.
- [37] J. M. Haile, “Molecular Dynamics Simulation-Elementary Methods, John Willey & Sons,” *Inc.*, New York, 1992.
- [38] J. H. Weiner, *Statistical mechanics of elasticity*. Courier Corporation, 2012.
- [39] J. F. Nye, *Physical properties of crystals: their representation by tensors and matrices*. Oxford university press, 1985.
- [40] D. N. Theodorou and U. W. Suter, “Atomistic modeling of mechanical properties of polymeric

- glasses,” *Macromolecules*, vol. 19, no. 1, pp. 139–154, 1986.
- [41] S. Y. Lim, M. Sahimi, T. T. Tsotsis, and N. Kim, “Molecular dynamics simulation of diffusion of gases in a carbon-nanotube–polymer composite,” *Phys. Rev. E*, vol. 76, no. 1, p. 11810, 2007.
- [42] M. A. Mazo *et al.*, “Molecular dynamics simulation of thermomechanical properties of montmorillonite crystal. 3. Montmorillonite crystals with PEO oligomer intercalates,” *J. Phys. Chem. B*, vol. 112, no. 12, pp. 3597–3604, 2008.
- [43] M. Parrinello and A. Rahman, “Strain fluctuations and elastic constants,” *J. Chem. Phys.*, vol. 76, no. 5, pp. 2662–2666, 1982.
- [44] J. H. Weiner, *Statistical Mechanics of Elasticity*. Courier Corporation, 2002.
- [45] T. Schneider and E. Stoll, “Molecular-dynamics study of a three-dimensional one-component model for distortive phase transitions,” *Phys. Rev. B*, vol. 17, no. 3, p. 1302, 1978.
- [46] M. P. Allen and D. J. Tildesley, *Computer simulation of liquids*. Oxford university press, 2017.
- [47] D. Frenkel and B. Smit, “Understanding molecular simulation: From algorithms to applications,” *Computational sciences series*, vol. 1. Elsevier (formerly published by Academic Press), pp. 1–638, 2002.
- [48] P. J. Flory and M. Volkenstein, “Statistical mechanics of chain molecules.” Wiley Online Library, 1969.
- [49] G. Kresse and D. Joubert, “From ultrasoft pseudopotentials to the projector augmented-wave method,” *Phys. Rev. b*, vol. 59, no. 3, p. 1758, 1999.
- [50] B. Militzer, H.-R. Wenk, S. Stackhouse, and L. Stixrude, “First-principles calculation of the elastic moduli of sheet silicates and their application to shale anisotropy,” *Am. Mineral.*, vol. 96, no. 1, pp. 125–137, 2011.

- [51] J. Greathouse and G. Sposito, "Monte Carlo and Molecular Dynamics Studies of Interlayer Structure in Li (H<sub>2</sub>O) 3- Smectites," *J. Phys. Chem. B*, vol. 102, no. 13, pp. 2406–2414, 1998.
- [52] N. W. Ockwig, J. A. Greathouse, J. S. Durkin, R. T. Cygan, L. L. Daemen, and T. M. Nenoff, "Nanoconfined water in magnesium-rich 2: 1 phyllosilicates," *J. Am. Chem. Soc.*, vol. 131, no. 23, pp. 8155–8162, 2009.
- [53] R. Yendluri, D. P. Otto, M. M. De Villiers, V. Vinokurov, and Y. M. Lvov, "Application of halloysite clay nanotubes as a pharmaceutical excipient," *Int. J. Pharm.*, vol. 521, no. 1–2, pp. 267–273, 2017.
- [54] Y. M. Lvov, D. G. Shchukin, H. Mohwald, and R. R. Price, "Halloysite clay nanotubes for controlled release of protective agents," *ACS Nano*, vol. 2, no. 5, pp. 814–820, 2008.
- [55] B. Lecouvet, J. Horion, C. D'haese, C. Bailly, and B. Nysten, "Elastic modulus of halloysite nanotubes," *Nanotechnology*, vol. 24, no. 10, p. 105704, 2013.
- [56] D. Lu, H. Chen, J. Wu, and C. M. Chan, "Direct measurements of the Young's modulus of a single halloysite nanotube using a transmission electron microscope with a bending stage," *J. Nanosci. Nanotechnol.*, vol. 11, no. 9, pp. 7789–7793, 2011.
- [57] D. Presti, A. Pedone, G. Mancini, C. Duce, M. R. Tiné, and V. Barone, "Insights into structural and dynamical features of water at halloysite interfaces probed by DFT and classical molecular dynamics simulations," *Phys. Chem. Chem. Phys.*, vol. 18, no. 3, pp. 2164–2174, 2016.
- [58] R. Fletcher and C. M. Reeves, "Function minimization by conjugate gradients," *Comput. J.*, vol. 7, no. 2, pp. 149–154, 1964.
- [59] D. L. Bish and C. T. Johnston, "Rietveld refinement and Fourier-transform infrared spectroscopic study of the dickite structure at low temperature," *Clays Clay Miner.*, vol. 41, no. 3, pp. 297–304, 1993.

- [60] P. Ugliengo, C. M. Zicovich-Wilson, S. Tosoni, and B. Civalleri, "Role of dispersive interactions in layered materials: a periodic B3LYP and B3LYP-D\* study of Mg (OH) 2, Ca (OH) 2 and kaolinite," *J. Mater. Chem.*, vol. 19, no. 17, pp. 2564–2572, 2009.
- [61] S. Tosoni, K. Doll, and P. Ugliengo, "Hydrogen bond in layered materials: structural and vibrational properties of kaolinite by a periodic B3LYP approach," *Chem. Mater.*, vol. 18, no. 8, pp. 2135–2143, 2006.
- [62] R. B. Neder, M. Burghammer, T. H. Grasl, H. Schulz, A. Bram, and S. Fiedler, "Refinement of the kaolinite structure from single-crystal synchrotron data," *Clays Clay Miner.*, vol. 47, no. 4, pp. 487–494, 1999.
- [63] B. Singh and R. J. Gilkes, "An electron optical investigation of the alteration of kaolinite to halloysite," *Clays Clay Miner.*, vol. 40, no. 2, pp. 212–229, 1992.
- [64] I. D. M. Robertson and R. A. Eggleton, "Weathering of granitic muscovite to kaolinite and halloysite and of plagioclase-derived kaolinite to halloysite," *Clays Clay Miner.*, vol. 39, no. 2, pp. 113–126, 1991.
- [65] Y. Kuroda, K. Ito, K. Itabashi, and K. Kuroda, "One-step exfoliation of kaolinites and their transformation into nanoscrolls," *Langmuir*, vol. 27, no. 5, pp. 2028–2035, 2011.
- [66] N. Kohyama, K. Fukushima, and A. Fukami, "Observation of the hydrated form of tubular halloysite by an electron microscope equipped with an environmental cell," *Clays Clay Miner.*, vol. 26, no. 1, pp. 25–40, 1978.
- [67] R. R. Anand, R. J. Gilkes, T. M. Armitage, and J. W. Hillyer, "Feldspar weathering in lateritic saprolite," *Clays Clay Miner.*, vol. 33, no. 1, pp. 31–43, 1985.
- [68] S. W. Bailey, "Surface chemistry structure and mixed layering of clays," in *Proceedings of the 9th Int. Clay Conf. Sciences Geologiques, Memoire*, 1990, vol. 86, pp. 89–98.

- [69] E. Joussein, S. Petit, J. Churchman, B. Theng, D. Righi, and B. Delvaux, “Halloysite clay minerals—a review,” *Clay Miner.*, vol. 40, no. 4, pp. 383–426, 2005.
- [70] Y. Lvov, W. Wang, L. Zhang, and R. Fakhrullin, “Halloysite clay nanotubes for loading and sustained release of functional compounds,” *Adv. Mater.*, vol. 28, no. 6, pp. 1227–1250, 2016.
- [71] F. Ferrante, N. Armata, and G. Lazzara, “Modeling of the halloysite spiral nanotube,” *J. Phys. Chem. C*, vol. 119, no. 29, pp. 16700–16707, 2015.
- [72] R. D. White, D. V Bavykin, and F. C. Walsh, “Spontaneous scrolling of  $\text{Al}_2\text{Si}_2\text{O}_5(\text{OH})_4$  nanosheets into halloysite nanotubes stimulated by structural doping with  $\text{GeO}_2$ ,” in *2012 12th IEEE International Conference on Nanotechnology (IEEE-NANO)*, 2012, pp. 1–4.
- [73] H. Heinz and H. Ramezani-Dakhel, “Simulations of inorganic–bioorganic interfaces to discover new materials: insights, comparisons to experiment, challenges, and opportunities,” *Chem. Soc. Rev.*, vol. 45, no. 2, pp. 412–448, 2016.
- [74] R. W. Hockney and J. W. Eastwood, *Computer simulation using particles*. crc Press, 1988.
- [75] G. Kresse and J. Furthmüller, “Efficient iterative schemes for ab initio total-energy calculations using a plane-wave basis set,” *Phys. Rev. B*, vol. 54, no. 16, p. 11169, 1996.
- [76] A. Dadrasi, A. R. Albooyeh, and A. H. Mashhadzadeh, “Mechanical properties of silicon-germanium nanotubes: A molecular dynamics study,” *Appl. Surf. Sci.*, vol. 498, p. 143867, 2019.
- [77] H. Yang, M. He, C. Lu, and W. Gong, “Deformation and failure processes of kaolinite under tension: Insights from molecular dynamics simulations,” *Sci. CHINA Physics, Mech. Astron.*, vol. 62, no. 6, p. 64612, 2019.
- [78] M. S. Daw and M. I. Baskes, “Embedded-atom method: Derivation and application to impurities, surfaces, and other defects in metals,” *Phys. Rev. B*, vol. 29, no. 12, p. 6443, 1984.

- [79] X. H. Fan *et al.*, “Application of Materials Studio modeling in crystal structure,” in *Advanced Materials Research*, 2013, vol. 706, pp. 7–10.
- [80] M. Moniruzzaman and K. I. Winey, “Polymer nanocomposites containing carbon nanotubes,” *Macromolecules*, vol. 39, no. 16, pp. 5194–5205, 2006.
- [81] S. Thomas and G. E. Zaikov, *Polymer nanocomposite research advances*. Nova Publishers, 2008.
- [82] S. S. Sarva, S. Deschanel, M. C. Boyce, and W. Chen, “Stress–strain behavior of a polyurea and a polyurethane from low to high strain rates,” *Polymer (Guildf.)*, vol. 48, no. 8, pp. 2208–2213, 2007.
- [83] S. Al-Malaika, A. Golovoy, and C. A. Wilkie, *Chemistry and technology of polymer additives*, vol. 1. Blackwell Science Oxford, 1999.
- [84] Y. A. Bahei-El-Din and G. J. Dvorak, “Behavior of sandwich plates reinforced with polyurethane/polyurea interlayers under blast loads,” *J. Sandw. Struct. Mater.*, vol. 9, no. 3, pp. 261–281, 2007.
- [85] J. O. Akindoyo, M. Beg, S. Ghazali, M. R. Islam, N. Jeyaratnam, and A. R. Yuvaraj, “Polyurethane types, synthesis and applications—a review,” *Rsc Adv.*, vol. 6, no. 115, pp. 114453–114482, 2016.
- [86] A. software Inc, “Accelrys Material Studio Release 5.0,” 2009.
- [87] J. Hafner, “Atomic-scale computational materials science,” *Acta Mater.*, vol. 48, no. 1, pp. 71–92, 2000.
- [88] H. Warlimont and W. Martienssen, “Springer Handbook of Condensed Matter and Materials Data.” New York: Springer Berlin Heidelberg, 2005.
- [89] J. Bicerano, *Prediction of polymer properties*. cRc Press, 2002.

- [90] W. L. Tham, B. T. Poh, Z. A. M. Ishak, and W. S. Chow, “Thermal behaviors and mechanical properties of halloysite nanotube-reinforced poly (lactic acid) nanocomposites,” *J. Therm. Anal. Calorim.*, vol. 118, no. 3, pp. 1639–1647, 2014.
- [91] V. P. Singh, K. K. Vimal, G. S. Kapur, S. Sharma, and V. Choudhary, “High-density polyethylene/halloysite nanocomposites: morphology and rheological behaviour under extensional and shear flow,” *J. Polym. Res.*, vol. 23, no. 3, p. 43, 2016.
- [92] N. Ning, Q. Yin, F. Luo, Q. Zhang, R. Du, and Q. Fu, “Crystallization behavior and mechanical properties of polypropylene/halloysite composites,” *Polymer (Guildf.)*, vol. 48, no. 25, pp. 7374–7384, 2007.
- [93] H. Ismail, S. Z. Salleh, and Z. Ahmad, “Properties of halloysite nanotubes-filled natural rubber prepared using different mixing methods,” *Mater. Des.*, vol. 50, pp. 790–797, 2013.
- [94] W. Chen, X. Tao, and Y. Liu, “Carbon nanotube-reinforced polyurethane composite fibers,” *Compos. Sci. Technol.*, vol. 66, no. 15, pp. 3029–3034, 2006.
- [95] Y. M. Muñoz-Muñoz, G. Guevara-Carrion, M. Llano-Restrepo, and J. Vrabc, “Lennard-Jones force field parameters for cyclic alkanes from cyclopropane to cyclohexane,” *Fluid Phase Equilib.*, vol. 404, pp. 150–160, 2015.
- [96] P. Xu, E. B. Guidez, C. Bertoni, and M. S. Gordon, “Perspective: Ab initio force field methods derived from quantum mechanics,” *J. Chem. Phys.*, vol. 148, no. 9, p. 90901, 2018.
- [97] J. Behler and M. Parrinello, “Generalized neural-network representation of high-dimensional potential-energy surfaces,” *Phys. Rev. Lett.*, vol. 98, no. 14, p. 146401, 2007.
- [98] K. Yao, J. E. Herr, D. W. Toth, R. Mckintyre, and J. Parkhill, “The TensorMol-0.1 model chemistry: a neural network augmented with long-range physics,” *Chem. Sci.*, vol. 9, no. 8, pp. 2261–2269, 2018.

- [99] F. A. Faber *et al.*, “Prediction errors of molecular machine learning models lower than hybrid DFT error,” *J. Chem. Theory Comput.*, vol. 13, no. 11, pp. 5255–5264, 2017.
- [100] A. Mardt, L. Pasquali, H. Wu, and F. Noé, “VAMPnets for deep learning of molecular kinetics,” *Nat. Commun.*, vol. 9, no. 1, pp. 1–11, 2018.
- [101] S. Chmiela, A. Tkatchenko, H. E. Sauceda, I. Poltavsky, K. T. Schütt, and K.-R. Müller, “Machine learning of accurate energy-conserving molecular force fields,” *Sci. Adv.*, vol. 3, no. 5, p. e1603015, 2017.
- [102] K. Hansen *et al.*, “Machine learning predictions of molecular properties: Accurate many-body potentials and nonlocality in chemical space,” *J. Phys. Chem. Lett.*, vol. 6, no. 12, pp. 2326–2331, 2015.
- [103] J. Behler, “Erratum: ‘Perspective: Machine learning potentials for atomistic simulations’ [J. Chem. Phys. 145, 170901 (2016)],” *J. Chem. Phys.*, vol. 145, no. 21, p. 219901, 2016.
- [104] F. Ercolessi and J. B. Adams, “Interatomic potentials from first-principles calculations: the force-matching method,” *EPL (Europhysics Lett.)*, vol. 26, no. 8, p. 583, 1994.
- [105] E. R. Pinnick, C. E. Calderon, A. J. Rusnak, and F. Wang, “Achieving fast convergence of ab initio free energy perturbation calculations with the adaptive force-matching method,” *Theor. Chem. Acc.*, vol. 131, no. 3, pp. 1–11, 2012.
- [106] D. Wei, Y. Song, and F. Wang, “A simple molecular mechanics potential for  $\mu\text{m}$  scale graphene simulations from the adaptive force matching method,” *J. Chem. Phys.*, vol. 134, no. 18, p. 184704, 2011.
- [107] O. Akin-Ojo and F. Wang, “The quest for the best nonpolarizable water model from the adaptive force matching method,” *J. Comput. Chem.*, vol. 32, no. 3, pp. 453–462, 2011.
- [108] S. Izvekov, M. Parrinello, C. J. Burnham, and G. A. Voth, “Effective force fields for condensed

- phase systems from ab initio molecular dynamics simulation: A new method for force-matching,” *J. Chem. Phys.*, vol. 120, no. 23, pp. 10896–10913, 2004.
- [109] N. Goldman, “Multi-center semi-empirical quantum models for carbon under extreme thermodynamic conditions,” *Chem. Phys. Lett.*, vol. 622, pp. 128–136, 2015.
- [110] M. Welborn, J. Chen, L. Wang, and T. Van Voorhis, “Why many semiempirical molecular orbital theories fail for liquid water and how to fix them,” *J. Comput. Chem.*, vol. 36, no. 12, pp. 934–939, 2015.
- [111] K. Levenberg, “A method for the solution of certain non-linear problems in least squares,” *Q. Appl. Math.*, vol. 2, no. 2, pp. 164–168, 1944.
- [112] J. Kennedy and R. Eberhart, “Particle swarm optimization,” in *Proceedings of ICNN’95-international conference on neural networks*, 1995, vol. 4, pp. 1942–1948.
- [113] E. H. L. Aarts, “Simulated annealing: Theory and applications,” 1987.
- [114] D. R. Rottach, J. G. Curro, J. Budzien, G. S. Grest, C. Svaneborg, and R. Everaers, “Permanent set of cross-linking networks: Comparison of theory with molecular dynamics simulations,” *Macromolecules*, vol. 39, no. 16, pp. 5521–5530, 2006.
- [115] D. R. Rottach, J. G. Curro, J. Budzien, G. S. Grest, C. Svaneborg, and R. Everaers, “Molecular dynamics simulations of polymer networks undergoing sequential cross-linking and scission reactions,” *Macromolecules*, vol. 40, no. 1, pp. 131–139, 2007.
- [116] B. S. G. de Almeida and V. C. Leite, “Particle swarm optimization: A powerful technique for solving engineering problems,” in *Swarm Intelligence-Recent Advances, New Perspectives and Applications*, IntechOpen, 2019.
- [117] D. Wang, D. Tan, and L. Liu, “Particle swarm optimization algorithm: an overview,” *Soft Comput.*, vol. 22, no. 2, pp. 387–408, 2018.

- [118] W. Peng, R. Ranganathan, P. Keblinski, P. Akcora, and R. Ozisik, “Viscoelastic and dynamic properties of polymer grafted nanocomposites with high glass transition temperature graft chains,” *J. Appl. Phys.*, vol. 126, no. 19, p. 195102, 2019.
- [119] Y. Gao, J. Liu, J. Shen, L. Zhang, Z. Guo, and D. Cao, “Uniaxial deformation of nanorod filled polymer nanocomposites: a coarse-grained molecular dynamics simulation,” *Phys. Chem. Chem. Phys.*, vol. 16, no. 30, pp. 16039–16048, 2014.
- [120] D. R. Rottach, J. G. Curro, G. S. Grest, and A. P. Thompson, “Effect of strain history on stress and permanent set in cross-linking networks: A molecular dynamics study,” *Macromolecules*, vol. 37, no. 14, pp. 5468–5473, 2004.
- [121] B. Sigma-Aldrich and P. S.-A. Region, “SIG MA-ALDRICH,” *Sigma*, vol. 302, no. H311, p. H331, 2018.
- [122] G. M. Odegard, T. S. Gates, K. E. Wise, C. Park, and E. J. Siochi, “Constitutive modeling of nanotube–reinforced polymer composites,” *Compos. Sci. Technol.*, vol. 63, no. 11, pp. 1671–1687, 2003.
- [123] J. Schneider *et al.*, “ATK-ForceField: a new generation molecular dynamics software package,” *Model. Simul. Mater. Sci. Eng.*, vol. 25, no. 8, p. 85007, 2017.
- [124] S. J. V Frankland, V. M. Harik, G. M. Odegard, D. W. Brenner, and T. S. Gates, “The stress–strain behavior of polymer–nanotube composites from molecular dynamics simulation,” *Compos. Sci. Technol.*, vol. 63, no. 11, pp. 1655–1661, 2003.
- [125] Y. J. Liu and X. L. Chen, “Evaluations of the effective material properties of carbon nanotube-based composites using a nanoscale representative volume element,” *Mech. Mater.*, vol. 35, no. 1–2, pp. 69–81, 2003.
- [126] G. D. Seidel and D. C. Lagoudas, “Micromechanical analysis of the effective elastic properties of

- carbon nanotube reinforced composites,” *Mech. Mater.*, vol. 38, no. 8–10, pp. 884–907, 2006.
- [127] A. P. Awasthi, D. C. Lagoudas, and D. C. Hammerand, “Modeling of graphene–polymer interfacial mechanical behavior using molecular dynamics,” *Model. Simul. Mater. Sci. Eng.*, vol. 17, no. 1, p. 15002, 2008.
- [128] S. Haghghatpanah, M. Bohlén, and K. Bolton, “Molecular level computational studies of polyethylene and polyacrylonitrile composites containing single walled carbon nanotubes: effect of carboxylic acid functionalization on nanotube–polymer interfacial properties,” *Front. Chem.*, vol. 2, p. 74, 2014.
- [129] J. Gou, S. Jiang, B. Minaie, Z. Liang, C. Zhang, and B. Wang, “Nanoscale Modeling and Simulation of Interfacial Bonding of Single-Walled Nanotube Reinforced Composites,” in *ASME International Mechanical Engineering Congress and Exposition*, 2003, vol. 37149, pp. 815–819.
- [130] S. Hirotsu, “Softening of bulk modulus and negative Poisson’s ratio near the volume phase transition of polymer gels,” *J. Chem. Phys.*, vol. 94, no. 5, pp. 3949–3957, 1991.
- [131] R. E. Webber, C. Creton, H. R. Brown, and J. P. Gong, “Large strain hysteresis and mullins effect of tough double-network hydrogels,” *Macromolecules*, vol. 40, no. 8, pp. 2919–2927, 2007.
- [132] J. A. C. Harwood and A. R. Payne, “Stress softening in natural rubber vulcanizates. Part III. Carbon black-filled vulcanizates,” *J. Appl. Polym. Sci.*, vol. 10, no. 2, pp. 315–324, 1966.
- [133] J. A. C. Harwood, L. Mullins, and A. R. Payne, “Stress softening in natural rubber vulcanizates. Part II. Stress softening effects in pure gum and filler loaded rubbers,” *J. Appl. Polym. Sci.*, vol. 9, no. 9, pp. 3011–3021, 1965.
- [134] D. E. Hanson *et al.*, “Stress softening experiments in silica-filled polydimethylsiloxane provide insight into a mechanism for the Mullins effect,” *Polymer (Guildf)*, vol. 46, no. 24, pp. 10989–10995, 2005.

- [135] V. M. Litvinov, R. A. Orza, M. Klüppel, M. Van Duin, and P. Magusin, “Rubber–filler interactions and network structure in relation to stress–strain behavior of vulcanized, carbon black filled EPDM,” *Macromolecules*, vol. 44, no. 12, pp. 4887–4900, 2011.
- [136] H. Luo, M. Klüppel, and H. Schneider, “Study of filled SBR elastomers using NMR and mechanical measurements,” *Macromolecules*, vol. 37, no. 21, pp. 8000–8009, 2004.
- [137] L. Mullins, “Softening of rubber by deformation,” *Rubber Chem. Technol.*, vol. 42, no. 1, pp. 339–362, 1969.
- [138] C. Storm, J. J. Pastore, F. C. MacKintosh, T. C. Lubensky, and P. A. Janmey, “Nonlinear elasticity in biological gels,” *Nature*, vol. 435, no. 7039, pp. 191–194, 2005.
- [139] O. Chaudhuri, S. H. Parekh, and D. A. Fletcher, “Reversible stress softening of actin networks,” *Nature*, vol. 445, no. 7125, pp. 295–298, 2007.
- [140] L. Mullins and N. R. Tobin, “Theoretical model for the elastic behavior of filler-reinforced vulcanized rubbers,” *Rubber Chem. Technol.*, vol. 30, no. 2, pp. 555–571, 1957.
- [141] C. Ma, T. Ji, C. G. Robertson, R. Rajeshbabu, J. Zhu, and Y. Dong, “Molecular insight into the Mullins effect: irreversible disentanglement of polymer chains revealed by molecular dynamics simulations,” *Phys. Chem. Chem. Phys.*, vol. 19, no. 29, pp. 19468–19477, 2017.
- [142] R. Diaz, J. Diani, and P. Gilormini, “Physical interpretation of the Mullins softening in a carbon-black filled SBR,” *Polymer (Guildf.)*, vol. 55, no. 19, pp. 4942–4947, 2014.
- [143] N. Lubbers, J. S. Smith, and K. Barros, “Hierarchical modeling of molecular energies using a deep neural network,” *J. Chem. Phys.*, vol. 148, no. 24, p. 241715, 2018.
- [144] E. M. Dannenberg and J. J. Brennan, “Strain energy as a criterion for stress softening in carbon-black-filled vulcanizates,” *Rubber Chem. Technol.*, vol. 39, no. 3, pp. 597–608, 1966.

- [145] T. S. Gaaz, A. B. Sulong, M. N. M. Ansari, A. A. H. Kadhum, A. A. Al-Amiery, and M. S. H. Al-Furjan, “Effect of halloysite nanotubes loading on thermo-mechanical and morphological properties of polyurethane nanocomposites,” *Mater. Technol.*, vol. 32, no. 7, pp. 430–442, 2017.
- [146] M. Meunier, “Introduction to materials studio,” in *EPJ Web of Conferences*, 2012, vol. 30, p. 4001.
- [147] M. A. N. Dewapriya and R. E. Miller, “Superior Dynamic Penetration Resistance of Nanoscale Multilayer Polymer/Metal Films,” *J. Appl. Mech.*, vol. 87, no. 12, 2020.
- [148] J. Diani, B. Fayolle, and P. Gilormini, “A review on the Mullins effect,” *Eur. Polym. J.*, vol. 45, no. 3, pp. 601–612, 2009.
- [149] V. Bourg, P. Ienny, A. S. Caro-Bretelle, N. Le Moigne, V. Guillard, and A. Bergeret, “Modeling of internal residual stress in linear and branched polyethylene films during cast film extrusion: Towards a prediction of heat-shrinkability,” *J. Mater. Process. Technol.*, vol. 271, pp. 599–608, 2019.
- [150] Z. Rigbi, “Reinforcement of rubber by carbon black,” *Prop. Polym.*, pp. 21–68, 1980.
- [151] D. Hossain, M. A. Tschopp, D. K. Ward, J.-L. Bouvard, P. Wang, and M. F. Horstemeyer, “Molecular dynamics simulations of deformation mechanisms of amorphous polyethylene,” *Polymer (Guildf)*, vol. 51, no. 25, pp. 6071–6083, 2010.
- [152] R. W. Ogden and D. G. Roxburgh, “A pseudo-elastic model for the Mullins effect in filled rubber,” *Proc. R. Soc. London. Ser. A Math. Phys. Eng. Sci.*, vol. 455, no. 1988, pp. 2861–2877, 1999.
- [153] R. W. Ogden, “Elastic deformations of rubberlike solids,” in *Mechanics of solids*, Elsevier, 1982, pp. 499–537.
- [154] R. W. Ogden, “Stress softening and residual strain in the azimuthal shear of a pseudo-elastic

- circular cylindrical tube,” *Int. J. Non. Linear. Mech.*, vol. 36, no. 3, pp. 477–487, 2001.
- [155] E. Peña, J. A. Peña, and M. Doblaré, “On the Mullins effect and hysteresis of fibered biological materials: A comparison between continuous and discontinuous damage models,” *Int. J. Solids Struct.*, vol. 46, no. 7–8, pp. 1727–1735, 2009.
- [156] R. W. Ogden, “Large deformation isotropic elasticity—on the correlation of theory and experiment for incompressible rubberlike solids,” *Proc. R. Soc. London. A. Math. Phys. Sci.*, vol. 326, no. 1567, pp. 565–584, 1972.
- [157] L. Huang, X. Yang, and J. Gao, “Pseudo-elastic analysis with permanent set in carbon-filled rubber,” *Adv. Polym. Technol.*, vol. 2019, 2019.
- [158] C. Schran, F. Uhl, J. Behler, and D. Marx, “High-dimensional neural network potentials for solvation: The case of protonated water clusters in helium,” *J. Chem. Phys.*, vol. 148, no. 10, p. 102310, 2018.